

Review on pore-network modeling studies of gas-condensate flow: Pore structure, mechanisms, and implementations

Ahmad Hosseinzadegan^a, Amir Raouf^{b,*}, Hojjat Mahdiyar^a, Ehsan Nikooee^c, Mojtaba Ghaedi^a, Jafar Qajar^a

^a Department of Petroleum Engineering, School of Chemical and Petroleum Engineering, Shiraz University, Shiraz, Iran

^b Department of Earth Sciences, Utrecht University, Utrecht, Netherlands

^c Department of Civil and Environmental Engineering, Shiraz University, Shiraz, Iran

ARTICLE INFO

Keywords:

Condensation
Snap-off
Pore-network modeling
Gas-condensate flow
Compositional pore-network modeling

ABSTRACT

Gas-condensate flow is a critical process in the near-well region where the well production efficiency is strongly affected by the production of condensate dropout. Pore-scale simulations have provided an understanding of the underlying processes such as snap-off and the effect of the interplay between viscous and capillary forces on gas-condensate flow and its induced blockage within the pore spaces. Among various modeling approaches used to explore these phenomena, pore-network modeling, due to its computational efficiency and the ability to simulate relatively large sample sizes, has appealed to researchers. This article presents a review of the development of pore-network models to simulate gas-condensate flow, particularly in the near wellbore regions. This contribution reviews pore-scale mechanisms that should be included in simulating the gas-condensate flow, together with the involved processes and the peculiarities pertinent to such modeling efforts.

After a brief review of different pore scale studies and their differences, advantages, and disadvantages, the review focuses on pore-network modeling, and the application of pore-network modeling in gas-condensate flow in the recent studies. The employed methodologies, highlights, and limitations of each pore network study are examined and critically discussed. The review addresses pore-space evolution, flow mechanisms, and the involved flow and transport parameters. The formulations of capillary entry pressure in different pore geometries, the corresponding conductance terms, snap-off criteria, and conditions for the creation of condensate bridging in different pore structures are presented. Additionally, three major approaches used in pore-network modeling of gas condensation, namely quasi-static, dynamic methods and dynamic compositional pore-network modeling, are presented and their main governing equations are provided using various tables. Finally, the significance of gas-condensate flow modeling including its modeling challenges together with the main similarities and differences among pore-network studies are provided.

1. Introduction

Retrograde behavior is the characteristic of gas-condensate reservoirs when the reservoir pressure falls below the line of dew point and liquid droplets form in the porous media. This results in condensate formation in the gas-condensate reservoir, which hinders the gas flow and drastically influences well deliverability and production. Furthermore, the liquid dropout and deposition of condensate, rich in heavier components, adversely affects the composition of produced gas. Therefore, measures should be taken to prevent condensate formation in the reservoir. The near-wellbore zone is of major concern where the creation

of large quantities of liquid dropouts and buildup of condensates occur in the presence of capillary forces, which significantly impairs well production. Other accompanying factors, including low gas-liquid interfacial tension (IFT), very high gas velocity in the vicinity of the wellbore, and the impact of inertial effects, have a considerable influence on the gas relative permeability and well production. Previous studies (mostly core-flood experiments) showed that relative permeability in gas-condensate reservoirs increases with velocity in this low-IFT two-phase flow process, which is known as “positive coupling” (Danesh et al., 1994; Henderson et al., 1995, 1997, 2000; Mott et al., 2000; Jamiolahmady et al., 2009; Gholampour and Mahdiyar, 2019).

* Corresponding author.

E-mail address: a.raouf@uu.nl (A. Raouf).

<https://doi.org/10.1016/j.geoen.2023.211693>

Received 8 August 2022; Received in revised form 17 January 2023; Accepted 15 March 2023

Available online 30 March 2023

2949-8910/© 2023 The Authors. Published by Elsevier B.V. This is an open access article under the CC BY license (<http://creativecommons.org/licenses/by/4.0/>).

While the inertial force decreases the effective gas permeability, the positive coupling effect (i.e., the velocity dependency of the relative permeability) leads to an increase of the effective gas-condensate relative permeability. It may be speculated that higher gas velocity facilitates the movements of condensate bridges and opens pathways for gas flow. Based on gas-condensate flow experiments performed by Mott et al. (2000), the high capillary number regime (i.e., with the high ratio of viscous forces to capillary forces, $N_c = V_g \mu_g / \sigma$ where V_g is gas velocity, μ_g denotes gas viscosity, and σ stands for interfacial tension (IFT)) has a positive effect on well productivity, while inertial flow (i.e., the non-Darcy effect) reduces the effective gas permeability. This coupling effect was well reported and documented by Jamiolahmady et al. (2000, 2003) for gas-condensate flow under low IFT conditions.

Various researchers have studied the competition between viscous and capillary forces as the primary operating forces at the micro-scale and even nano-scale affecting the flow of gas-condensate. The gas-condensate flow is controlled by the formation of condensate bridges and their subsequent mobilization, which are governed by pore-scale characteristics and physics such as pore morphology, connectivity, as well as wettability. As such, macroscopic formulations of gas-condensate flow and system permeability are not possible without an in-depth knowledge and understanding of several pore-scale mechanisms, such as droplet formation, corner/film flow, and snap-off, and their influence on the gas condensate flow, which necessitates pore-scale models. Pore-scale models can be divided into two main groups of methods, those which consider an idealization of the pore space, conceptualized as a set of different interacting or noninteracting geometrical elements (e.g., pore-network models, a bundle of capillary tubes, interacting capillary bundle, an extended bundle of capillary tubes, pore morphology technique, and pore unit assembly (Sweijen et al., 2016, 2017; Raouf and Hassanizadeh, 2010; Cai et al., 2022) and direct numerical simulations (DNS), which involve detailed flow simulations directly performed on a full portrait of pore space (Golparvar et al., 2018; Fathi et al., 2017; Zhao et al., 2019; Raeini et al., 2015; Mehmani et al., 2020; Cai et al., 2022) (see also Table 1).

Provided that there is sufficient computational capacity and spatial resolution of the pore structure, DNS can simulate fluid flow directly on any arbitrary pore space geometries. DNS, which employ well-established numerical methods and computational fluid dynamics (CFD) techniques, suffer from their high computational demand. Application of DNS on a highly resolved computational domain results in a drastic increase in simulation time (Cai et al., 2022), and therefore, this category of pore scale techniques is often considered inefficient for a computational domain with dimensions near enough to a three-dimensional representative elementary volume (REV). There have, however, been efforts to introduce multiscale formulation to alleviate this problem (Guo et al., 2019; Mehmani and Tchelepi, 2018, 2019). Furthermore, efforts have been made to accelerate DNS by CPU (Pan et al., 2004) or GPU parallelization (An et al., 2017), and suggestions have been made to use quantum computing (Sahimi and Tahmassebi, 2022). The use of artificial intelligence in porous media characterization and modeling for diverse applications spanning from the prediction of petrophysical characteristics, and constitutive parameters (Ahmadi and Chen, 2019; Sakhaei et al., 2020; Tembely et al., 2020), to pore scale imaging (Wang et al., 2021; Tang et al., 2022) has offered new opportunities to employ DNS-informed intelligent techniques on reasonably large domains (Da Wang et al., 2020; Santos et al., 2020; Zhou et al., 2022). Besides, DNS can experience irreducible numerical errors for capillary-dominated (i.e., low capillary number, N_c) flow (Scardovelli and Zaleski, 1999; Chen et al., 2020).

Pore-network modeling (PNM), however, is based on a much-idealized description of the porous media and utilizes much faster multiphase formulations, making it capable of modeling much larger domains and a natural option for investigating the copious number of scenarios required for stochastic modeling as well as parametric studies.

For example, Mahmoodlu et al. (2020) have used PNM to simulate flow and chemical transport in a large (36-cm long) sand column to compare the 3D pore-scale results of flow and solute transport against the continuum-scale model. Furthermore, several pore-scale physical phenomena can be directly introduced at the pore scale making PNM ideal for coupled processes and phenomenological multiphase flow and multi-component reactive transport modeling (Raouf et al., 2013). Detailed classification and discussion of the advantages and disadvantages of different pore scale models have been presented in Table 1.

The motive to use pore scale approaches such as pore-network models for gas-condensate modeling lies in the physics and processes at the pore scale, which are difficult to be captured otherwise and accounted for in the larger macro-scale models. Pore-network models can help us to get parameter values that can quantify the effect of condensate formation on the macro-scale constitutive relations, such as gas-condensate relative permeability curves. Hereafter, the review is focused on the pore-network modeling. For other methods of modeling gas-condensate flow, the gas-condensate thermodynamic fluid behavior analysis, and flow/production prediction models, the reader can refer to a review study presented by Panja et al. (2020).

The early experimental studies of the pore-scale mechanisms involved in the gas-condensate flow (i.e., micromodel studies) were somewhat limited to qualitative investigation of the phenomena and were challenging to be performed due to the required high-pressure level. Detailed analysis and quantification of pore-scale phenomena have, however, been performed by the development of pore-network models, described in detail in the next sections. The PNM approach has been further used to obtain macro-scale properties of porous media, such as capillary pressure (P_c), relative permeability (K_r), and residual oil saturation (S_{or}), by adding fluid flow physics to the pore-scale (e.g., viscous forces, capillary forces, inertial effects, and flow regimes) as well as pore space morphology and fluid characteristics (e.g., pore geometries, wettability, and IFT) (Blunt and King, 1991; Hui and Blunt, 2000; Blunt et al., 2002; Al-Gharbi and Blunt, 2005; Piri and Blunt, 2005; Chalbaud et al., 2007; Sorbie and Skauge, 2012). Pore-scale models including pore-network models can be used in Enhanced Oil Recovery (EOR) to explore the effect of porous rock structure, wettability alteration (e.g., gas wetting projects, surfactant flooding, and smart water injection), viscosity ratios, and IFT change (e.g., use of nanofluids, gas-condensate flow, and steam flooding) on the recovery. The computation speed of PNM is often much higher compared to the direct numerical simulations like the Lattice Boltzmann Method (LBM), which brings the possibility of simulating larger porous media samples (Mahmoodlu et al., 2020). On the other hand, pore-network models require knowledge of the internal porous structure, including pore and throat statistical distribution properties as well as cross-sectional shapes of pores and throats. Such knowledge could be acquired through advanced image analysis techniques.

In the PNM approach, the void space of a porous medium is characterized as a two or three-dimensional lattice of pore bodies linked by pore channels (i.e., throats) as a representative model of porous rock to study the pore-scale physics such as solute mass transport, wettability alteration (Ganiae et al., 2019), and multiphase flow (Raouf et al., 2013). Such processes and physics are critical in petroleum applications and enhanced oil recovery (EOR). For constructing a representative pore-network model, the following information should be specified: pore body and throat size distribution, the distribution of pore coordination number (the number of pore throats neighboring a specific pore), pore cross-sectional shape and geometry, as well as pore-network wettability represented by contact angle (Raouf et al., 2013; Khaksar et al., 2013; Nikoee et al., 2014; Rostami et al., 2015; Daneshian et al., 2021).

Pore-network geometry and topology can be obtained through computer-generated media or by imaging (Raouf and Hassanizadeh, 2010). Raouf and Hassanizadeh (2010) developed algorithms to create a pore-network model which can generate networks with the desired

Table 1
Different pore-scale modeling categories highlighting their capabilities, as well as drawbacks or challenges.

Main category	Sub-category	Approach	Advantages	Disadvantages/challenges	References
Direct numerical simulations (DNS)	Particle based	Lattice-Boltzmann Method (LBM)	<ul style="list-style-type: none"> + A straightforward algorithm based on a statistical equation describing the streaming and collision of fluid molecules in space + It does not need any discretization technique and thus is free of truncation errors + Accurate in delineating the detailed pore structures and accurate account of complex topologies + Highly suitable for parallel computation (Liu et al., 2012) + Ease of implementation for complex solid boundaries (Zhao et al., 2020) 	<ul style="list-style-type: none"> - Computationally demanding - LBM is strongly dependent on fluid viscosity which can lead to unphysical behaviours, if not carefully dealt with; multi-relaxation-time (MRT) LBM can significantly help to alleviate this issue 	<p>Golparvar et al. (2018) Nekoeian et al. (2018) Zhao et al. (2020) Vogel et al. (2005)</p>
Direct numerical simulations (DNS)	Particle based	Smoothed Particle Hydrodynamics (SPH)	<ul style="list-style-type: none"> + Accurate in delineating the pore structures + No need to nodal integration points (particles) to be distributed on grids or meshes resulting in less computationally expensive spatial discretization of complex pore spaces + Making use of an updated Lagrangian approach and suitable to deal with nonlinear convection terms, tracking of interfaces and their coalescence + Explicit SPH approaches allow for massive parallel High Performance Computations (HPC) (Osorno et al., 2021) 	<ul style="list-style-type: none"> - High computational costs associated with repetitive use of neighbor searching algorithms - Time stepping stability criteria such as the Courant–Friedrichs–Lewy (CFL)-condition are restrictive when used in explicit time integration schemes for implementation of SPH - Difficulty in accurate imposition of boundary conditions such as prescribed flux and/or prescribed pressure boundary condition - Further stability criteria have to be fulfilled, e.g., Fourier criteria for diffusion-type problems 	<p>Golparvar et al. (2018) Tartakovsky and Meakin (2006) Kunz et al. (2016) Sivanapillai and Steeb (2018) Osorno et al. (2021) Tartakovsky et al. (2007)</p>
Direct numerical simulations	Particle based	Dissipative Particle Dynamics (DPD)	<ul style="list-style-type: none"> + Modeling a small cluster of atoms or molecules as particles, and being a mesoscale method (between micro- and pore-scale) offers an important tool in multiscale studies + Suitable for modeling complex fluid flow in porous media such as polymer suspensions, liquids with interfaces, colloids and gels and to simulate discrete nature of flow in nanometer size pores in media such as shales (containing nano-scale along with much larger size pores) + Suitable for parallelization + Rigorously conserves mass and momentum 	<ul style="list-style-type: none"> - DPD is not efficient as other methods of the same category such as LBM and is computationally demanding 	<p>Liu et al. (2015) Liu et al. (2007)</p>
Direct numerical simulations	Grid based	Volume of Fluid (VOF)	<ul style="list-style-type: none"> + Accurate in delineating the pore structures + No known issue of mass conservation, accordingly superior in that respect to methods such as level set 	<ul style="list-style-type: none"> - Computationally demanding - Calculation of interfacial properties like normal vectors and curvatures involves approximations 	<p>Golparvar et al. (2018) Jettestuen et al. (2021)</p>
Direct numerical simulations	Grid based	Level-set	<ul style="list-style-type: none"> + Accurate in delineating the pore structures + Calculation of interfacial properties like normal vectors and curvatures is easier to achieve as compared to VOF (Jettestuen et al., 2021) + Capable of handling interface redistribution and its topological changes induced by capillary instabilities (Singh et al., 2022) 	<ul style="list-style-type: none"> - Computationally demanding - It suffers from mass conservation issues 	<p>Sethian (1999) Meakin and Tartakovsky (2009) Golparvar et al. (2018) Jettestuen et al. (2021) Singh et al. (2022)</p>
Direct numerical simulations	Mesh and mesh-free	Phase-field	<ul style="list-style-type: none"> + Straightforward modeling of multiple phases + The evolution of phase field helps to track the interface and there is no need for explicit interface tracking techniques + Robust derivation based on energy concepts + Simple implementation + Accurate mass conservation + A multipurpose and robust method by use of diffuse interfaces 	<ul style="list-style-type: none"> - Computationally demanding - Numerical instability and stiffness of governing equations - Requires fine mesh in the interface region - The physical meaning of characteristic length is ambiguous - Difficult imposition of internal constraints - Highly nonlinear, numerical instabilities and convergence issues. 	<p>Nguyen et al. (2019) Frank et al. (2018) Zhu et al. (2019) Alpak et al. (2018)</p>
Pore space geometrical idealization	Pore-network modeling (PNM)		<ul style="list-style-type: none"> + A fast and cost-effective tool suitable to study the variables that are difficult to determine from the experiments 	<ul style="list-style-type: none"> - The identification of features/phenomena relevant to the modeled processes and neglecting the rest to reduce the computational load 	<p>Xiong et al. (2016) Cai et al. (2022) Ovaysi and Piri (2010)</p>

(continued on next page)

Table 1 (continued)

Main category	Sub-category	Approach	Advantages	Disadvantages/challenges	References
			+The main advantage is the simplicity of the multiphase algorithms (making use of a simplified form of mass and momentum equations) as compared with direct numerical simulations (DNS) solving the full Navier-Stokes equations + PNM is very efficient computationally speaking and suitable for much larger domains as those easily modeled in DNS + Capable of describing/incorporating all relevant multiphase flow processes + Increasing the accuracy of pore network-modeling for two-phase flow by introducing extra computational nodes in pore bodies and pore throats + Enabling calculation of fluxes around the non-wetting phase in each pore body and pore throat of the pore network + Adaptive node refinement based on drainage state of pores to enhance computational efficiency	- The more precise the knowledge of the morphology of pore geometry and the physical processes at the pore-scale, the more accurate the results that are obtained. - It is challenging to be applied in the unconventional reservoirs where fracture networks coexist with micropores. - Loss of geometrical and topological information resulted from geometrical simplifications involved in pore network extraction can bring about inaccuracies. - Complex modeling required to simulate two-phase flow - The number of unknowns is increased in pore bodies from one unknown per pore to 8 unknowns per pore	Zhao et al. (2020) Tranter et al. (2020) Thompson (2002)
Pore space geometrical idealization	Further extension of Pore-network modeling (PNM): Refining pore bodies and pore throats		+ Enabling multi-physics modeling inducing single/multiphase flow, adsorptive transport, multi-component reactive transport + Representing diverse porous media using computer generated pore networks having pore connections (coordination number) between 0 and 26	- Computer generated pore networks have a lattice based (i.e., regular) pore locations	Raouf and Hassanizadeh (2012)
Pore space geometrical idealization	Further extension of Pore-network modeling (PNM): Multi-directional pore-network modeling		+ In PUA, a pore network is extracted from a grain packing, the coupling of the PNM with discrete element techniques provides an opportunity to model two-phase flow in deformable porous media	- As throats in this approach are commonly idealized as a 2-d entity between two adjacent pore units, the length of throat is not obtained directly and a proper choice for throat radius for different granular media is also not yet well explored (Daneshian et al., 2021)	Raouf and Hassanizadeh (2010) Raouf et al. (2013)
Pore space geometrical idealization	Pore unit assembly (PUA)		+ Easy to use for derivation of closed form formula	- Oversimplification of the porous media and casting it into only one element, namely, capillary tube and assigning both functions of pores (storage) and throats (accessibility and conduction) results in discrepancies in its simulation results. - Furthermore, ordinary BCT is unable to model corner flow, lacks connection and interaction between different elements.	Mason and Mellor (1995) Sweijen et al. (2016, 2017) Nikooee et al. (2016, 2017) Hosseinkhani et al., 2023 van Genuchten (1980) Hunt et al. (2013) Daneshian et al. (2021)
Pore space geometrical idealization	Bundle of capillary tube model (BCT)		+ The same merits as BCT, further to that the positions of nonwetting-wetting menisci in the capillaries of the interacting tube bundle model are dependent of each other because of pressure equilibration	- The model suffers from joint function of pore and throats expected from single capillary tube element, all capillary tubes of the same size have access to the front and there is no restrictive element or path limiting their access to invading fluid, contrary to pore network or pore unit assembly approaches	Dong et al. (2005)
Pore space geometrical idealization	Interacting bundle of capillary tube model (IBCT)		The same merits as BCT, further to that, its capillary tube elements include corners and shapes closer to natural granular media, offering opportunities to account for residual saturation residing on pore corners, thin films adsorbed to grain surfaces and liquid bridges + The model simulations seem reliable for sphere packings, and unconsolidated porous media, and enjoy lower computational demand	- Loss of connection between capillary tubes, the same demerits as BCT	Likos and Jaafar (2013)
Pore space geometrical idealization	Extended bundle of capillary tubes		- The original algorithm is restricted to quasi-static drainage simulation - It does not account for corners and films flow - The accuracy of the results can be dependent on the grain size distribution of the medium.		Hilpert and Miller (2001) Sweijen et al. (2017)
Pore space geometrical idealization	Pore morphology technique (PMT)				

distribution of pore coordination numbers where the maximum coordination number could be as large as 26 which is sufficient for most porous materials. Pore networks can also be extracted using different imaging techniques. The algorithm of pore-network extraction consists of morphological image processing techniques such as skeletonizing, and distance transform, where the centerline of throats is obtained and used to identify pores and throats (Dong and Blunt, 2009; Rabbani et al., 2014; Xiong et al., 2016; Yi et al., 2017; Gostick, 2017).

Two PNM approaches are widely applied for modeling two-phase flow, namely, quasi-static and dynamic. In quasi-static pore-network modeling, capillary pressure in each step is assumed to be equilibrated through the porous medium, and the Young-Laplace equation is used to simulate fluid displacement (Fatt, 1956a, 1956b, 1956c; Øren et al., 1998; Blunt et al., 2002; Raouf and Hassanizadeh, 2012; Joekar-Niasar et al., 2010b). In dynamic pore-network models, a set of linear algebraic equations is formed and solved to find the distribution of pressure and

saturation of phases across the pore-network length (Koplik and Lasseter 1985; King, 1987; Blunt and King, 1991; Aker et al., 1998; Mogensen and Stenby, 1998; Thompson, 2002; Singh and Mohanty, 2003; Al-Gharbi and Blunt (2005); Joekar-Niasar et al., 2010a; Raouf et al., 2013, Yin et al., 2018). The approximation of quasi-static displacement is not valid in the presence of rate-dependent effects in displacements which may occur under low IFTs. This effect substantially reduces capillary forces, which is evident in gas-condensate reservoirs and near wellbore flow where the formation and flow of the wetting layers/films are significant, and both capillary and viscous forces contribute to the fluid redistributions at the pore scale (Blunt et al., 2002). Joekar-Niasar and Hassanizadeh (2012) presented a comprehensive literature review on analyzing two-phase flow fundamentals at the pore scale using PNM. They reviewed dynamic pore-network models, their topological and geometrical structures, computational algorithms, as well as their applications. For computational algorithms, two main approaches were introduced. The single-pressure method in which pressure calculation was performed for a single equivalent phase, and the two-pressure algorithm in which the pressure is determined for each phase. Then, the numerical challenges like geometry definition and conductivity calculations and local rules implementations were discussed. As PNM challenges, they considered the quantification of network geometry and topology, computational costs, the need for sophisticated imaging techniques for verification of assumed porous structure and local rules, and complex implementation of physical processes in a dynamic fluid flow system. Xiong et al. (2016) reviewed the pore-network construction by statistical reconstruction, grain-based model, and direct mapping techniques. They indicated that the application of PNM is computationally feasible and faster than direct methods. However, the predictions may be limited due to possible inaccuracies in simplifications of the geometry of constructed network and the lack of experimental resolution in pore space characterization. Thus, advancements in pore space reconstruction can potentially increase the accuracy of predictions. Golparvar et al. (2018), in a comprehensive review paper, described different simulation methodologies such as Bundle of Capillary Tube Modeling (BCTM), Direct Pore Scale Modeling (DPSM), and PNM to study the pore-scale mechanisms in porous media. They discussed two main fluid flow modeling approaches, quasi-static and dynamic. They noted that dynamic network models are more appropriate for simulating flow regimes where viscous and gravity effects are important and cannot be neglected. In another review paper, Wopara and Iyuke (2018) described wettability variations and oil recovery mechanisms in the implementation of the PNM method for water-flooding of different sandstone and carbonate rocks. They stated that capturing the multi-scale nature of shale gas-oil systems is essential and requires further studies to characterize better pore space and wettability, which, in turn, improves the analysis of hydrocarbon recovery by water flooding through pore-network models.

The flow of the gas-condensate in a porous medium near-wellbore region is influenced by pore-scale processes that are difficult to account for in the continuum scale modeling. For this reason, PNM has been used in recent decades to study the effect of statistical and structural pore space properties as well as two-phase flow parameters on the gas-condensate flow and thereby on the gas-condensate relative permeability. The gas-condensate flow is strongly influenced by the formation of condensates in the pore corners (affected by phase behaviors, fluid composition, reservoir pressure, and temperature), their possible swelling and coalescence, thereby, condensate bridge formation, and finally, the condensate bridge movement together with thin film flow, all of which highly dependent on the interplay between viscous and capillary forces as well as rock wettability and pore morphology. Such complex interactions make numerical simulation and experimental study of gas-condensate systems unique, challenging, and different from the conventional two-phase flow systems.

On the one hand, pore-network models of gas-condensate flow require insights into pore-scale filling and flow phenomena which can be

obtained from experimental observations such as microfluidics. On the other hand, experimental pore scale studies of aforementioned pore-scale interactions and mechanisms not only require to be done at high pressure and temperature but also are generally limited due to the difficulty to achieve the same fluid compositions and properties as those under reservoir conditions. Besides, the macroscopic theoretical and numerical studies on flow patterns of gas-condensate reservoirs necessitate knowledge of the gas-condensate relative permeability dependence on phase change and pore-scale processes. Challenges remain regarding how to infer and inspect such knowledge from experiments. For instance, in the shale matrix, advanced and reliable techniques should be developed to measure and study the effect of nano-scale properties on the phase behavior of the gas-condensate fluid. Alternatively, pore-network modeling can be used to investigate multiple physical phenomena to improve our understanding of involved pore-scale processes and thereby develop physically-plausible and more accurate macroscopic formulations for two-phase flow in gas-condensate reservoirs.

As will be discussed in this review, a more comprehensive formulation of pore-scale displacement mechanisms, a detailed depiction of porous media, as well as more computationally efficient and physically reliable algorithms for phase change and condensate formation are required to be incorporated in future PNM studies to improve simulations. Such developments should go hand-in-hand with the developments of high-pressure high-temperature microfluidics and imaging techniques required for capturing pore-scale mechanisms. To explore the application of pore-network models to study the gas-condensate flow, first, the applicability of the pore-network modeling approach is discussed, an overview of different studies on the subject is presented, and the results are critically analyzed and reported. Then, the utilized pore-network geometries and pore structure characterization methods are reviewed in detail, followed by an introduction to the applied physical processes used to describe phase change, condensation, and two-phase flow. As will be demonstrated in this analysis, not all reviewed PNM studies have comprehensively addressed all involved physical processes. Next, the main governing equations are provided, and, finally, the significance of the PNM approach, challenges, and main concluding remarks are provided.

2. Pore-network modeling to explore the gas-condensate flow

2.1. Overview of the PNM applications in gas-condensate flow

The first pore-network model studies on gas-condensate flow have mostly aimed at the investigation of the effect of pore-scale geometrical and physical parameters on critical condensate saturation (i.e., the specific saturation at which the condensate begins to flow) as well as the determination of the gas and condensate distribution in the pore network under gravity, capillary, and viscous forces using phenomenological models. In these studies, the gas-condensate flow was simulated via quasi-static pore-network modeling based on percolation theory and local capillary equilibrium under low capillary numbers. The pore-scale mechanisms implemented in the multiphase flow through early pore-network models mainly consist of drainage and imbibition processes. In the drainage process, flow primarily happens in the form of piston-like displacement (Blunt and King, 1991; Blunt, 1997; Hui and Blunt, 2000; Al-Gharbi and Blunt, 2005). The imbibition process is, however, more complex and may include displacements governed by only the main terminal meniscus the so-called piston-like displacement, but also the movement of corner menisci towards the center line of a pore known as snap-off, and displacement of wetting phase from the connecting throats into a pore, commonly referred to as the pore-body filling displacement (Aker et al., 1998; Mogensen and Stenby, 1996, 1997, 1998; Hughes and Blunt, 2000; Singh and Mohanty, 2003; Nguyen et al., 2006; Idowu, 2009; McDougallLi and Sorbie, 2017). In the gas-condensate flow in the porous media, the main displacement

processes, which are commonly studied through pore-network models are considered to be film/corner flow depending on the pore geometry, snap-off, and the displacement of condensate bridges induced by the gas pressure increase.

Table 2 presents main PNM approaches used for modeling gas-condensate flow including percolation theory, quasi-static modeling, two-phase dynamic modeling, and compositional pore-network modeling. The major physical parameters (and phenomena) addressed in each study are also referred to in this table.

In what follows, the results of the PNM studies mentioned in Table 2 with their modeling objectives and studied physical parameters are described in detail.

The first pore network construction to study the micro-scale aspects of gas-condensate flow dates back to Mohammadi et al. (1990). They have simulated the phenomenon of retrograde behavior and vaporization induced by a pressure change in the porous media. The main aim was to develop a mathematical model for the process of retrograde condensation by pressure reduction in porous media. They calculated the gas and condensate relative permeabilities considering the irreducible water saturation in the system and neglected the influence of gravity. The results were compared with the conventional strongly water-wet two-phase relative permeability. Their study revealed that the reduction in the relative permeability of gas is highly pronounced due to the formation of condensate and concluded that the relative permeability of condensate at the maximum condensate dropout is comparable to that of the conventional wetting phase relative permeability. The increase in relative permeability of condensate was attributed to the larger-size pores which get filled with condensate and contribute considerably to the overall conductivity. They found a significant effect of the conductance of the throats and its formulation and pore coordination number on the calculated condensate relative permeabilities. Moreover, the choice of geometry of the pores could highly influence phase relative permeability and phase entrapments. Among selected geometries, tetrahedral geometry led to the largest phase trapping. Moreover, no significant hysteresis in gas and condensate relative permeability during the condensation-vaporization process was observed. They stated that the assumption of capillary occupancy is not appropriate in near-critical points and under gravity drainage film flow when condensate is dripping out, as fluid films, over the grain surfaces and the IFT effect is also negligible. Percolation theory applied in the Bethe lattice network (i.e., a regular tree structure with a connected cycle-free graph) showed to be insufficient in near-critical point conditions to describe film flow in the presence of the gravitational effects.

In 1999, Wang and Mohanty developed a mechanistic pore-network model using percolation theory to study the effect of phase entrapment and connectivity at pore corners on the critical condensate saturation, S_{cc} . In their model, the pore body radius showed a considerable impact on the reduction of S_{cc} . They stated that the higher the pore size becomes, the higher the volume of condensate required for making the spanning cluster would be, as the connectivity and coalescence of condensate in throats and pores would be more difficult to achieve. However, as the total pore volume also increases, a decrease in S_{cc} is eventually observed. Characterization of the pore network was done using connectivity, pore shape, and pore radius distributions. In the cubic network model, the presence of the wetting phase (water) had a significant impact on S_{cc} and S_{cc} was predicted to be as low as 4% in the presence of water (~16%) and as high as 45% in the absence of the water phase. They considered a sphere-pack model with modification (Fig. 1a), where S_{cc} decreased as a result of any of the following conditions: a) as mean connectivity increased, b) as throat radius decreased, c) as pore radius increased, and d) as the pore-throat radii were correlated. The resulting critical liquid saturation was underestimated due to overrating pore corner connectivity. In their cubic model (Fig. 1b), by increasing the connectivity, throat radius, pore radius, length, and throat shape factor, X (i.e., defined between 0 (straight throat) and one (converging-diverging shape) to represent the throat size at the

connection to a pore body), S_{cc} decreased. Furthermore, an uncorrelated relation between throat-pore radii also led to a decrease in S_{cc} . The positive and negative correlations are summarized in Table 3. Furthermore, with increasing connate water saturation and decreasing gas-condensate IFT (an increase of the Bond number), S_{cc} decreased in their cubic model.

Based on the quasi-static approach (i.e., supposing that the equilibrium states of two-phase flow are governed by only local capillary pressures), Fang et al. (1996), Bustos and Toledo (2003a,b) developed pore-network models to study different aspects of gas and condensate flow while neglecting the viscous effects. The quasi-static approach in PNM of gas-condensate flow will be further discussed in this review study (in section 2.3: processes and condensation implementation). To calculate critical condensate saturation, Fang et al. (1996), used a small two-dimensional square network of tubular pore segments in which the gravity effects were accounted for. They found that the critical condensate saturation can be considered mainly a function of IFT, the pore size, and contact angle hysteresis. They showed that pore geometries with curved triangular shapes could retain larger liquid volumes as compared to pores with circular or triangular cross-sections. Bustos and Toledo (2003b) proposed a mathematical model for the formation of the condensate phase and its flow in the lattice of capillaries to investigate the effect of statistical properties of the lattice on gas-condensate relative permeability curves by two and three-dimensional cubic models. They applied the model of Fang et al. (1996), and the condensation process was simulated by the Monte Carlo method without condensate re-vaporization. The pore level mechanisms observed in glass micro-models and reported in the literature were considered in their model. Moreover, the gravity effects were also included. Menisci movement was considered a quasi-static and capillary-controlled process. They concluded that the relative permeability is related to the pore geometrical characteristics, particularly for the gas phase. The gas relative permeability showed two trends of decline, first one was attributed to an initial flow regime for gas flow when condensate wedges were forming and occupying the corners of the throats, and the second flow regime represented an abrupt gas relative permeability decline when condensate bridges were forming in throats by coalescence of those formed in the corners. In another work in 2003, they presented the effect of contact angle hysteresis on gas-condensate relative permeabilities using a 3D pore-network model considering only the contribution of capillary and gravity forces using a truncated lognormal distribution for the inscribed radius of throats. They used three receding contact angles of zero, 10 and 20°, while considering spatially uniform contact angles in each simulation, and assuming an advancing contact angle of 30°. The results were presented at a fixed mean pore size of 50 μm and different standard deviations of pore sizes (i.e., 8, 15, 30, and 50 μm). The same flow patterns stated earlier for the relative permeability of gas were observed, and both the change of wettability towards the intermediate wetting and the reduction of contact angle hysteresis had a positive effect on gas-condensate relative permeabilities only in the second flow regime for higher condensate saturations above 20%. Bustos and Toledo (2004) analyzed the pore shape effect (i.e., angularity) on gas-condensate relative permeabilities for the triangle, square, and octahedron cross sections and showed that the higher angularity considering the same inscribed radius leads to higher gas relative permeability at a fixed condensate saturation. Additionally, less angularity in octahedral pore shapes caused the creation of condensate bridges at lower condensate saturations which resulted in an earlier decline in gas relative permeability. The angularity and the skewness of selected pore-size distributions increased condensate relative permeability due to higher connectivity but caused a larger drop in gas relative permeability due to gas path blockage in smaller-size throats.

To include the viscous force effect, dynamic pore-scale models have been implemented by Li and Firoozabadi (2000), Wang and Mohanty (2000), Jamiolahmady et al. (2000, 2003), Momeni et al. (2017), and Labeled et al. (2018) to investigate the interplay between viscous and

Table 2
Summary of gas-condensate PNM: scope of application and objectives.

Approach		Quasi-static: percolation theory			Quasi-static: local capillary equilibrium			
The subject of study		Retrograde condensation and re-vaporization		Critical condensate saturation		Critical condensate saturation		Evaluating the effect of statistical properties of porous skeleton, pore shape and contact angle hysteresis on gas-condensate relative permeability
Author		Mohammadi et al. 1990		Wang and Mohanty 1999		Fang et al. 1996		Bustos and Toledo 2003, 2004
Parameters investigated	Fluid property	Not investigated		Connate water saturation, IFT		Contact angle hysteresis, IFT		Not investigated
	Pore-network structure	Throat conductivity, volume exponents, coordination number, pore size distribution, corner (tetrahedral shape) phase trapping		Connectivity, pore and throat size, pore-throat spatial correlation, throat shape factor, X (representing how the end size of a throat is changing compared to pore body size), throat length		Not studied		Network size, network dimensionality, pore shape and pore size distribution (width, variance and skewness)
Parameters not considered		Thin film flow, angularity, fluid properties effects		Thin film flow, viscous forces, fluid properties effects		Critical condensate saturation		Gas/Condensate relative permeability
Parameters not considered						Thin film flow, angularity, pore-network structure, viscous forces		Thin film flow, fluid properties, viscous forces
Approach		Two-phase dynamic						
The subject of study		Critical condensate saturation and gas-condensate relative permeabilities	The relative permeabilities and non-Darcy coefficients	Flow velocity effect (flow rate effect) on gas-condensate relative permeability	Positive effect of flow velocity on gas-condensate relative permeability	PNM of dynamic displacement of gas and condensate in wellbore region	The impact of condensate saturation on Knudsen flow in shale porous medium	
Author		Li and Firoozabadi 2000	Wang and Mohanty 2000	Jamiolahmady et al. 2000	Jamiolahmady et al. 2003	Momeni et al. 2017	Labed et al. 2018	
Parameters investigated	Fluid property	IFT, gravity, flow rate, pressure gradient, contact angle hysteresis, wettability	IFT, superficial velocity	IFT, flow rate (injection velocity), condensate to gas volume ratio (CGR)	IFT, flow rate (injection velocity), CGR	IFT and velocity	Pressure, condensate saturation	
	Pore-network structure	Not investigated	Pore and throat size, pore-throat spatial correlation, throat shape factor (X), throat length	Not applicable (i.e., single pore unit mechanistic study)	Not investigated	Not investigated	Mean of pore size, standard deviation, coordination number Z	
Parameters not considered		Critical condensate saturation, gas-condensate relative permeability	Pressure gradient, gas-condensate relative permeability	Gas/Condensate relative permeability	Gas/Condensate relative permeability	Gas/Condensate relative permeability	Relative Correction Factor (Darcy flow, Knudsen flow and Knudsen dry gas flow), gas/condensate relative permeability	
Parameters not considered		Thin film flow, pore-network structure, angularity	Thin film flow	Multi-pore interaction, pore-network structure, angularity	Pore-network structure, angularity	Pore-network structure,	Thin film flow, angularity	
Approach		Dynamic compositional						
The subject of study		Compositional pore-scale network model for gas-condensate flow	Phase-change and two-phase flow study in dynamic pore-network modeling	Improvement of gas-condensate flow by wettability change	Evaluation of the impact of IFT and velocity on gas-condensate relative permeability, investigation of the different gas injection strategies to improve gas-condensate flow with condensate vaporization			
Author		Santos and Carvalho 2020	Chen et al. 2020	Reis and Carvalho 2020	Reis and Carvalho 2021, 2022			
Parameters investigated	Fluid property	Differential pressure $P_{inlet} - P_{outlet} = 9.8$ kPa (to study saturation distributions)	Viscosity, composition	Fluid (gas) velocity, IFT, pressure	Fluid (gas) velocity, IFT, fluid composition (to study the gas injection strategy)			
	Contact angles uniformly distributed (degrees)	$\theta = 0$	$\theta = 0$	$\theta = 0, 45, 60, 75, 90, 105, 120$ and 135	$\theta = 0$			
Parameters not considered		Gas-liquid relative permeability	P_c curve, viscosity ratio, phase saturation distributions	Gas-liquid relative permeability, the improvement factor (IF)	Gas-liquid relative permeability, vaporization			
Parameters not considered		Pore-network structure, angularity, capillary, snap-off	Pore-network structure, angularity	Pore-network structure, angularity	Pore-network structure, angularity			

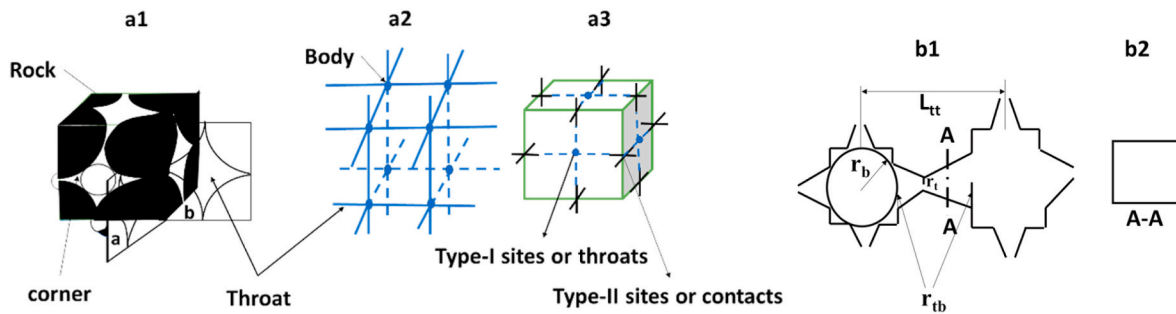


Fig. 1. a) The concept of sphere-pack model: (a1) the sphere pack in the presence of four grains and (a2) the resulting throat–body pore-network. (a3) Connectivity of throat–corner network, b) Cubic model: (b1) Longitudinal section of pore elements; (b2) cross-section of throat.

Table 3

The impact of the involved parameters and their positive/negative correlation (shown by + and - symbols) with the reduction of critical condensate saturation (S_{cc}) (Wang and Mohanty, 1999).

	Connectivity	Throat size	Pore size	Throat-pore body spatial correlation	Connate water saturation (S_{wc})	IFT
Modified sphere pack model	+	-	+	+	Not studied	Not studied
Cubic model	+	+	+	-	+	-

capillary forces on the simultaneous flow of gas and condensate. Li and Firoozabadi (2000) utilized the dynamic pore-network model to analyze critical condensate saturation, and obtain the gas-condensate relative permeability curves considering viscous effects. The interplay between gravitational (originated from the difference in gas and condensate densities), viscous, and IFT effects on critical condensate saturation was investigated in their model, and they observed a significant viscous and IFT effect on relative permeability. In their model, the gravitational effect on the relative permeability was more substantial when the viscous effects were minimal. Regardless of gravitational and interfacial tension effects, wettability alteration (accounted for by using receding contact angles) caused a decrease in critical condensate saturation.

Wang and Mohanty (2000) implemented a gas-condensate pore-network model and considered two distinct flow regimes in their modeling, namely, capillary-dominated flow, and viscous and inertial-dominated flow (the latter of which was used under low condensate saturation). They investigated the effect of pore geometry and flow-dependent parameters (such as non-Darcy coefficients in higher pressure gradients) on the gas and condensate relative permeability curves. The inertial effect on gas-condensate flow has not extensively been modeled through PNM except in the work of Wang and Mohanty (2000), who included the non-Darcy product for an inertial-dominated flow regime. Their model showed that each phase's relative permeability is strongly dependent on pore morphology under capillary-dominated flow. In viscous and inertial-dominated flow, relative permeabilities of both gas and condensate phases improved, showing a positive correlation with saturation and pressure gradient.

Jamiolahmady et al. (2000) formulated a mathematical model for a conical-shaped pore and described the gas and condensate interactions based on the observed pore-scale flow patterns in high-pressure micro-models. In their model, they formulated and included the mechanisms controlling the cyclic process of gas-condensate blockage and removal observed in the past microfluidic experiments. They compared their simulation results against available core flood experimental data and found a good match between the flow rate effect in their model and the reported experimental results. However, for a better description of gas-condensate flow dynamics, they claimed that there is a need to consider possible pore-to-pore interactions to capture better the influence of parameters such as geometry, IFT, and velocity on the flow. In 2003, Jamiolahmady et al., used PNM to investigate the positive coupling effect controlled by viscous and capillary forces observed in core experiments in low and high IFT ranges. The implemented dynamic

pore-network model was used to quantify the positive coupling effect on gas relative permeability, K_{rg} , and condensate relative permeability, K_{rl} . They found that the positive coupling effect on K_{rg} is more than K_{rl} . Furthermore, they noticed the higher the IFT values, the lower the coupling effect is. Moreover, the increase in condensate saturation was observed in the rise in velocity.

Momeni et al. (2017) employed a 3D PNM of dynamic gas-condensate flow, which partly reproduced the experimental data of Jamiolahmady et al. (2003). They simulated the impact of flow rate and IFT on relative permeability curves by building a steady-dynamic model to capture the positive effect of velocity and its reduction in higher IFT values reported in the literature. They compared their model simulations with Jamiolahmady et al. (2003) model as a representative pore-network model. They simulated, through PNM, the gas-condensate fluid flow based on PVT sample data from literature and confirmed the positive effect of velocity on the gas-condensate flow. However, it was not stated whether the steady state gas-condensate flow had been achieved or not.

Labed et al. (2018) constructed a PNM model to describe the gas and condensate phase behavior in a porous shale medium and analyze the flow pattern and the effect of the pore sizes. Because of the dominant interaction of gas molecules with the pore walls, the gas flow behavior in the porous shale medium is strongly related to the distribution of pore sizes and reservoir pressure. Assuming a smaller effect of capillary force and adsorption of the gas on phase change, they investigated the effect of condensate saturation and its blockage on Knudsen flow. They also determined a relative correction factor for the relative permeability of gas to relate the pressure and condensate saturation to the Knudsen flow. This factor was defined to quantify the Knudsen effect and compare the impact of gas-condensate and dry gas flow. The gas-condensate flow was evaluated by comparing apparent gas-condensate permeability and Darcy gas-condensate permeability. The dry gas flow was, however, assessed by comparing the apparent permeability of dry gas and dry gas permeability in the Darcy flow. They concluded that when condensate saturation in the shale matrix is high, the gas flow pattern is not influenced by the Knudsen effect. The condensate blockage during reservoir pressure decline was strongly related to the statistical distribution of pore radius. Their results showed that the relative correction factor reflecting the Knudsen effect is reduced when the reservoir pressure drops into the retrograde condensation zone. The summary of their pore-network results is provided in Table 4.

The dynamic compositional pore-network model is a recent

Table 4

The impact of various physical factors and geometrical parameters on Knudsen flow studied by pore-network modeling of shale gas-condensate reservoir (Labeled et al., 2018).

Condensate saturation	Mean of pore size distribution	Condensate blockage	Standard deviation of pore size distribution	Coordination number	Reservoir pressure
-	+	+	-	+	+

approach to address phase behavior and study the effect of micro-scale parameters on the gas-condensate flow. Santos and Carvalho (2020) developed a gas-condensate pore-network model for pore-scale simulation of retrograde condensation. The pore network formulation was implemented to describe the transport of components in the gas and condensate through the network at a specified reservoir temperature. The model was used to analyze the flow regime under high capillary number and low IFT within the wellbore region. Their model was applied to estimate the relative permeability of gas and condensate along a 0.3-m pore-network length under different pressure gradients below dew point pressure corresponding to different saturation levels. Under high capillary number flow, the flow regime was defined such that condensate embraces the gas phase and flows attached to the pore walls in the straight circular-shaped capillaries. Considering a viscous-dominated flow, and in the absence of processes such as snap-off, the main feature of their model was to reach a stabilized flow pattern of gas and condensate after several time steps. The core-annular flow was stabilized due to the sample spanning of gas flow in the middle of throats and the condensate film flows at the wall of pore throats. Using a 3D dynamic PNM, Chen et al. (2020) simulated the drainage process (injection of a gas mixture into a medium filled initially with liquid phase) where the effect of the phase change (condensation and vaporization) on the flow patterns was studied. Two gas-condensate fluid compositions including a binary (C1–C5) and a ternary (C1–C5–CO₂) fluid composition were considered. They constructed a 3D site model assuming only the pore bodies volume for two simulations (using square-tube and cubic) with square cross-sectional shapes to study pore invasion and explore fingering effects on the drainage displacement front. The gas saturation and gas invasion patterns were influenced and changed in their model by liquification of the injected gas phase and vaporization of the residual heavier component in the liquid phase. They concluded that condensation induced by phase change influences the gas invasion pattern and can lessen the viscous fingers. Reis and Carvalho (2020) developed a compositional model to study the wettability change effect on the condensate banking, improving Santos and Carvalho's (2020) model by adding the capillary force contributions in formulations for higher IFT values when the reservoir pressure sufficiently declines. Although several pore-network studies considered spatially varying contact angles (e.g., Foroughi et al., 2020; Chen et al., 2021; Raeini et al., 2022), Reis and Carvalho (2020) applied the wettability effect using simulations with the contact angles distributed uniformly in each case (i.e., no spatial variation of wettability was assumed). Furthermore, they not only analyzed the wettability effect on the gas-condensate relative permeability but also considered various phase change conditions (i.e., different pressure levels), and velocity fields (i.e., through applying different flow rates). Wettability alteration was quantified by taking different contact angles below 90° for a range of liquid-wet mediums considering the film flow followed by the formation of the condensate bridges at the capillary middle sections, and above 90° for the gas-wet medium, representing the flow of condensate droplets followed by the creation of condensate slugs in the thin section of capillaries (see Table 6, where contact angle was considered in the term of capillary pressure difference along the condensate bridge/slug presented in equations 6.35 and 6.43). The cycle of closing and opening of a capillary as a result of the movement of the condensate bridge was modeled using a continuous step-function depending on the pressure difference along the throat and its gas saturation. The blockage of the narrow section of a capillary occurred when either condensate thickness exceeded 25% of the capillary radius or met

a non-wetting break-up criterion proposed by Beresnev et al. (2009) for sinusoidal capillary channels (see Table 7). The key limitation noted in their work was that the effect of wall roughness was not included. Moreover, for gas-wet scenarios, they assumed that condensate slugs were forming at the early condensation stages, where gas saturation is close to 1. They stated that the slug flow pattern in condensate-carrying porous media could be characterized similarly to the observations in hydrophobic microchannel flow studies (Chen and Cheng, 2005; Fang et al., 2010; Cubaud et al., 2006; Wu and Djilali, 2012). These slug flow configurations have been based on microfluidic experiments with liquid-air systems flowing in high Reynolds numbers in micro-channels. Finally, they had only a qualitative comparison of the wettability effect against the core flood experiments conducted on gas-condensate media, which could be due to the lack of knowledge on what happens internally within such media. Potentially, future imaging studies of gas-condensate systems could shed light on the evolution of slug flow, and micromodel studies under high pressures could provide valuable direct observations. The main results derived from the pore-network model for the dynamic gas-condensate flow were consistent with the experimental findings from the literature (showing a positive flow rate impact and a negative effect of IFT on the relative permeability). Furthermore, PNM revealed the significant effect of wettability change, velocity, and pressure level on improving the gas-condensate relative permeability. Reis and Carvalho (2020) also observed that in an intensely wet medium, at high levels of condensation, accumulation of heavy components will lead to reservoir fluid compositional shift to a volatile oil. Recently, Reis and Carvalho (2021) analyzed the impact of velocity, and IFT on relative permeability curves of the completely liquid-wet medium with the same compositional model developed earlier by their group. They compared the obtained relative permeability curve in a completely liquid-wet medium with those reported in the past PNM studies as well as available experimental data of core flood experiments. Annular condensate thin film flow was modeled together with the condensate bridges. They presented their results at two pressure levels resulting in two different IFTs. They simulated flow in three gas velocities and also included the snap-off mechanism. However, in their new model, they considered only a binary mixture for reservoir fluid. In conclusion, their pore-network model results were validated quantitatively with experimental core-flood data confirming their considered mechanisms for the condensate blockage at the pore scale. In another study, Reis and Carvalho (2022) presented the production performance under different injection strategies and for different gas types by using a similar compositional pore-network model. They modeled the condensate blockage caused by a typical gas-condensate reservoir fluid with six components followed by injection of different gas types at the inlet face of the network. The effect of pure gas injection, as well as injection of the mixture of produced gas and pure gases on the vaporization of heavier components, was investigated. They simulated gas-condensate flow at different pressure levels of the reservoir representing different degrees of condensate blockage. At a specific flow rate, and disregarding the IFT effect, they presented the improvement caused by different gas injection strategies through a compositional fluid model at different levels of condensate saturation examined in terms of heavy components present in the network outflow (i.e., as a proxy of condensate evaporation). Although the effect of IFT on the vaporization process was overlooked, they emphasized the role of gas recycling and gas injection strategy as a remedy for the problem of condensate blockage at the pore scale. Hereafter, a close look at the utilized geometries and topological structure of the pore-network models used to study gas-condensate will

be presented, followed by a discussion of the formulation of physical processes and the involved mechanisms.

2.2. Development of pore networks: geometry and pore structure

A realistic characterization of pore space structure and morphology is essential in the simulation of multiphase flow. In this section, previous gas-condensate pore-network modeling studies have been reviewed based on their pore space descriptions in terms of pore network topology and geometry. Pore space conceptualization in pore-network models has evolved from statistically equivalent and structured regular pore networks to those captured by pore space imaging techniques, pore-network extraction algorithms, and multiphase interface tracking techniques (Al-Gharbi and Blunt, 2005; Moebius and Or, 2014). More details can be found in Golparvar et al. (2018). As pore space geometry and topology have significant effects on multiphase flow patterns, the pore structure parameters involved in the representation of pore networks have been varied and subjected to sensitivity analysis in the PNM of gas-condensate flow (Mohammadi et al., 1990; Wang and Mohanty, 1999; Bustos and Toledo, 2003a,b; Labeled et al., 2018). For gas-condensate flow modeling, pore geometry has been selected from simple 2D and 3D networks with circular cross-section tubes to more representative geometrical shapes and network topologies extracted from core samples. Mohammadi et al. (1990) presented a 2D pore-network model to simulate the pore-scale rules inferred from microfluidic observations. The pore-scale rules were applied to determine the distribution of the condensate phase in the pore space, including the pore corners and crevices. The pore geometry of both angular and circular shapes was considered, the former of which was capable of capturing phase entrapment. Their network topology was a Bethe Tree network, in which fluid transport was analyzed through void volume-assigned pore throats; whereas, pore bodies were assumed to act as just volumeless joints (nodes) with no resistance to flow. The network pore size distribution was based on statistical functions, and a variety of geometrical, morphological, and statistical parameters, as well as physical mechanisms including the fluid entrapment were introduced to study their effect on gas-condensate relative permeability. They noted that the geometry of throats (assumed therein as tetrahedral) strongly controls phase entrapment within the network. Fang et al. (1996) constructed a 2D pore network of circular-shaped pores of different sizes. Their network was vertically aligned, and the radius of the tubes was randomly assigned. They considered the gas and condensate flow in both single tubes and pore-throat junctions to quantify the geometry effect on the evolution of condensation in the network (i.e., void volume was assigned to both pores and throats). Their study analyzed the critical condensate saturation and condensate flow in various tube geometries (circular, triangular, and arced triangles). Wang and Mohanty (1999) used two types of pore network construction schemes, one based on a sphere packing and another one using a cubic model with a square cross-section and converging-diverging profile (Fig. 1b). In the cubic model, the corners did not have any links to each other to maintain low condensate saturations. The topology of the sphere packing model was defined as an equivalent model to a Berea sandstone, and statistical properties of the model were assigned based on Weibull distribution.

Li and Firoozabadi (2000) also utilized a 2D network with circular capillary tubes, similar to that of Fang et al. (1996) assigning cubic shapes to the intersection of capillary tubes, thereby, considering the pore body volume in the network. However, Wang and Mohanty (2000) implemented a 3D pore-network model to analyze gas-condensate dynamic flow in which throats had converging-diverging profiles with square cross-sections instead of cylindrical shapes used in the other studies. In both models developed by Wang and Mohanty (1999, 2000) they assigned volume to both pore bodies and throats to investigate the structural and morphology effects on the gas condensation process. Jamiolahmady et al. (2000) first modeled condensate formation in a single conical-shaped pore, and in a later study, in 2003, they upgraded

their unit cell model to a 3D bond model (i.e., nodes were considered volumeless and gas and condensate phases were only distributed inside the pore throats) analyzing the behavior of condensate flow at steady state conditions. Their model had circular-shaped pores with a constant outlet radius/inlet radius ratio equal to 0.3 for all pores. In their model, the equivalent pore throat length was considered as an additional geometrical parameter to account for the effect of flow resistance and pore tortuosity on condensate film flow (considered as a thin film on pore walls) in cylindrical capillaries in the network. Bustos and Toledo (2003a,b) described the model geometry with a square cross-section in which the condensate phase could form a wedge in the pore corners. Later on, the triangular and octahedral cross sections were also included in their 3D model to study the effect of angularity on gas-condensate relative permeabilities (Bustos and Toledo, 2004). Different distribution functions were selected to assign the size of pore segments statistically. Pore bodies were considered volumeless junctions (nodes) with infinite conductance, while throats having volumes contributed to the gas-condensate flow. Contact angle hysteresis was allowed in vertical pore segments, which were adopted by advancing and receding contact angles. The pore segment length, L , was selected such that the pore segment could hold the highest stable condensate column without overflowing.

Momeni et al. (2017) also presented a cubic 3D bond model taking only throat volume into consideration with a square cross-sectional area to study the dynamic aspects of gas-condensate flow. As a bond model, Labeled et al. (2018) also defined a 3D cubic pore network with randomly assigned pore sizes in which pore junctions assumed to have infinite conductivity. In their simple model (with a small pore-network model of size $8 \times 8 \times 8$), pore radii with a circular cross-sectional shape were assigned randomly by a log-normal distribution. Santos and Carvalho (2020) developed a pore-network model consisting of only one layer of spherical pores and cylindrical throats. To consider pore bodies and throats volume, they constructed a pore-throat model, assigning a control volume to each pore body, incorporating also the volume of half of the throats that enter the pore body.

Chen et al. (2020) constructed two types of 3D pore-network models one with square tube and another with cubic pore bodies connected by square cross-sectional pore throats. The pore size (i.e., inscribed radius) and coordination number distributions were adopted from sand packs in the literature. The pore throat inscribed radius was considered as half of the connecting smaller pore bodies at each side. The pore bodies were assigned volume, facilitating the tracking of phase interfaces within pore bodies while the pore throats were assumed volumeless. It should be noted, however, that the snap-off phenomenon was considered in the throats, controlling the gas phase connectivity. As the square cross-section was selected for the pore throat geometry, they considered the phase invasions using entry capillary pressure and the snap-off process by definition of snap-off threshold capillary pressure given in Tables 6 and 7 respectively. In a recent development for pore network structure, Reis and Carvalho (2020) considered a 3D pore-network model composed of circular capillaries with a converging-diverging profile for the compositional modeling of condensate flow and inspecting the effect of wettability change. They have assigned volumes of the contiguous throats to a pore to that pore; this has been done through a control volume centered at each pore, to which the volume of that pore and half of the volume of throats entering the pore has been assigned. Similar to Chen et al. (2020) model, in this model snap-off criterion has been considered as well. They selected capillary (throat) elements of varying cross sections (i.e., converging-diverging profile with the narrowest part defined in the middle, and diverging parts at both ends). The pore-network properties such as pore and throat sizes and aspect ratios were distributed based on the statistical distributions extracted from a digital Berea core sample. The same procedure was followed by Reis and Carvalho (2021, 2022).

The pore structures taken in gas-condensate modeling are categorized based on their cross-sectional shape, cross-sectional angularity,

network lattice type, and dimension, as well as network type in Table 5. The entry pressure, P_e (the capillary pressure beyond which the viscous or gravity force overcomes the capillary force for a given pore geometry), is presented in Table 6 for different pore geometries. In addition, Table 6 shows the phase conductance terms based on geometry and phase occupancies. The conductance term is used to calculate gas flow and condensate film/corner flow rates often based on Hagen-Poiseuille's law. In Table 7 the non-wetting phase snap-off pressure, P_s , is given for different capillary geometries utilized in gas-condensate pore-network models in the literature.

2.3. Gas-condensate pore-network modeling development: processes and condensation implementation

Simulation of gas-condensate flow through the pore network under local rules derived from observed experimental phenomena in the pore spaces has been a challenging task in the past. That is why, different models were developed and employed to predict the gas-condensate

flow behavior established based on different assumptions for condensate formation and pore scale displacement mechanisms. In the following, the applied models to simulate gas-condensate flow at the pore scale are extensively described to explore more specifically the involved processes and procedures, which have been used to obtain the macroscopic parameters such as critical condensate saturation as well as gas-condensate relative permeabilities.

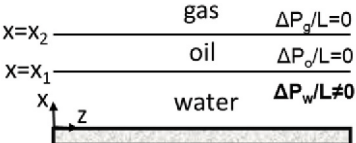
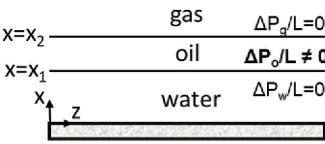
2.3.1. Quasi-static pore-network modeling

The quasi-static pore-network models are capable of simulating equilibrium states of microscale flow processes while neglecting time variant events between those equilibrium states. However, the states between equilibrium conditions are applied by incremental global pressure change. These models are widely used to study two-phase flow transport in porous media where the pressure is considered uniform in each phase and the interfacial pressure difference is governed by the Laplace equation and the flow is only governed by interfacial forces (Thompson, 2002; Primkulov et al., 2018). The quasi-static approach is

Table 5
Pore structure and geometry developments in pore-network modeling of gas-condensate flow.

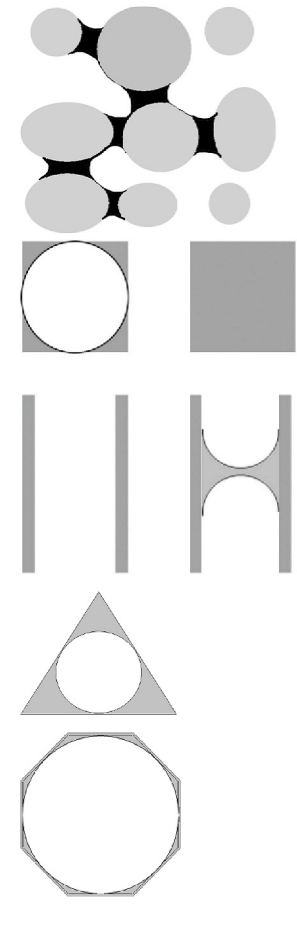
Geometry	Cross-section category	Circular shaped cross section					
	Cross-section shape	Circular shape capillary tubes	Circular shape capillary tubes	Circular conical	Circular conical	Circular tubes	Circular
	Pore size distribution	Log-normal distribution	Log-normal size distribution	Not applicable	Weibull distribution	Log-normal distribution	Uniform
	Lattice type	Square (20 × 20)	Square (20 × 20)	Single pore	Regular cubic lattice (20 × 25 × 25)	Cubic network (8 × 8 × 8)	Regular square lattice (50 × 20)
	Pore-network specification (R = radius, Z = coordination number, μ = average throat size, SD = standard deviation of throat size, PV = pore volume, L = capillary length, ϕ = porosity)	$\mu = 23.06 \mu\text{m}$ and $\text{SD} = 5.74 \mu\text{m}$ PV = 8.89mm^3 , L = 6000 μm	$\mu = 23 \mu\text{m}$ and $\text{SD} = 5.74 \mu\text{m}$ PV = 8.93mm^3 , L = 6000 μm	$R_{\text{in}} = 6 \mu\text{m}$, $R_{\text{out}} = 10 \mu\text{m}$, L = 100 μm	Z = 3, $R_{\text{out}}/R_{\text{in}} = 0.3$, $1.28 \mu\text{m} < R_{\text{throat}} < 19.21 \mu\text{m}$, L = 28.3 μm	Z = 6, $\mu = 10 \text{nm}$, $\text{SD} = 0.6 \text{nm}$, L = 142.8 nm , $\phi = 0.08$	$20.7 \mu\text{m} < R < 25.3 \mu\text{m}$, L = 6000 μm
	Dimension	Vertical 2D	Vertical 2D	Horizontal 2D	3D	3D	Horizontal 2D
	Network type	Site-bond model	Site-bond model	Single pore	Bond model	Bond model	Site-bond model
Author		Fang et al. 1996	Li and Firoozabadi 2000	Jamiolahmady et al. 2000	Jamiolahmady et al. 2003	Labeled et al. 2018	Santos and Carvalho 2020
Geometry	Cross-section category	Angular-shaped cross section					
	Cross-section shape	Square, triangular and octahedral cross-sections	Convex polyhedral and cylindrical	Bipyramidal with a square cross-section	Polygonal cross-section	Network#1: tube-shaped with square cross section Network#2: cubic pore bodies	
	Pore size distribution	Uniform, normal, log-normal	Rayleigh function/Truncated Normal Distribution (TND)	Weibull distribution	Weibull distribution	Adopted from sand pack distributions in the literature	
	Lattice type	Regular square/cubic lattice (60 × 60 and 20 × 20 × 20)	The Bethe Tree network	Modified sphere-pack model (MSPM) and a cubic model (CM) (20 × 20 × 20)	Regular cubic lattice (35 × 35 × 35)	Regular cubic lattice (Network#1: 10 × 10 × 10, Network#2: 20 × 20 × 20)	
	Pore-network specification	$\mu = 80$ and $55 \mu\text{m}$, $\text{SD} = 8-50 \mu\text{m}$, L = 300 μm	Not mentioned	$0 < R_{\text{throat}} < 22 \mu\text{m}$, $10 \mu\text{m} < R_{\text{pore}} < 35 \mu\text{m}$, L = 100 μm	Z = 6, $4.8 < R_{\text{throat}} < 16.2 \mu\text{m}$	Network#1: Z = 4.5, Network#2: Z = 5.2 $10 \mu\text{m} < R_{\text{pore}} < 50 \mu\text{m}$, $4 \mu\text{m} < R_{\text{throat}} < 24 \mu\text{m}$	
	Dimension	2D/3D	Horizontal	3D converging-diverging elements	3D	3D	
	Network type	Bond model	Bond model	Site-bond model	Bond model	Site model	
Author		Bustos and Toledo 2003, 2004	Mohammadi et al. 1990	Wang and Mohanty 1999	Momeni et al. 2017	Chen et al. 2020	
Geometry	Cross-section category	Converging-diverging profile					
	Cross-section shape	Bipyramidal with a square cross section		Converging-diverging circular		Converging-diverging circular	
	Pore size distribution	Weibull distribution		Adapted from image sample		Adapted from aspect ratio (AR) of image sample	
	Lattice type	Regular cubic lattice (20 × 20 × 20)		Sub-cubic extracted network		A cubic lattice of 20 × 25 × 25	
	Pore-network specification	$0 < R_{\text{throat}} < 22 \mu\text{m}$, $10 \mu\text{m} < R_{\text{pore}} < 35 \mu\text{m}$, L = 100 μm		$0.9 \mu\text{m} < R_{\text{min}} < 39 \mu\text{m}$, $0.9 \mu\text{m} < R_{\text{max}} < 74 \mu\text{m}$, Network Volume = 1.75 mm^3 , Z = 2.72, $\phi = 0.171$		$1 \mu\text{m} < R_{\text{min}} < 19.5 \mu\text{m}$, Z = 3, L = 75 μm	
	Dimension	3D, converging-diverging elements		3D		3D	
	Network type	Site-bond model		Pore-throat model		Pore-throat model	
Author		Wang and Mohanty 2000		Reis and Carvalho 2020, 2022		Reis and Carvalho 2021	

Table 6
Structural-process effects on gas-condensate phase distribution: the associated entry pressure and flow conductance term calculation relationships.

Selected Geometry	Entry Pressure	Flow Conductance (The term g , refers to flow conductance)	Author
Circular cross-section, Horizontal capillary	<p>Criterion for condensate bridge displacement:</p> $P_R - P_A \geq \frac{2\sigma}{R} (\cos \theta_R - \cos \theta_A), \dots (6.1)$ $P_{entry} = \frac{2\sigma}{R} (\cos \theta_R - \cos \theta_A), \dots (6.2)$ <p>where θ_R and θ_A are referring to receding and advancing contact angles, σ refers to interfacial tension, R refers to the capillary radius and P refers to pressure.</p>	<p>Hughes and Blunt (2000)</p> $g_g = \frac{\pi R_{eff}^4}{8\mu_g L}, \dots (6.3)$ <p>where R_{eff} is the effective radius of (non-wetting phase) gas phase and μ_g is the gas viscosity.</p>	<p>Li and Firoozabadi (2000)</p>
Circular cross-section, Vertical capillary	<p>Criterion for condensate bridge displacement: $h \geq h_{cc} =$</p> $\frac{2\sigma}{\Delta\rho g R} (\cos \theta_R - \cos \theta_A) - \frac{(P_R - P_A)}{\Delta\rho g}, \dots (6.4)$ <p>where h_c is the height of liquid bridge in a circular tube after formation and h_{cc} is the critical height of liquid column before movement.</p> $P_R - P_A \geq \frac{2\sigma}{R} (\cos \theta_R - \cos \theta_A) - \Delta\rho g h, \dots (6.5)$ $P_{entry} = \frac{2\sigma}{R} (\cos \theta_R - \cos \theta_A) - \Delta\rho g h, \dots (6.6)$ <p>where ρ is the density, g is the acceleration of gravity and h is the height of fluid column.</p>	$g_l = 0 \quad (S_l \leq S_{lc}), \dots (6.7)$ $g_l = \frac{\pi R^4}{8\mu_l L} \quad (S_l = 1), \dots (6.8)$ $g_l = \frac{\pi R^4}{8\mu_l L} \left(S_l + \frac{\mu_g}{\mu_l} (1 - S_l) \right)^{-1} \quad (S_l > S_{lc}), \dots (6.9)$ $g_g = \frac{\pi R^4}{8\mu_g L} \left(1 - S_l + \frac{\mu_l}{\mu_g} S_l \right)^{-1} \quad (S_l > S_{lc}), \dots (6.10)$ <p>where R is the radius of capillary tube, S_{lc} is the critical liquid (i.e., condensate) saturation, l and g are referring to liquid (i.e., condensate) and gas phase, and S is the saturation term.</p>	<p>Li and Firoozabadi (2000)</p>
Sphere packing	$\Delta P_c = 2\sigma \left(\frac{1}{R_1} - \frac{1}{R_2} \right), \dots (6.11)$ <p>Criterion for condensate bridge movement: $h_{max} =$</p> $\frac{2\sigma}{R_t \Delta\rho g} = \frac{2K}{N_B R_t}, \dots (6.12)$ $N_B = \frac{\Delta\rho g k}{\sigma}, \dots (6.13)$ $P_{entry} = 2\sigma \left(\frac{1}{R_1} - \frac{1}{R_2} \right), \dots (6.14)$ <p>where R_t, N_B, k, R_1 and R_2 are throat radius, Bond number, permeability, and liquid bridge radius of curvatures respectively.</p>	<p>Mani and Mohanty (1998):</p> <p>Single phase conductivity: $g_{lg} = \frac{\pi R_t^4}{8\mu L} \quad (S_{lg} = 1), \dots (6.15)$</p> <p>The Navier-Stokes equations were solved for two transport cases to calculate average velocities with assigned phase pressure gradients and boundary conditions:</p> <p>Case 1: water thin film conductivity:</p>	<p>Wang and Mohanty (2000)</p>
			
		<p>The average water velocity, \bar{v}_w over the water film thickness x_1:</p> $\bar{v}_w = \frac{x_1^2 \Delta P_l}{3\mu_l L}, \dots (6.16)$ <p>Case 2: oil thin film conductivity:</p>	
			
		<p>The average oil velocity:</p> $\bar{v}_o = \frac{\Delta P_o}{3\mu_o L} \left[\frac{1}{3} (x_2^2 + x_1 x_2 + x_1^2) - x_1 x_2 + \frac{\mu_o}{\mu_w} x_1 (x_2 - x_1) \right], \dots (6.17)$	

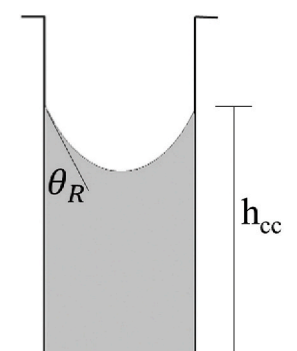
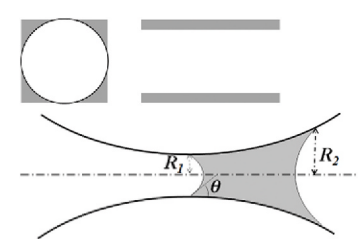
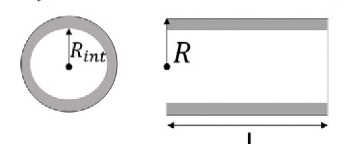
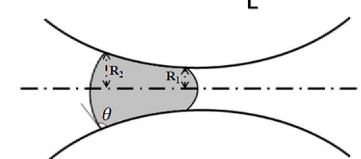
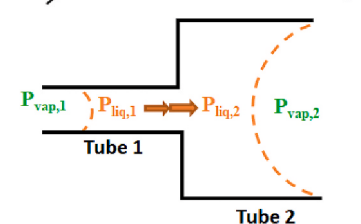
(continued on next page)

Table 6 (continued)

Selected Geometry	Entry Pressure	Flow Conductance (The term g, refers to flow conductance)	Author
<p data-bbox="129 606 276 718">Capillaries with square, triangular and octahedral cross-sections</p> 	<p data-bbox="702 606 1064 630">Criterion for condensate bridge movement:</p> $P_{entry} = \frac{2\sigma}{R} (\cos \theta_R) - \rho g h_{cc}, \dots (6.18) h_{cc} = \frac{2\sigma}{\rho g R_t} \cos \theta_R, \dots (6.19)$ <p data-bbox="702 694 1170 742">where h_{cc} is the critical height of condensate bridge formed in the vertical capillary tube with the radius, R.</p>	$g_g = \frac{\pi R_{eff}^4}{8\mu_g L}, \dots (6.20)$ $g_l = \frac{V_l r_l^2}{\beta \mu_l L^2}, \dots (6.21)$ $R_{eff} = \frac{1}{2} \left(R_t + \sqrt{\frac{a}{\pi}} \right), \dots (6.22)$ <p data-bbox="1170 710 1830 805">where l and g are referring to liquid (i.e., condensate) and gas phase respectively, a is referring to the area of the pore cross-section, R_t is inscribed capillary radius,</p> $V_l = n_c A_c L = n_c r_l^2 L \left[\sin(\alpha + \theta) \cos(\alpha + \theta) + \frac{\cos^2(\alpha + \theta)}{\tan(\alpha)} - \frac{\pi}{2} + \alpha + \theta \right], \dots (6.23)$ $A_c = \frac{A(1 - S_g)}{n_c}, \dots (6.24)$ <p data-bbox="1170 893 1830 1045">V_l is referring to the condensate volume residing in the capillary corners, n_c is referring to the number of corners for square cross section, r_l is referring to the meniscus radius of curvature defined in the capillary corner as $r_l = \frac{\sigma}{P_c}$ in which σ, and P_c are the interfacial tension and the capillary pressure respectively. Other parameters are the pore length, L, the pore corner half-angle, α, and the contact angle, θ.</p> <p data-bbox="1170 1045 1659 1069">The resistance factor, β is defined as the following expression:</p> $\beta = \frac{12 \sin^2 \alpha (1 - C)^2 (\psi_1 - C\psi_2)(\psi_3 + fC\psi_2)^2}{(1 - \sin \alpha)^2 C^2 (\psi_1 - C\psi_2)^3}, \dots (6.25)$ $\psi_1 = \cos^2(\alpha + \theta) + \cos(\alpha + \theta) \sin(\alpha + \theta) \operatorname{tg} \alpha, \dots (6.26)$ $C = \left(\frac{\pi}{2} - \alpha \right) \operatorname{tg} \alpha, \dots (6.27)$ $\psi_2 = 1 - \frac{\theta}{\frac{\pi}{2} - \alpha}, \dots (6.28)$ $\psi_3 = \frac{\cos(\alpha + \theta)}{\cos \alpha}, \dots (6.29)$ <p data-bbox="1170 1252 1830 1308">$f = 0$ for gas-condensate interface, the factor f varies between 0 and 1 according to the boundary condition at the fluid interface.</p>	<p data-bbox="1830 614 1979 694">Bustos and Toledo, 2003b, 2004</p>

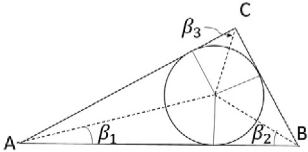
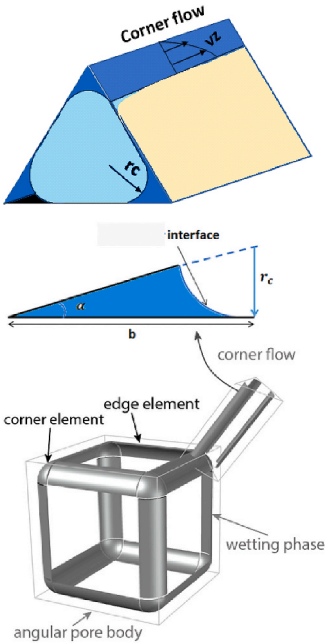
(continued on next page)

Table 6 (continued)

Selected Geometry	Entry Pressure	Flow Conductance (The term g , refers to flow conductance)	Author
 <p>Horizontal/vertical square cross-section capillary</p>	$A_c = n_c r_l^2 \left[\cos \theta (\cot \alpha \cos \theta - \sin \theta) + \theta + \alpha - \frac{\pi}{2} \right], \dots$ <p>(6.30) where A_c is the corner area of liquid l and n_c stands for the number of corners</p> $P_{entry} = P_c - (P_g - P_l) < 0, \dots (6.31)$ <p>Criterion for condensate bridge displacement:</p> $P_g > P_l + P_c = P_l + \frac{2\sigma}{R}, \dots (6.32)$ <p>where R denotes the throat radius adopted from Jamiolahmady et al. (2003)</p>	$g_g = \frac{\pi R_{eff}^4}{8\mu_g L}, \dots (6.33)$ $g_l = \frac{V_l \mu_l^2}{\beta \mu_l L^2}, \dots (6.34)$ <p>V_l is given by equation 6.23, resistance factor, β is given by equation 6.25, defined in Bustos and Toledo (2003b).</p>	<p>Momeni et al. (2017)</p>
 <p>Converging-diverging capillary (liquid-wet medium)</p>	<p>The capillary pressure difference along a condensate bridge in capillary, ij connecting pore bodies i and j:</p> $\Delta P_{ij}^{int} = \left[2\sigma \cos \theta \left(\frac{1}{R_1} - \frac{1}{R_2} \right) \right]_{ij}, \dots (6.35)$ $\Delta P_{crit} = \left[2\sigma \cos \theta \left(\frac{1}{R_1} - \frac{1}{R_2} \right) \right], \dots (6.36)$	$g_g = \frac{\pi}{8\mu_g L} (S_g R_{eq}^2)^2 + \frac{\pi}{4\mu_l L} (R_{eq}^2 - S_g R_{eq}^2) S_g R_{eq}^2, \dots (6.37)$ $g_l = \frac{\pi}{8\mu_l L} (R_{eq}^2 - S_g R_{eq}^2)^2, \dots (6.38)$ <p>where R_{eq} specifies the equivalent radius for the converging-diverging capillary.</p>	<p>Reis and Carvalho (2021, 2022)</p>
 <p>Circular cross-section capillary (liquid-wet medium)</p>	$\Delta P_{ij}^{int} = 0, \dots (6.39)$ $P_{entry} = 0, \dots (6.40)$	$g_g = \frac{\pi}{8\mu_g L} R_{int}^4 + \frac{\pi}{4\mu_l L} (R^2 - R_{int}^2) R_{int}^2, \dots (6.41)$ $g_l = \frac{\pi}{8\mu_l L} (R^2 - R_{int}^2)^2, \dots (6.42)$ <p>where R, is the capillary radius and R_{int}, is the capillary radius occupied by gas phase.</p>	<p>Santos and Carvalho (2020)</p>
 <p>Converging-diverging capillary (gas-wet medium)</p>	<p>The capillary pressure difference along a condensate slug in capillary, ij in gas-wet medium:</p> $\Delta P_{ij}^{int} = \left[2\sigma \cos \theta \left(\frac{1}{R_1} - \frac{1}{R_2} \right) \right]_{ij}, \dots (6.43)$ $\Delta P_{crit} = \left[2\sigma \cos \theta \left(\frac{1}{R_1} - \frac{1}{R_2} \right) \right], \dots (6.44)$	$g_{sf}^g = \frac{\pi R_{eq}^4}{8L} \left(\frac{S_g}{S_g(\mu_g - \mu_l) + \mu_l} \right), \dots (6.45)$ $g_{sf}^l = \frac{\pi R_{eq}^4}{8L} \left(\frac{1 - S_g}{S_g(\mu_g - \mu_l) + \mu_l} \right), \dots (6.46)$ <p>where sf refers to slug flow.</p>	<p>Reis and Carvalho (2020)</p>
 <p>Circular cross-section capillary</p>	<p>Criterion for condensate slug displacement:</p> $P_{liq,1} - P_{liq,2} > 0 \rightarrow \Delta P_g > P_{c1} - P_{c2}, \dots (6.47)$ $\Delta P_c = \sigma_{gl} \cos \theta \left(\frac{1}{R_1} - \frac{1}{R_2} \right) = \Delta P_{thr}, \dots (6.48)$ $\Delta P_{crit} = \sigma_{gl} \cos \theta \left(\frac{1}{R_1} - \frac{1}{R_2} \right), \dots (6.49)$ <p>where R_1 and R_2 are the radii of two different capillaries and ΔP_{thr} is the threshold pressure difference to allow the condensate transport from Tube 1 to Tube 2</p>	$g_{ij}^g = \frac{q_{ij}^g}{\Delta P_{ij}} = \xi_{ij} \frac{\pi R_{ij}^4}{8\mu_{ij}^g L_{ij}}, \dots (6.50)$ $g_{ij}^l = \frac{q_{ij}^l}{\Delta P_{ij}} = \frac{\pi R_{ij}^4}{8\mu_{ij}^l L_{ij}}, \dots (6.51)$ $\xi_{ij} = (1 + \alpha_{ij} K_{n,ij}) \left(1 + \frac{4K_{n,ij}}{1 - K_{n,ij}} \right), \dots (6.52)$ $\alpha_{ij} = \frac{128}{15\pi^2} (4K_{n,ij}^{0.4}), \dots (6.53)$	<p>Labeled et al. (2018)</p>

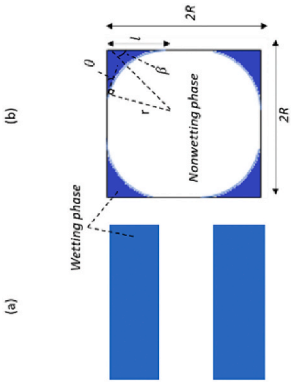
(continued on next page)

Table 6 (continued)

Selected Geometry	Entry Pressure	Flow Conductance (The term <i>g</i> , refers to flow conductance)	Author
Triangular cross-section capillary	 $P_{entry} = P_c, \dots (6.55)$ $\beta_i < \frac{\pi}{2} - \theta_r, \dots (6.56)$ $F_d = \frac{1 + \sqrt{1 - \frac{4GC}{\cos^2 \theta_r}}}{1 + 2\sqrt{\pi G}}, \dots (6.57)$ $P_c = \frac{\sigma \cos \theta_r}{r} (1 + 2\sqrt{\pi G}) F_d, \dots (6.58)$ $C = \sum_{i=1}^n \left[\cos \theta_r \frac{\cos(\theta_r + \beta_i)}{\sin \beta_i} - \left(\frac{\pi}{2} - \theta_r - \beta_i \right) \right], \dots (6.59)$ <p>where <i>G</i> is the shape factor, θ_r is the receding contact angle and β_i is the corresponding corner half angle.</p>	$K_n = \frac{\lambda}{R}, \dots (6.54)$ <p>where <i>g</i>, <i>R</i>, λ and K_n are referred to conductance, tube radius, the average minimum free path and the Knudsen number respectively. The index <i>ij</i> refers to a capillary connecting node <i>i</i> to node <i>j</i>.</p> <p>Corner wetting-phase conductance for the corresponding corner half angle, β: $g_{pc} = C \frac{A_c^2 G_c}{\mu_p}$, (<i>p</i> = phase, <i>c</i> = corner), $\dots (6.60)$</p> <p>Corner area for the wetting phase:</p> $A_c = \left(\frac{b_i \sin \beta}{\cos(\theta_i + \beta)} \right)^2 \left(\frac{\cos \theta_i \cos(\theta_i + \beta)}{\sin(\beta)} + \theta_i + \beta - \frac{\pi}{2} \right), \dots (6.61)$ $G_c = \frac{A_c}{4b_i^2 \left(1 - \frac{\sin \beta}{\cos(\theta_i + \beta)} \left(\theta_i + \beta - \frac{\pi}{2} \right) \right)^2}, \dots (6.62)$ $C = 0.364 + 0.28 \frac{G^*}{G_c}, \dots (6.63) \quad b_i = R \frac{\cos(\theta_a + \beta_i)}{\sin(\beta_i)}, \dots (6.64)$ $G^* = \frac{\sin \beta \cos \beta}{4(1 + \sin \beta)^2}, \dots (6.65)$ $g^* = \frac{g\mu}{r_c^3} = \int \frac{v_z^3 da^*}{A^*}, \dots (6.68)$ <p>where g^* is the conductance term in non-dimensional form, which is only in relation to the corner half angle (the contact angle is zero).</p>	Piri (2003) Valvatne and Blunt (2004), ^a
Triangular cross-section capillary	 $P_{entry} = p_{ij}^{entry}, \dots (6.66)$ <p>Capillary pressure in the corner flow:</p> $P_c = P_n - P_w = \sigma_{wn} \left(\frac{1}{R_1} + \frac{1}{R_2} \right) = \frac{2\sigma_{wn}}{r_c}, \dots (6.67)$ <p>where r_c is the average radius of curvature.</p>	$g^* = \frac{g\mu}{r_c^3} = \int \frac{v_z^3 da^*}{A^*}, \dots (6.68)$ <p>where g^* is the conductance term in non-dimensional form, which is only in relation to the corner half angle (the contact angle is zero).</p>	Raouf and Hassanizadeh (2012), ^a

(continued on next page)

Table 6 (continued)

Selected Geometry	Entry Pressure	Flow Conductance (The term g, refers to flow conductance)	Author
<p>Network#1: tube-shaped with square cross section Network#2: cubic pore bodies</p>	 $P_{entry} = P_{ij}^{entry} = \frac{\sigma}{R_{ij}} \left(\cos \theta + \sqrt{\sin \theta \cos \theta + \frac{\pi}{4} - \theta} \right), \dots \quad (6.69)$	<p>Single α-phase conductance: $g_{ij}^{\alpha} = \frac{0.5623 G_{ij} (A_{ij}^{\alpha})^2}{\mu_{ij}^{\alpha} L_{ij}}$, ($\alpha$ = phase),... (6.70)</p> $G_{ij} = \frac{A_{ij}}{(C_{ij})^2}, \dots (6.71)$ <p>Two-phase non-wetting phase (nw) conductance: $g_{ij}^{nw} = \frac{0.5623 G_{ij}^{nw} (A_{ij}^{nw})^2}{\mu_{ij}^{nw} L_{ij}}$, ... (6.72)</p> $C_{ij}^{nw} = 8 \left[R_{ij} + r_{ij} \left(-\frac{\sin(\pi/4 - \theta)}{\sin(\pi/4)} + \frac{\pi}{4} - \theta \right) \right], \dots (6.73)$ $A_{ij}^{nw} = 4R_{ij}^2 - 4r_{ij}^2 \left[\frac{\sin(\frac{\pi}{4} - \theta)}{\sin(\frac{\pi}{4})} \cos \theta - \left(\frac{\pi}{4} - \theta \right) \right], \dots (6.74)$ <p>$r_{ij} = P_{ij}^c / \sigma$, ... (6.75), radius of curvature of arc meniscus in the capillary, ij P_{ij}^c is set equal to the P^c of the upstream pore body with higher capillary pressure, i. e., $P_{ij}^c = \max(P_i^c, P_j^c)$, ... (6.76) (Joekear-Niasar et al., 2010a).</p> <p>Corner wetting-phase (w) conductance: $g_{ij}^w = 4 \frac{2 \tilde{g}_{ij}^w A_{ij}^w}{\mu_{ij}^w L_{ij}}$, ... (6.77)</p> $\tilde{g}_{ij}^w = \exp \left\{ \left[-18.2066 (\tilde{G}_{ij}^w)^2 + 5.88287 \tilde{G}_{ij}^w - 0.351809 + 0.02 \sin(\beta - \pi/6) \right] / \left(\frac{1}{4\pi} - \tilde{G}_{ij}^w \right) + 2 \ln \tilde{A}_{ij}^w \right\}, \dots (6.78)$ $\tilde{G}_{ij}^w = \frac{\tilde{A}_{ij}^w}{4 \left[1 - \left(\theta + \beta - \frac{\pi}{2} \right) \sin \beta / \cos(\theta + \beta) \right]^2}, \dots (6.79)$ $\tilde{A}_{ij}^w = \left[\frac{\sin \beta}{\cos(\theta + \beta)} \right]^2 \left[\frac{\cos \theta \cos(\theta + \beta)}{\sin \beta} + \theta + \beta - \frac{\pi}{2} \right], \dots (6.80)$	<p>Chen et al. (2020)</p>

^a The model was selected from PNM of the two-phase system to compare entry pressure and conductance for triangular and square cross-sectional geometry.

Table 7
Snap-off criteria for capillary condensation.

Geometry	Snap-off pressure, P_s	Author
Convex polyhedral, bipyramidal with a square cross section as well as circular	$R_p = \text{constant threshold radius } \dots(7.1)$	Mohammadi et al. (1990), Fang et al. (1996), Wang and Mohanty (1999, 2000), Li and Firoozabadi (2000)
Square cross section	$P_s = \frac{\sigma \cos(\alpha + \theta)}{R_t \cos \alpha}, \dots(7.2)$ where R_t is the throat inscribed radius.	Bustos and Toledo (2003b)
Circular cross section	A correlation of evolution time for condensate bridge formation and blockage was derived from their mechanistic model, $t_{ev} = 0.387 \left(\frac{\mu_l R^{in}}{\sigma}\right) \left(\frac{R^{out}}{R^{in}}\right)^{5.632} \left(\frac{L}{R^{in}}\right)^{0.410} \left(\frac{h_{ini}}{R^{in}}\right)^{-4.538}, \dots(7.3)$ where each capillary was assumed as a conical shape with radii of R^{in} and R^{out} with circular cross section with initial condensate thickness of h_{ini} .	Jamiolahmady et al. (2003)
Square cross section	$P_{sh} = \frac{\sigma}{2R} (\cos \theta - 2 \sin \theta \tan \alpha), \dots(7.4)$ **For regular shapes (square or equilateral triangular cross section), they referenced to Hughes and Blunt (2000): $P_c = \frac{\sigma}{R_t} (\cos \theta - \sin \theta \tan \alpha), \dots(7.5)$	Momeni et al. (2017)
Converging-diverging capillary	Critical condensate film (uniformly attached to the pore surface) thickness (t_{crit}) was assumed at either $0.25R_{min}$ thickness of condensate for each capillary or when satisfying the fluid break-up in constricted capillaries at: $L > 2\pi\sqrt{(R_{max} - e)(R_{min} - e)}, \dots(7.6)$ where e is the current thickness of condensate and L is the capillary length.	Reis and Carvalho (2020, 2022)
Equilateral triangle cross section	For $\theta \leq \frac{\pi}{2} - \alpha$ $P_s = \frac{\sigma}{R_t} (\cot \alpha \cos \theta - \sin \theta), \dots(7.7)$	Piri and Blunt (2005), ^a Spontaneous imbibition
Square cross section	$P_s = \frac{\sigma \sin(\pi/4 - \theta)}{R_t \sin(\pi/4)}, \dots(7.8)$	Chen et al. (2020)

^a The model was selected from PNM of the two-phase system to compare snap-off pressure for the geometry of the triangular and square cross-section.

applicable in simulating solute transport in complex pore-scale models and can be used as a predictive tool to analyze the effect of pore/nanoscale geometry, structure and wettability on macroscopic properties of the porous medium (Heiba et al., 1983; Al-Futaisi and Patzek, 2003; Cui et al., 2022). Its predictive capability has been proven successful as compared to experiments for capillary pressure and relative permeability curves (e.g., Øren and Bakke, 2002). As this approach only deals with just capillary forces under no dynamic flow conditions, it is also computationally efficient (Al-Gharbi and Blunt, 2005; Raouf et al., 2013; Joekar-Niasar and Hassanizadeh, 2012). However, in the case of time-dependent and coupled pore-scale processes such as transient flow, rate effects, and viscous fingering this method is unable to predict dynamic behaviors (Thompson, 2002).

2.3.1.1. Percolation-based quasi-static models. Percolation theory is based on statistical theories that account for randomness in porous medium geometry, structural, transport properties, and their interplay (Berkowitz and Ewing, 1998). In geology and physics, this theory deals with the slow fluid flow in porous media and the connectivity in random systems respectively (Liu and Regenauer-Lieb, 2021). The properties of macroscopic systems known as percolation properties are essentially evaluated based on the onset of macroscopic connectivity within the system (Berkowitz and Ewing, 1998; Hunt et al., 2014). Critical phenomena such as transport in random medium (i.e., many imbibition and drainage processes) can be described by percolation theory. In a random medium (e.g., pore networks), the transport processes depend on a critical point where a property encounters an abrupt change. In porous media and pore-scale models, such as pore networks above a critical saturation, the corresponding phase or its cluster spans the system. For gas-condensate flow, the critical condensate saturation can be an example of such critical properties. The condensation process can be modeled stepwise corresponding to each step of pressure depletion. At each step of condensation, a percolation threshold radius can be defined to determine the number of throats, in which the effective radius of interfacial curvature is equal to or less than the threshold radius. Those throats are then occupied with the condensate phase. This occupation depends on the size distribution of the throats (i.e., for the reason that

interface geometry would be influenced by the throat size).

The capillary-dominated flow regimes (i.e., slow processes where viscous forces are not dominant) in pore-network models can be described by percolation theory referred to as the invasion percolation. In invasion percolation, the movement of phase interfaces in the network is described stepwise, following the flow paths with minimum capillary resistance (Tranter et al., 2020). Thus, this process can be categorized as quasi-static when the capillary (i.e., the entry capillary pressure) is the only criterion governing each individual pore or throat filling. For example, the invasion-percolation algorithm has been applied to study the drying of porous media using pore-network models (Prat, 2011; Biswas et al., 2018). The following two studies address obtaining the gas-condensate macroscopic properties (relative permeability and critical condensate saturation) based on percolation theory.

The initial implementation of the condensation process was mainly based on the physical rules in horizontal and vertical capillaries observed in visual experimental studies of the condensation process, such as those performed in micromodels (Danesh et al., 1987, 1989). Mohammadi et al. (1990) conducted the first PNM study of gas-condensate relative permeability using percolation theory. The physical process of condensation in micromodel laboratory tests indicated that when the pressure is decreased, the condensate phase first fills in the smaller pores, and larger pores remain occupied by only the gas phase. As long as the pressure decline continues, the condensate phase tends to occupy the tight corners of other larger pores and create an interface attached to the pore walls. This process was utilized in the network model by defining a threshold radius to fill larger pores with the condensate phase when the effective pore radius is equal to this threshold radius. The threshold radius value is varied as the gas phase pressure level in the network changes to describe the evolution of the condensate formation in different pores. In other words, as the network pressure is lowered stepwise, larger pores are blocked with the condensate phase. At the pressure level that evaporation starts, the condensate phase in the pores connected to the spanning gas cluster, which could be accessed from the external boundary, is allowed to vaporize.

The network model of Wang and Mohanty (1999) also incorporated

the physical processes observed in micromodels to study the critical condensate saturation at the pore scale. They considered only the condensation process near the critical point where IFT values between gas and condensate are minimal. Under dominated capillary and gravity force effects, disregarding the viscous force effect, the condensation process was described by the concept of percolation theory. The same procedure of the condensation process was applied by Mohammadi et al. (1990) and Fang et al. (1996). Following their algorithm, the criterion for forming a condensate slug in the middle part of a throat was satisfied when the throat radius was equal to or smaller than a pre-specified threshold radius for the condensate meniscus residing in the corner of each throat. Phase change implementation for the above models was based on a schematic diagram of the phase envelope for the liquid dropout phenomenon that occurs during pressure depletion (experimental diagram of condensate dropout versus pressure). During the condensation process, by increasing the number of throats whose radius is lower than the threshold gas-condensate meniscus radius, the coalescence of slugs and the condensates in the corners begins, which creates ganglions in the pore network. Force balance was applied along the horizontal and vertical throats containing the slugs with two curvatures at each end in a converging-diverging profile of the throat to specify the stability of the slugs. This concept was applied to find the critical condensate saturation by balancing the gravitational and capillary forces across the condensate slugs. The critical condensate saturation was defined as a critical length of this ganglion beyond which there is no hydrodynamical stability. The condensate phase was assumed to spread on the water phase (i.e., connate water) and the contact angle hysteresis was also overlooked.

2.3.1.2. Capillary equilibrium-based quasi-static models. Fang et al. (1996) simulated the condensation process using a quasi-static scheme (i.e., where equilibrium states of flow were considered and filling of capillaries was determined based on the stability of menisci for a given contact angle and throat shape) to obtain critical condensate saturation (S_{cc}). The retrograde condensation process was modeled in discrete steps by adding a specified amount of condensate at each stage. In other words, the phase change was indirectly introduced by means of empirical relations obtained from the experiments performed in a PVT cell at different temperatures and pressures. The throats with a radius smaller than a threshold value, set as $20 \mu\text{m}$, were allowed to form condensate bridges and gradually filled. Continuing this process led to allowing larger throats to have condensates as bridges. Finally, S_{cc} was determined at which a continuous path of the condensate phase was developed, providing enough connectivity among different condensate clusters so that the condensate could exit the network. They further emphasized that for gas-condensate fluids, near the critical point where the IFT is low, the condensate spreads over the grain surfaces, and a thin film flow can be established resulting in a very low S_{cc} . However, in the conventional gas-condensate reservoir, this behavior may not often occur because the capillary effect causes the condensate to form bridges between the pore walls as the reservoir temperature is commonly far from the critical point. They assumed constant interfacial tension (i.e., neglected the pressure dependency of IFT), and viscous forces due to gas flow were also disregarded. Therefore, the force balance for a cluster of vertically coalesced liquid bridges was employed, and the liquid pressure was considered to be in hydrostatic equilibrium in the vertical direction.

Pore level physics in Bustos and Toledo (2003a,b) model was based on the condensate saturation evolution in the network under the quasi-static assumption because the condensate meniscus displacement is governed by local capillary pressures and filling of pore elements is determined by stability criterion of condensate bridges for a given contact angle. The condensation and phase change in the system were implemented following the same procedure as Fang et al. (1996) (i.e., using an empirically obtained relationship from experiments). The

condensation was gradually increased in the network in its vertical and horizontal pore elements based on the local capillary pressure. The continuous capillary-dominant flow of gas and condensate was assumed along the gravitational direction ignoring the viscous effect. Defining the snap-off pressure (P_s) for each pore element, the condensate wedges were allowed to reside in the pore corners if their local capillary pressure was exceeding the snap-off pressure. Otherwise, a condensate bridge could form, or the existing condensate bridges could be enlarged. As a result of the blockage of gas paths by the growing number (or size) of condensate bridges and neglecting the viscous effect, the effective gas permeability decreased to zero. In vertical pores, the condensate bridge formation was set at the snap-off pressure, and the movement of the bridge was modeled with the balance of gravity and capillary forces adopted from Fang et al. (1996). However, in the vertical direction, the balance of gravity and viscous force could initiate a downward movement of the bridge, and therefore a cyclical opening and closing process would happen. Mainly, three nearly simultaneous events were accounted for in the condensation process as follows. 1) condensation as a wedge and then as a bridge in the vertical pore and subsequent flow of a bridge (at its critical height) to the surrounding pore elements followed by gas entrance to the pore element if the pore element is connected to the gas flow path, 2) if the gas flow path was established through the reconnection of gas islands, the gas island conductance contributes to the network gas flow permeability, and 3) during the movement of condensate bridges by the connected gas flow, the gas above and below the condensate volume contribute to the network gas flow permeability.

The main governing equation was a conservation law for the gas and condensate flow in the pore elements based on Poiseuille law. The system of equations was written in the matrix form as $AX = B$, representing A as the matrix of conductance values, X as the vector of unknowns for phase pressures, and B as a vector related to the boundary pore pressures and conductance values. With an arbitrary pressure gradient across the network, the system of equations was solved by an iterative method after a search algorithm was implemented to identify the sample-spanning clusters (i.e., the connected pore clusters which act as the flow-carrying backbone). The solution gave the pressure field to determine the flow rates in the pore-throat elements and, thus, in the whole network. Finally, the relative permeability of each phase was calculated using the Darcy law. The continuous condensation process was implemented in several steps, summarized in the flowchart of Fig. 2.

2.3.2. Dynamic two-phase gas-condensate pore-network models

As stated in the approach of quasi-static models, its main drawback is the representation of coupled processes and time-dependent transport phenomena in the porous media. This has led to the development of more advanced mathematical formulations to address those issues in the pore-network models and simulate transient fluid flow within the network (Joekar-Niasar and Hassanizadeh, 2012; Qin and van Brummelen, 2019). The dynamic pore-network models can simulate several relevant physics in light of experimental limitations to provide a numerical predictive tool for continuum scale parameters (Thompson, 2002; Huang et al., 2016; Reis and Carvalho, 2020). This approach is also applicable for studying transient flow, inertial, rate effects, dynamics of contact angle, and the invasion front. However, compared to the quasi-static approach, due to higher nonlinearity of the equations describing the dynamics of coupled processes at the pore scale, these models require robust numerical approaches to tackle pore-scale flow simulation problems (Koplik and Lasseter, 1985; Al-Gharbi and Blunt, 2005; Joekar-Niasar and Hassanizadeh, 2012). In the following section, the development of dynamic pore-network modeling primarily addressing gas-condensate flow as an incompressible immiscible two-phase flow is presented.

2.3.2.1. Dynamic gas-condensate pore-network models: literature summary. Several gas-condensate pore-network models were

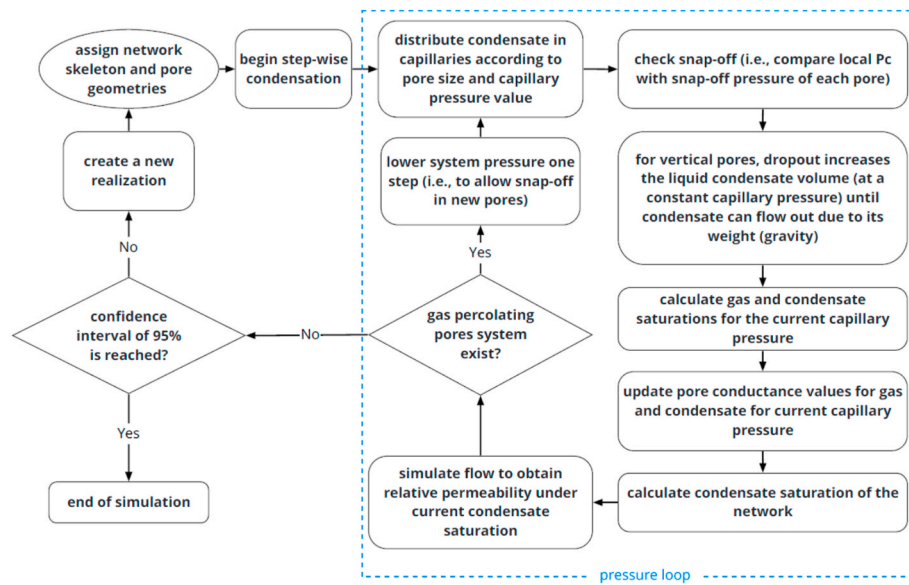


Fig. 2. The flowchart of condensate formation for quasi-static method (Bustos and Toledo, 2003a,b).

considered two-phase dynamic given that the pressure field and saturation distributions are evolved in the network by considering the viscous and capillary forces, and fluid displacements with phase pressures are determined from the solution of developed viscous flow in the capillaries considering the local capillary pressure drops for a given phase distributions. Li and Firoozabadi (2000) studied the critical condensate saturation and relative permeability of the gas-condensate flow in a 2D pore network of circular capillary pores using dynamic PNM. They considered the value of threshold gas–condensate meniscus radius, R_p , constant, and equal to $20\ \mu\text{m}$. Throats with the radius smaller than this threshold were first filled with condensate (the gas phase in those throats with radius less than this threshold were allowed to condense). Hagen-Poiseuille's law was used to represent the conductive flow under the effect of viscous force for the gas-condensate piston-like displacement. They applied a force balance between capillary and viscous force in capillary tubes, while gravity force was also included in vertical tubes. The applied governing equations are presented in Tables 6 and 10. Based on such balance equations, the movement of the slug was simulated. The condensation process in the network was simulated in discrete steps similar to Fang et al. (1996) (i.e., phase change was phenomenologically applied based on the phase behavior of gas-condensate fluid at a specific temperature and pressure, obtained experimentally). However, they additionally included viscous effects. Next, improving the model of Fang et al. (1996), a pressure difference along the network was applied. The pressure distribution was obtained from the solution of a set of linear equations to determine the critical condensate saturation based on the criterion for movement of condensate bridges for each capillary tube and, thus, for the whole network. The effective phase conductance values as a function of their corresponding single-phase conductance and the relative permeability of each phase were calculated when a two-phase flow in the network was established (i.e., when the condensate saturation was above its critical state). Network relative permeability for each phase was calculated from the ratio of phase effective conductance to the absolute single-phase conductance along the network using a renormalization method (an upscaling procedure) following the procedure of Stinchcombe and Watson (1976) for calculating conductivity in heterogeneous media. In this method, the effective phase conductivity is determined on small unit cells (i.e., renormalization cells) of the network and then on larger scales, which ultimately provides the effective phase conductivity for the whole network by the repetition of the renormalization procedure.

Wang and Mohanty (2000) studied pore-scale gas-condensate flow

mechanisms to obtain relative permeabilities and investigate the non-Darcy conductance terms under high-pressure gradients typical in the near-wellbore region using a 3D regular cubic lattice. The phase change below the dew point pressure was considered based on the experimental diagram of liquid dropout versus pressure. Similar to their previous study in 1999, the depletion process of gas condensation was expressed in terms of gas-condensate meniscus radius, determined as a function of fluid phase behavior (i.e., pressure dependency of condensate dropout). The condensate slug in the middle part of a throat could be formed, provided that the throat radius was below a threshold gas-condensate meniscus radius of curvature. Following Li and Firoozabadi (2000), the model of Wang and Mohanty (2000) used the balance between the resultant gravitational force and viscous forces applied on the menisci of a slug at its two sides and the capillary force difference (resulting from the curvature difference at each end of it) to determine the possibility of movement. When the capillary force is not dominant, the condensate slug would flow in a vertical tube. Contact angle hysteresis was disregarded in their selected geometry, and two flow regimes were implemented and evaluated in their model.

The first flow regime was based on a capillary-dominated flow (i.e., low capillary number flow regime), in which each phase flows under its own pressure gradient. The condensate phase flow was, however, conditioned to its saturation exceeding the critical condensate saturation. The fluid distribution in the pore network was controlled by the pores' geometrical and morphological properties as well as phase saturations. In the applied methodology, each phase conductance was calculated first. Then by applying a small pressure gradient along a sample-spanning cluster of each phase (i.e., the continuous fluid cluster, which is connected to both inlet and outlet), the mass conservation law was implemented and solved at each pore body based on the volumetric flow of each phase. Finally, when the pressure distribution in the given network was found, the phase flow rates and total lattice flow rate were obtained, based on which the phase relative permeabilities were calculated.

The second flow regime was considered based on a viscous-dominated flow, including the inertial effect assuming a low condensate-saturated flow. In this simulation scenario, an initial fluid distribution in the lattice was assumed and exposed to high-pressure gradients. Like high gas velocities near the wellbore region, the inertial flow in the defined converging-diverging geometry was computed, and the gas pressure field was calculated at the specified high-pressure gradient. Next, applying a slight pressure gradient along this

redistributed fluid pattern, the pressure calculation was done following a similar procedure described earlier for the first flow regime. Analysis of effective gas flow rates at Darcy-state and inertial-state conditions gives gas effective permeability and the degree of non-Darcy flow (expressed in terms of the effective non-Darcy coefficient using the Forchheimer equation). The ratio of effective gas permeability and effective non-Darcy flow coefficient to the related single-phase values provided the gas relative permeability and the relative non-Darcy coefficient. In this model, two types of droplet formation and flow, based on the micromodel experiments, were considered, one for when the gas flow velocity surpasses a critical velocity in the throats in which condensate droplets are moving under viscous drag force (such throats are not occupied by condensate slug) and another type of the gas flow occurs in the throats that contain condensate slugs and gas pressure gradient exceeds the entry capillary pressure defined as $2\sigma/R_t$ where σ specifies interfacial tension and R_t denotes throat radius.

Jamiolahmady et al. (2000) studied the mechanisms involved in the condensation process and influential factors on the gas-condensate flow based on the available experimental data before PNM modeling. Their study highlighted the pronounced effect of flow rate compared to IFT on the relative permeability in a developed mechanistic model. Furthermore, as the gas-condensate flow near the wellbore regions is substantially influenced by the interaction of viscous, capillary, and inertial forces under very high gas velocities, such interaction was the focus of their study in 2000, and later using PNM in 2003. They studied the thin film flow on the grain surface and condensate lens formation in a model with one conical-shaped pore unit. They obtained the equation of motion for the liquid phase (i.e., the evolution equation) by solving the Navier–Stokes equation. The phase change dependent properties such as IFT and condensate to gas volume ratio (CGR) were considered in their flow analysis. They investigated the evolution of condensate film flow with the simultaneous flow of gas and condensate through a unit conical pore. The main assumptions made in their model included i) no fluid flow through the boundary between gas and condensate (i.e., there was no mass exchange between the two phases at the interface), ii) overlooking gravitational effect, iii) no slip at the capillary wall, iv) continuity of velocity and continuous shear stress at the gas-condensate interface, and v) complete wettability of the wetting phase. Their model determined the spatial fluid distribution at any time in a pore unit. Equations were solved numerically for two open and closed half-cycles separately. Next, as soon as a steady-state condition was attained at a constant condensate-to-gas volume ratio (CGR), specified in the pore inlet, the relative permeability was calculated. The injection rate was gradually increased to evaluate the rate effect while keeping the volume ratio of the two phases entering the pore constant. The main aim of the study was to derive a physically-based model of the thin film flow on the pore surfaces and condensate lens formation in constricted capillaries to examine the impact of IFT and flow rate on the gas-condensate flow at the pore-scale based on observations from micromodels.

To improve the implementation of the rate and multi-pore interaction effects, Jamiolahmady et al. (2003) extended their model to a full pore network description of the porous medium. In a 3D pore network representing a Berea sandstone sample, they implemented dynamic gas-condensate flow at the pore scale. The initial state of the model was defined by an initially distributed condensate thickness at the beginning of simulations (i.e., correlated with pore geometry, capillary number and CGR).

The phase behavior effect was not explicitly applied in their dynamic two-phase pore-network model but the phase change dependent properties were considered based on experimental data at three different pressure levels below the dew point pressure at a certain temperature. Furthermore, an empirical formulation was used in which the initial condensate saturation in each throat was obtained based on the gas-condensate volume ratio (CGR), inlet and outlet radii of each throat, throat length, the condensate viscosity, throat inlet total velocity (i.e., summation of gas and condensate velocity). Then condensate lens

formation was included using a time evolution equation (i.e., to simplify and replace the complex differential equation they had obtained from their previous mechanistic model for closing a pore element). The correlation provided the time interval required for the evolution of the condensate from a thin film into a bridge form. The evolution time was dependent on the pore shape, fluid characteristics, and the initial thickness of the condensate film. According to the cycling process of condensate lens formation and removal in constricted capillaries, as observed in the micromodel experiments, a criterion for opening the closed pores was set based on the entry pressure of the throat containing the condensate suppressing which the condensate could flow. The flow of the condensate bridges and the simultaneous flow of condensate thin film and gas flow were included. The phase pressure field was calculated by solving two sets of linear pressure equations for each time step. By setting the capillary pressure, P_c , equal to zero at the outlet, the simulation was continued until capillary pressure at the inlet approached that of the outlet value (i.e., zero), showing arrival at a stable steady-state condition. The rate effect was studied by incrementally increasing gas and condensate injection rates. The final fluid configurations and conditions at any velocity level were set as the initial model states for the next velocity level. Finally, Darcy's law was applied to determine the relative permeability of each flowing phase at the ultimate steady-state condition.

Similar to Jamiolahmady et al. (2003) network model, Momeni et al. (2017) applied the same methodology for the condensate formation and flow, considering both the condensate corner flow for square-shaped throats and the condensate bulk flow when the viscous forces overcome the capillary force in the throats. They developed a dynamic semi-compositional two-phase flow model in which the phase change was taken into account by flash calculations (i.e., state equations based on phase equilibrium) at each time step decoupled from the two-phase dynamic model to better quantify the condensate phase amount and phase properties in the flow model. They applied the conservation law for the mass flow rates entering and exiting pore bodies. They solved the system of equations to obtain the pressure field at pore bodies for each phase while considering no accumulation terms in the pore bodies. The time step was set according to the time required for the smallest capillary tube to be filled with condensate and snap-off (i.e., using the residence time). The criterion for the condensate snap-off was met when the capillary pressure was less than snap-off pressure, $P_c < P_s$; in this condition, the condensate phase swells from the throat corner towards the center and disconnects the contact line of the gas phase with the throat wall (i.e., condensate blockage occurs). The boundary conditions were set such that a constant CGR was specified in the inlet face of the network, and the pressure was fixed at the outlet face while the other sides had a periodic boundary condition.

Given the peculiarities of gas condensate in shale reservoirs, a specific PNM methodology to study the pore-scale aspects, such as Knudsen flow, has been developed by Labeled et al. (2018). Knudsen flow is a characteristic behavior for shale gas reservoirs where the gas flow does not follow Darcy's law. This pore-scale related displacement depends on the multiphase aspect of flow, which should be further explained in shale gas-condensate reservoirs where gas flow is highly influenced by condensate dropout and accumulation. As the capillary force in the shale matrix is significant, the modification of phase behavior has been the subject of several studies which indicated that the condensation takes place at higher dew point pressures and the condensate saturation is higher compared to the conventional gas-condensate reservoirs. The methodology that was employed by Labeled et al. (2018) was a dynamic gas PNM, including the capillary effect in nanotubes. The gas flow through nanotubes was described by the modified Hagen-Poiseuille equation. After network generation and setting the Knudsen flow parameters, gas and condensate saturations were updated based on pressure steps using PVT data, and finally the pressure field for gas accessible flow network was obtained by solving a set of mass conservation equations (see Tables 6 and 10). The condensation process induced by

phase change behavior for a selected condensate fluid composition was considered at each pressure step of simulation by utilizing the PVT data from the experimental diagram versus pressure. The capillary condensation in the network was such that all pores with a radius smaller than a threshold radius, $R_{g,min}$ (determined from the condensate distribution in the system), were considered to be blocked by the condensate. The simulation of capillary-dominated gas-condensate flow was done in such a way that the gas phase was unable to move the condensate phase, which implied the entrapment of the condensate phase by capillary force and consequently, all nano-throats saturated with condensate set to be blocked. Three flow regimes of Darcy flow, Knudsen flow, including the blockage due to condensation, and Knudsen flow of dry gas without condensate blockage were compared.

2.3.2.2. Dynamic pore-network models: computational methodology. The general form of governing equations in the pore-network modeling is derived based on the mass balance equations written in the location of each pore body referred to as a node. In a two-phase flow system in PNM, the main variables to be solved are often pressure and phase saturations. In the compositional approach, however, the component molar mass conservation is written for each pore body (i.e., node) of the pore network and variables include phase pressures and phase equilibrium properties as well as phase saturations. The void representation of PNM can be considered as a bond model (volumeless pore bodies), site and bond model and site model (volumeless pore throats) depending on the applied pressure formulations. To simulate incompressible immiscible two-phase flow in the dynamic pore-network model, two formulations have been introduced in the literature. One approach is the single-pressure formulation, which is expressed in terms of only one pressure variable for a single-phase, or two-phase fluids considered as an equivalent phase (Koplik and Lasseter, 1985; Singh and Mohanty, 2003; Li et al., 2017). The second approach is the two-pressure formulation, which considers each phase with its own pressure variable (Thompson, 2002; Joekar-Niasar et al., 2010a; Joekar-Niasar and Hassanizadeh, 2011, 2012; Qin, 2015). The general formulations of single and two-pressure algorithms are presented in Table 8. As two-pressure formulations describe dynamic aspects of multiphase flow more accurately, they have commonly been used in different studies such as multiphase flow in porous media, water liquid/vapor flow in fuel cells, and droplet dynamics during the printing process. In the two-pressure formulation, for each of the two fluids occupying a pore body as bulk and wetting film/corner phase, a flow equation (connecting the pressure difference of the phases and its induced flow) is coupled with the corresponding phase mass balance equation. The aforementioned pressure algorithms take into account the (dynamic) transient behavior of flow and reflect the competition of viscous and capillary forces. The first dynamic PNM was introduced by Koplik and Lasseter (1985) for the imbibition process in rocks and then other models were developed for various applications such as drainage and imbibition processes in different porous media (Aker et al., 1998; Mogensen and Stenby, 1998; Hughes and Blunt, 2000; Thompson, 2002; Al-Gharbi and Blunt, 2005; Nguyen et al., 2006; Joekar-Niasar and Hassanizadeh, 2011; Qin and van Brummelen, 2019). Due to simplifications involved in the single-pressure formulation (i.e., assuming negligible local capillary pressure for pore bodies), it has a lower computational cost than the two-pressure formulation. However, some physical processes such as the two-phase countercurrent flow in pores with angular cross sections cannot be described (Joekar-Niasar and Hassanizadeh, 2012; An et al., 2020). Additionally, the single pressure algorithm cannot delineate the dynamics of fluid interface displacements in the pore bodies, particularly for small capillary number values, which in turn leads to inconsistent fluids' occupations within the pore network (Qin, 2015).

Three main solution techniques have been introduced in the literature to solve the governing equations in two-phase dynamic PNM to determine the pressure field and saturation distributions: IMPES

Table 8

Formulation of developed single and two-pressure algorithms in the literature.

Conservation law and flow terms: two-pressure algorithm (Thompson, 2002)

Based on two-phase occupation in a pore body with their own pressure, a local capillary pressure is assigned in a pore body.

$$V_i \frac{ds_i^\alpha}{dt} + \sum_{j=1}^{n_{\text{opp}}} Q_{ij}^\alpha = 0, \alpha = w, nw, \dots (8.1)$$

Total volume balance equation for each pore body i : $\sum_{j=1}^{n_{\text{opp}}} (Q_{ij}^{nw} + Q_{ij}^w) = 0, \dots (8.2)$

$Q_{ij}^\alpha = g_{ij}^\alpha (P_i^\alpha - P_j^\alpha), \alpha = w, nw, \dots (8.3)$ g_{ij}^α is hydraulic conductivity for phase α in the pore throat as a function of the entry capillary pressure of pore throat.

$$g_{ij}^\alpha = f(P_{ij}^c), \dots (8.4)$$

The local capillary pressure in each pore is defined as a function of wetting saturation:

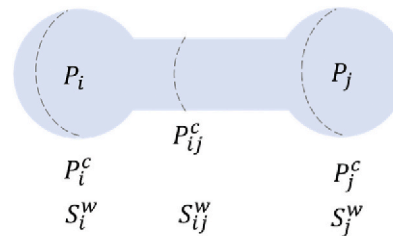
$$P_i^{nw} - P_i^w = P_i^c = f(s_i^w), \dots (8.5)$$

$$s_i^{nw} + s_i^w = 1, \dots (8.6)$$

IMPES algorithm for the two-pressure formulation:

The pressure field, which is obtained from the total volume balance is implicitly solved while updating the saturation phases (phase volume balance equation) explicitly at each time step.

Conservation law and flow terms: single pressure algorithm (Joekar-Niasar and Hassanizadeh, 2012):



Based on a single or two-phase occupation in the pore body/throats and interface location, an equivalent fluid is defined with an equivalent single pressure assigned to each pore body and an equivalent conductivity assigned to each pore throat.

$$V_i \frac{ds_i^{nw}}{dt} + \sum_{j=1}^{n_{\text{opp}}} Q_{ij} S_{ij}^{nw} = 0, \dots (8.7) \text{ or } \sum_{j=1}^{n_{\text{opp}}} Q_{ij} = 0, \dots (8.8)$$

$Q_{ij} = g_{ij} \Delta_{ij}, \dots (8.9)$ where Q_{ij} is the volumetric flow rate in pore throat, ij , V_i is the volume of pore body, i , g_{ij} is the equivalent hydraulic conductance as a function of the pore throat radius (R_{ij}), pore throat length and fluid viscosities.

$$s_i^{nw} + s_i^w = 1, \dots (8.10)$$

$$s_{ij}^{nw} + s_{ij}^w = 1, \dots (8.11)$$

The equivalent pressure drop along the pore throat, ij is defined as:

$$\Delta_{ij} = f(P_i, P_j, P_{ij}^c, \text{pore and throat fluids configuration}), \dots (8.12)$$

In every pore body, only the nonwetting or wetting phase pressure can be defined and superscript n and w does not mean that both pressures have been defined at the same time in a pore. The equivalent pressure drop along the pore throat, ij can be expressed as follows:

$$\Delta_{ij} = P_i^{nw} - P_j^{nw} + S_i^w (P_{ij}^c - P_i^c) - S_j^w (P_{ij}^c - P_j^c), \dots (8.13)$$

$$P_{ij}^c = f(R_{ij}), \dots (8.14) \text{ where } P_{ij}^c \text{ is the entry capillary pressure of pore throat.}$$

(implicit pressure explicit saturation: Thompson, 2002; Qin et al., 2022), IMP-SIMS (implicit pressure semi-implicit saturation: Joekar-Niasar and Hassanizadeh, 2012), FI (fully implicit) (Chen et al., 2020). IMPES and IMP-SIMS algorithms have limitations in numerical stability and global mass conservation errors due to very small time stepping to simulate very low capillary number flow patterns (Joekar-Niasar et al., 2010a; Qin, 2015; Qin and van Brummelen, 2019). FI algorithm, instead, has successfully been applied in recent PNM studies with higher accuracy and lower computational cost to study a wider range of flow regimes from very low to high capillary number flow (Chen et al., 2020; An et al., 2020). This method has also been implemented in compositional PNM, which provided the opportunity to implement compressible two-phase multi-component transport in dynamic PNMs (Chen et al., 2020). The fully implicit scheme can also be used to incorporate coupled physical phenomena in the formulations such as advective, diffusive, and even energy transport together with composition/phase change (Weishaupt and Helmig, 2021). The solution techniques for the pore-network modeling of gas condensates including compositional equations are provided in detail in the section titled "Gas-condensate DCPNM: computational methodology".

Table 9
Summary of gas-condensate pore-network modeling: methods and processes.

Method		Quasi-static model: percolation theory		Quasi-static model: local capillary equilibrium				
Applied methodology		Monte Carlo procedure and the analytical method of Stinchcombe (1974) for evaluation of absolute and relative permeabilities		Force balance in capillary tubes	The continuous condensation process in discrete steps	A Monte Carlo simulation of the condensation process in which the conjugate gradient approach (Mogensen et al., 1999) is applied to solve a system of nodal material balance equations for each phase.		
Pore-scale process	Piston-like advance (bridge displacement)	No	No	No	No	Yes		
	Cooperative pore-body filling	No	No	No	No	No		
	Thin film flow	No	No	No	No	No (assumed corner flow)		
	Snap-off (bridge formation)	Yes	Yes	Yes	Yes	Yes		
	Gravity drainage	No	Yes	No	No	Yes		
Initial thin film assumption in the network		Yes	No	No	No	Yes		
Capillary Number (N_c)		Low, (i.e., capillary-dominant flow: $N_c < 10^{-5}$)		Low (capillary-dominant flow)	Low (capillary-dominant flow)	Low (capillary-dominant flow)		
Forces considered in fluid transport		Capillary		Capillary and gravitational	Gravitational and capillary	Gravitational and capillary		
Author		Mohammadi et al.		Wang and Mohanty	Fang et al.	Bustos and Toledo		
Year		1990		1999	1996	2003a,b, 2004		
Method		Two-phase dynamic						
Applied methodology		The renormalization method (Stinchcombe and Watson, 1976) for effective conductance calculation, the Gauss iteration method was applied to solve a set of linear continuity equations and obtain pressure distribution.	The pressure field in the lattice was derived by solving a set of linear conservation equations for each phase-occupied pore body. Assumptions were capillary-dominated flow regime, and viscous and inertial-dominated flow at low condensate saturation.	Formulating flow of the condensate in a pore unit (by deriving the equation of motion for the liquid phase) in a single pore	The evolution of initial condensate films on the surfaces was implemented in pore-network model by their developed correlations, sparse Gaussian elimination approach was applied to solve a set of linear mass conservation equations at each pore body	The flash calculation was applied to estimate the amount of accumulated condensate, bi-conjugate gradient method was used to solve a set of linear mass conservation equations to obtain each phase pressure.	The relative correction factor, ξ_{rel} was defined and an iterative Newton-Raphson method was applied to solve mass conservation equations for gas and condensate phase and obtain pressure distribution.	
Pore-scale process	Piston-like advance (bridge displacement)	Yes	No	No	No	Yes	Yes	
	Cooperative pore-body filling	No	No	No	No	No	No	
	Thin film flow	No	No	Yes	Yes	No (assumed corner flow)	No	
	Snap-off (bridge formation)	Yes	Yes	No	Yes	Yes	Yes	
	Gravity drainage	Yes	Yes	No	No	No	No	
Initial thin film assumption in the network		No	No	Yes	Yes	Yes	No	
Forces considered in fluid transport		Gravitational, viscous and capillary		Viscous and capillary	Viscous and capillary	Viscous and capillary	Viscous and capillary	
Capillary Number (N_c)		Low		Low and very high (inertial effect)	Moderate 1.1×10^{-3} - 1.9×10^{-5}	Moderate 1.1×10^{-3} - 1.9×10^{-5}	Moderate 1.1×10^{-3} - 1.1×10^{-5}	Low
Author		Li and Firoozabadi		Wang and Mohanty	Jamiolahmady et al.	Jamiolahmady et al.	Momeni et al.	Labeled et al.
Year		2000		2000	2000	2003	2017	2018

Method		Dynamic compositional	
Applied methodology	Collins et al. (1992) methodology (an adaptive-implicit compositional simulator for solving non-linear system of equations, see section "Dynamic compositional pore-network models (DCPNM)" of current review for further details)	Collins et al. (1992) methodology, a compositional slug flow with blockage was implemented.	Fully implicit approach for solving non-linear system of equations for two flow processes: 1- immiscible incompressible two-phase flow, 2- two-phase compressible compositional flow.
Pore-scale process	Piston-like advance (bridge displacement) Cooperative pore-body filling Thin film flow Snap-off (bridge formation) Gravity drainage Thin film assumption Compositional flow model	Yes No Yes Yes No Yes Fully-implicit	Yes No Yes Yes No Yes Fully-implicit
Forces considered in fluid transport	Viscous (high capillary number)	Viscous and capillary	Viscous and capillary
Capillary Number (N_c)	high $8.3 \times 10^{-2} < N_c < 2.4 \times 10^{-1}$	Moderate	Moderate
Author	Santos and Carvalho	Reis and Carvalho	Reis and Carvalho
Year	2020	2020	2021, 2022

2.3.3. Dynamic compositional pore-network models (DCPNM)

Measurements of pore scale gas-condensate flow are very challenging under conditions below dew point pressure (Dawe and Grattoni, 2007). To better quantify dynamic aspects of phase change in gas-condensate systems, the pore-scale study of microscale processes affecting condensate banking and associated multicomponent transport should be thoroughly described (Chen et al., 2020). For example, the complex pore size interaction with phase change behavior in natural nano-porous media (e.g., shale matrix) and deviation from the conventional Darcy flow is currently being explored at the pore scale (LABED et al., 2018). This process is mainly due to a shift in the gas-condensate critical properties at the pore space morphology and its confinement (Civan et al., 2012; Allawe et al., 2015; Pan et al., 2019). Thus, the dynamic compositional PNM approach has appealed as a strong tool to describe the physics of phase transitions between gas and condensate as well as the coupled effect of viscous-capillary forces in recent studies (Santos et al., 2020; Chen et al., 2020). Because of the importance of the subject and its complexity, a summary of studies investigating multi-component transport through dynamic pore-network modeling approaches (i.e., the dynamic compositional pore-network modeling, DCPNM) is discussed further hereafter.

2.3.3.1. Gas-condensate DCPNM: literature summary. Compositional PNM was implemented by Santos and Carvalho (2020) for modeling gas-condensate flow in which conservation of molar flow of components in the gas and the liquid phase was applied at each pore body with a specified volume to calculate the main variables at each pore body (e.g., pressure, the number of moles of each component as well as the source term of each component (i.e., injection or production source terms calculated based on inlet or outlet boundary condition of the pore network)). The single-pressure formulation was adopted to solve the pressure field for the mixture (see Table 10). The governing equations for the compositional modeling in the continuum scale were discretized using the finite difference method and implemented in the pore network. In their formulation, the fluid properties were calculated using an equation of state, while viscosity was obtained based on the pressure and composition. The main unknowns were determined by solving the system of non-linear equations using Newton's method. Following Collins et al. (1992) procedure for compositional modeling and assuming a slightly compressible medium, the pore body volume adjusted with the occupied phase volumes at each time step. They also assumed that the liquid phase could flow as a film along the pore wall, and the thermodynamic equilibrium of phases takes place instantly in the pore body. Given the instant thermodynamic equilibration of the phase, the calculation of phase-equilibrium properties, referred to as flash calculations and main flow equations, was performed separately to reduce the computational time. In the equations of Santos and Carvalho (2020), when solving for the primary variables at the current time step, all flash-dependent and primary variables were obtained iteratively using the Newton-Raphson and a fully implicit scheme was employed to increase the accuracy of results (see Table 10, Equations 10.26 and 10.27).

Reis and Carvalho (2020, 2021) also applied the same compositional model as Santos and Carvalho (2020) to simulate gas-condensate flow, and validate their proposed model with reported literature experiments. The flow regime was considered to be laminar, implying a low Reynolds number flow. The flow of a seven-component reservoir solution was simulated for a range of gas velocities relevant to corresponding values of gas-condensate reservoirs. Using a fully implicit approach, the same set of governing equations as those of Santos and Carvalho (2020) was implemented and solved numerically. A new capillary pressure difference term was added in their formulation to account for the capillary forces acting on a condensate bridge inducing a pressure resistance to gas-condensate fluxes through the pore throats. The pressure field was assigned to the control volume consisting of the center pore body and all

half-length capillaries with a converging-diverging profile connected to the center pore body.

In another study, [Chen et al. \(2020\)](#) developed a 3D dynamic compositional PNM for two-phase gas-condensate flow. They used the two-pressure formulation to address unsteady-state flow for immiscible two-phase flow of the gas-condensate. The main governing equations were defined as molar balance equations including the diffusion term, saturation constraint, and capillary pressure formulation as a function of wetting phase saturation in the pore bodies assuming volumeless throats ([Table 10](#)). The local rules such as capillary pressure formulation, entry capillary pressures, snap-off capillary pressure threshold and conductance terms for two-phase flow in the pore throats were described as auxiliary equations (see [Tables 6 and 7](#)). They selected gas pressure, liquid saturation, and liquid, and gas mole fraction of each component as primary variables. Then, they employed a fully implicit approach and applied Newton method to determine flow and phase-equilibrium state variables simultaneously within Newton iterations loop at each time step. In a similar work, [Reis and Carvalho \(2022\)](#), using the same pore network formulations as their study in 2020, simulated gas-condensate flow at steady state conditions and with different inlet boundary conditions indicative of various gas injection scenarios. Their pore scale dynamic compositional model was proved successful in numerical modeling of the phase change and compositional change at the pore scale resulting in relative permeability values reasonably well matching the experimental data.

The methodologies and processes involved in PNM of gas-condensate flow, in terms of pore-scale mechanisms, flow regimes and applied mathematical models are summarized in [Table 9](#). Besides, statistical techniques such as Monte Carlo and mechanistic models are often utilized to facilitate and supplement models. For instance, Monte Carlo has been used to generate and inspect the impact of pore radius distribution on the gas-condensate flow ([Bustos and Toledo, 2003b](#)).

2.3.3.2. Gas-condensate DCPNM: computational methodology. The molar conservation and flow equations for a number of studies are presented in the next section ([Table 10](#)). To solve the set of developed non-linear equations coupled with phase-equilibrium calculations at the pore scale, the Newton method has been implemented using a fully implicit algorithm ([Chen et al., 2020](#)). As the same as continuum scale compositional simulations, the total molar balance equations written at each pore body are the main governing equations. After the definition of complementary equations such as volume consistency equations and capillary pressure-saturation equations, the main primary variables are defined to be solved iteratively via the Newton method. The number of primary variables to be solved at each time step is of importance as it can influence the computational cost and solution approach. For example, [Santos and Carvalho \(2020\)](#) defined the number of moles of each component, the pressure, and the source term of each component at each pore body of the network as primary variables while the phase stability analysis and phase equilibrium calculations were decoupled from the main flow solver. However, [Chen et al. \(2020\)](#) developed a compressible compositional two-phase flow model for gas-condensate flow taking into account phase changes, where they solved simultaneously the primary variables of pressure, saturation, and each component fraction in the liquid and gas phase (P, S, x_i, y_i) using Newton iterations coupled with phase stability analysis at each time step. [Fig. 3](#) shows general computational steps applied in a compositional pore-network modeling approach following the [Chen et al. \(2020\)](#) computational methodology, which employs a fully implicit solution technique.

The flowchart presenting different steps taken in modeling gas-condensate flow is presented in [Fig. 3](#). Regarding the implementation of the numerical technique, first the initial composition (i.e., each phase saturation is defined based on the pressure level and temperature of the fluid system), as well as the boundary condition of the pore-network model (commonly specified flow rate at the inlet face of network and

a fixed pressure at the outlet face of pore network) are defined. Next, the set of nonlinear system of equations is discretized, and written in the form of residual functions. The Newton-Raphson method is applied to solve for the primary unknown variables. In this method, all residual functions are linearized, and all primary variables are calculated and updated following an iterative scheme to finally converge to the solution of primary unknowns at one time step. Defining X as the vector of principle variables, R as the residual functions, k as the iteration number, and n as the time step counter, the linearization approach for each pore body leads to:

$$[J^{n+1}]^k \cdot [\Delta\delta^{n+1}]^{k+1} = [-R^{n+1}]^k$$

where J is the Jacobian matrix containing numerical derivatives of residual functions with respect to primary variables and $\Delta\delta$ is the difference between primary unknowns during each iteration. This formulation can be presented as follows:

$$(X)^{k+1} - (X)^k = [\Delta\delta^{n+1}]^{k+1}$$

$$(X)^{k+1} = (X)^k - (J^{-1}R)^k$$

$$J = \frac{\partial R}{\partial X}$$

When the system of equations converges to the desired solution with an acceptable error, all primary variables of the current iteration are found and updated, and the procedure shifts to the next time step. The convergence here means that the residuals are less than a threshold value. In other words, the solution of the primary variables could be achieved when $R \rightarrow 0$, that is $(X)^{k+1} \rightarrow (X)^{n+1}$. The macroscopic flow terms such as relative permeability values have often been obtained and reported when the steady-state flow condition is established along the pore network ([Santos and Carvalho, 2020](#); [Reis and Carvalho, 2021](#)).

2.4. Development of the governing equations

Based on the reviewed studies, the following procedure and governing equations are commonly applied for condensate formation and flow modeling in pore networks. After defining the phase occupancy and flow conductance based on the geometry and pore-scale rules, the flux terms are calculated using Poiseuille law, and then the phase pressures and saturation updates are performed based on the mass or molar conservation equations applied often at the pore bodies of the network. For a specified boundary condition in the system, pressure calculations and gas and condensate saturation updates are continued until a steady-state flow is achieved for the whole network. Afterward, the target macroscopic property such as relative permeability is determined. The applied governing equations in gas-condensate flow modeling and relative permeability calculations are summarized in [Tables 10 and 11](#).

2.5. Discussion of the reviewed PNM studies: achievements, similarities, differences, challenges and future perspectives

2.5.1. Significance of gas-condensate pore-network modeling

Reviewing the application of PNM for gas-condensate flow shows that one of the most challenging and essential processes is the condensate bridge formation and its displacement by viscous forces (i.e., driven by velocity effects) in a specified pore geometry, for modeling which different formulations have been offered ([Tables 6 and 7](#)). It is often based on the insights from the experimental observations. To simulate the gas-condensate flow, the fluid flow governing equations (including compositional or non-compositional formulations) that describe the depletion process in the pore network are employed ([Table 10](#)). PNM has investigated the impact of pore structure and process-based influential forces on the gas-condensate flow which cannot be studied using macroscale continuum-scale frameworks. However, capturing the

Table 10
Summary of gas-condensate PNM: flow equations development.

Calculation of transport properties: conservation law and convection terms			
Author	Geometry	Conservation law ^a	Flow terms ^b
Li and Firoozabadi (2000)	Circular cross-section capillary	Volume conservation law: $\sum_{j=1}^{n_{cap}} q_{ij} = 0, \dots (10.1)$ where q_{ij} is volumetric flow rate assuming incompressible fluid in capillary, ij .	$q_{ij} = \frac{\pi R_{ij}^4}{8\mu} \left(\frac{\Delta P_{ij}}{L} + \rho g \right), \dots (10.2)$ where ρ is the density, g is the acceleration of gravity, L is the length of capillary tube, μ is the fluid viscosity, R is the radius of tube, and P is the pressure.
Bustos and Toledo (2003a, b)	Square cross-section capillary	Volume conservation law: $\sum_{j=1}^{n_{cap}} q_{ij} = 0, \dots (10.3)$	$q = g\Delta P, \dots (10.5)$ $g_g = \frac{\pi R_{eff}^4}{8\mu_g L}, \dots (10.6)$
Momeni et al. (2017)	Square cross-section capillary	Mass conservation law: $\sum_j m_{ij} = \sum_j \rho_{ij} q_{ij}, \dots (10.4)$ where m_{ij} is mass flow rate in capillary, ij .	$g_i = \frac{V_l R_l^2}{\beta \mu_l L^2}, \dots (10.7)$ $R_l = \frac{\sigma}{P_c}, \dots (10.8)$ where g is conductance, V_l is liquid volume and R_l is liquid radius of curvature in the capillary, ij .
Jamiolahmady et al. (2003)	Conical circular cross-section capillary	Volume conservation law: $\sum_{j=1}^{n_{cap}} q_{ij} = 0, \dots (10.9)$	$Q_b = \frac{\pi R^4}{8\mu L T_b} \Delta P, \dots (10.10)$ $Q_f = \frac{2\pi R h^3}{3\mu L T_f} \Delta P, \dots (10.11)$ where b and f referring to bulk and thin film flow on the pore surface, h referring to condensate thickness, T_b and T_f referring to equivalent length of total bulk and film resistance.
Labeled et al. (2018)	Circular cross-section capillary	Mass conservation law: $\sum_{j=1}^{n_{cap}} q_{ij} = 0 \quad i = 1..N, \dots (10.12)$	$q_{ij} = g_{ij}^c \Delta P_{ij}, \dots (10.13)$ where g refers to each phase conductance.
Joekar-Niasar et al., 2010a	Square cross-section capillary (cubic pore body)	Mass balance equation: $V_i \frac{\partial s_i^c}{\partial t} + \sum_{j=1}^{n_{cap}} g_{ij}^c (P_i^c - P_j^c) = 0, \dots (10.14)$ Summation of each phase flow equation leads to pressure equation: $\sum_{j=1}^{n_{cap}} g_{ij}^{nw} (P_i^w - P_j^w) + \sum_{j=1}^{n_{cap}} g_{ij}^{nw} (P_i^{nw} - P_j^{nw}) = 0, \dots (10.15)$ Saturation equation: $V_i \frac{\partial s_i^{nw}}{\partial t} + \sum_{j=1}^{n_{cap}} \left(\frac{g_{ij}^{nw}}{g_{ij}^{nw} + g_{ij}^w} (q_{ij}^{nw} + q_{ij}^w) + \frac{g_{ij}^{nw} g_{ij}^w}{g_{ij}^{nw} + g_{ij}^w} (P_i^c - P_j^c) \right) = 0, \dots (8.5.3) P_i^c - P_j^c \approx \frac{\partial p_{ij}^c}{\partial s_{ij}^w} (s_i^w - s_j^w), \dots (10.16)$ where α, s, nw, w, c notations are referring to phase, saturation, non-wetting, wetting, capillary respectively. n_{cap} is the number of capillaries connected to a pore body and V_i is the pore body control volume.	$q_{ij}^{nw} = g_{ij}^{nw} (P_i^{nw} - P_j^{nw}), \dots (10.17)$ $q_{ij}^w = g_{ij}^w (P_i^w - P_j^w), \dots (10.18)$ $P_i^{nw} - P_i^w = P_i^c = f(s_i^w), \dots (10.19)$ $s_i^{nw} + s_i^w = 1, \dots (10.20)$ $P_i^c (s_i^w) = \frac{2\sigma^{nw}}{R_i (1 - \exp(-6.83S_i^w))}, \dots (10.21)$ Computational methodology: The system of mass balance equations is solved for average pressure $\bar{P}_i = S_i^w P_i^w + S_i^{nw} P_i^{nw}, \dots (10.22)$ $P_i^w = \bar{P}_i - S_i^{nw} P_i^c, \dots (10.23)$ $P_i^{nw} = \bar{P}_i + S_i^w P_i^c, \dots (10.24)$ The pressure equation: $\sum_{j=1}^{n_{cap}} (g_{ij}^w + g_{ij}^{nw}) (\bar{P}_i - \bar{P}_j) = - \sum_{j=1}^{n_{cap}} [(g_{ij}^{nw} S_i^w - g_{ij}^w (1 - S_i^w)) P_i^c + (g_{ij}^w (1 - S_j^w) - g_{ij}^{nw} S_j^w) P_j^c], \dots (10.25)$ The pressure and saturation equations are solved using IMP-SIMS (implicit pressure semi-implicit saturation) algorithm.
(Santos and Carvalho, 2020; Reis and Carvalho, 2020)	(Circular tubes; converging-diverging capillaries)	Compositional molar conservation law: $\frac{\partial N_i^k}{\partial t} = - \sum_{j=1}^{n_{cap}} C_{ij} n_{ij}^k + s_i^k, \dots (10.26)$ where N_i is the number of moles of each component k in a pore body i and n_{ij}^k is the molar flow rate of component k in the capillary, ij . s_i^k is the source/sink molar rate imposed at the boundary of network. C_{ij} is an entry of the network incidence matrix.	Santos and Carvalho (2020): disregarding condensate bridge formation $\dot{n}_{ij}^k = (y^k \xi_g g_g + x^k \xi_l g_l)_{ij} \sum_{i=1}^{n_b} C_{ij} P_i, \dots (10.27)$ where x^k and y^k are molar fractions of component, k in the liquid and gas phase, ξ_l and ξ_g are molar liquid and gas density, g_l and g_g are the liquid and gas conductance. P is the mixture pressure in the pore body i , and n_b is the number of pore bodies. Reis and Carvalho (2020): considering condensate bridge formation $\dot{n}_{ij}^k = H_{ij} (y^k \xi_g g_g + x^k \xi_l g_l)_{ij} \Delta P_{ij}, \dots (10.28)$ $\Delta P_{ij} = \sum_{i=1}^{n_b} C_{ij} P_i - H_{ij}^{int} \Delta P_{ij}^{int}, \dots (10.29)$ $\Delta P_{ij}^{int} = \left[2\sigma \cos \theta \left(\frac{1}{R_1} - \frac{1}{R_2} \right) \right]_{ij}, \dots (10.30)$ $H_{ij}, H_{ij}^{int} = f(\Delta P_{ij}^{int}, S_{g,crit}), \dots (10.31)$ where H is a step function depending on the gas saturation at snap-off condition (i.e., $S_{g,crit}$) and also interface capillary pressure difference (ΔP_{ij}^{int}) along a condensate bridge in the capillary, ij . $S_{g,crit} = S_g$, at critical condensate film thickness, t_{crit} at snap-off conditions, $\dots (10.32)$ $C_{ij} = \begin{cases} 0, & \text{if the pore throat } j \text{ is not connected to the pore body } i \\ -1, & \text{if the pore throat } j \text{ enters the pore body } i \\ +1, & \text{if the pore throat } j \text{ exists the pore body } i \end{cases}, \dots (10.33)$ Volume consistency equation: $V_i = V_{g_i} + V_{l_i} \approx \bar{V}_i [1 + \nu (P_i - \bar{P})], \dots (10.34)$ where ν is the pore body compressibility factor.

Author	Geometry	Conservation law ^a	Flow terms ^b
Chen et al. (2020) (Immiscible incompressible two-phase flow)	square-tube (tube-shaped with square cross section) and cubic pore bodies	The mass balance equation for each fluid phase in the pore body, i : $V_i \frac{\partial s_i^\alpha}{\partial t} + \sum_{j=1}^{n_{cap}} g_{ij}^\alpha (P_i^\alpha - P_j^\alpha) = 0, \alpha = w, nw, \dots (10.35)$	$Q_{ij}^\alpha = g_{ij}^\alpha (P_i^\alpha - P_j^\alpha), \alpha = w, nw, \dots (10.36)$ $S_i^w + S_i^{nw} = 1, \dots (10.37)$ Assuming phase equilibrium condition in each pore body: $P_i^{nw} - P_i^w = P_i^c, \dots (10.38)$ For square-tube pore body: $P_i^c = \begin{cases} \frac{\sigma}{r_i} & 0 < s_i^w \leq s_{i,c}^w \\ \frac{\sigma \sin(\pi/4 - \theta)}{R_i \sin(\pi/4)} & s_{i,c}^w < s_i^w \leq 1 - \delta, \dots (10.39) \\ \frac{\sigma \sin(\pi/4 - \theta)}{R_i \sin(\pi/4)} [(1 - s_i^w)/\delta]^{1/3} & 1 - \delta < s_i^w \leq 1 \end{cases}$ $R_i \left\{ s_i^w / \left[\frac{\sin(\pi/4 - \theta)}{\sin(\pi/4)} \cos \theta - \left(\frac{\pi}{4} - \theta \right) \right] \right\}^{1/2}, \dots (10.40)$ where R_i is the inscribed radius, r_i is the radius of curvature, δ is a small positive number ($\delta = 0.01$) and a critical wetting saturation is defined as $s_{i,c}^w = 1 - \frac{\pi}{4}$.
Chen et al. (2020) (Compositional two-phase flow formulation with phase change)	square-tube (tube-shaped with square cross section) and cubic pore bodies	The main mass balance equation: $V_i \frac{\partial}{\partial t} (x_i^k \rho_i^k s_i^k + y_i^k \rho_i^g s_i^g) + \sum_{j=1}^{n_i} F_{ij}^{k,adv} + \sum_{j=1}^{n_i} F_{ij}^{k,diff} = 0, \dots (10.41)$	The advection flow term: $F_{ij}^{k,adv} = x_{ij}^k \rho_{ij}^k f(p_i^k, p_j^k) g_{ij}^k (p_i^k - p_j^k) + y_{ij}^k \rho_{ij}^g f(p_i^g, p_j^g) g_{ij}^g (p_i^g - p_j^g), \dots (10.42)$ The diffusion flow term: $F_{ij}^{k,diff} = \frac{D_{ij}^{k,g} A_{ij}^g \rho_i^g \max(y_i^k - y_j^k, 0) + \rho_j^g \min(y_i^k - y_j^k, 0)}{L_{ij}}, \dots (10.43)$ where $D_{ij}^{k,g}$ is the diffusion coefficient of component, k in the gas phase in the pore throat, ij . The liquid and gas conductances are denoted by g_{ij}^k and g_{ij}^g , presented in Table 6. At an equilibrium state, the fugacities of each component in the liquid and gas phase in a pore body, i are equal: $f_i^{k,l} = f_i^{k,g}, \dots (10.44)$ $\sum_{k=1}^{n_c} x_i^k = \sum_{k=1}^{n_c} y_i^k = 1, \dots (10.45)$ $S_i^l + S_i^g = 1, \dots (10.46) f(p_i^l, p_i^g) = \frac{(p_i^l + p_i^g)/2}{\min(p_i^l, p_i^g)}, \dots (10.47)$ where α denotes the corresponding phase.

^a The conservation law is applied at each pore body, i in the pore-network model.

^b The flow in each capillary, ij is calculated based on the phase conductance and the applied pressure gradient.

real porous structure is challenging, and thus network geometry and topology have evolved through the years to accurately capture this effect. The site models representing the converging-diverging pore-throat shape and simple bond models (which neglect pore body volumes) have been implemented in the literature to model the cyclic process of condensation in pore throats (i.e., the snap-off phenomenon induced by swelling of the condensate in the constricted capillaries and its displacement by viscous forces). Given the importance of film/corner flow of condensate on pore walls/in the crevices and corners of throats in real porous media observed in the micromodel experiments (e.g., Danesh et al., 1988, 1989, 1991; Coskuner, 1997; Jamiolahmady et al., 2000), the pore cross-sectional shapes of throats have been improved from circular to the shapes with an angular cross-section (i.e., convex polyhedrons) such as cuboid and tetrahedral shapes in recent years (Table 5). By introducing the angular shapes, pore-network models could capture processes such as snap-off (Piri and Blunt, 2005; Chen et al., 2020) (see Table 6 for details). Apart from the evolution in considered pore geometry and topologies, given the complex physics of gas-condensate flow, the computational algorithms were also developed and evolved from a quasi-static approach to dynamic and dynamic compositional methods. Additionally, in recent studies, solution algorithms have been improved from IMPES (implicit pressure explicit saturation), and IMP-SIMS (implicit pressure semi-implicit saturation) generally applied in immiscible incompressible two-phase flow to fully implicit (FI) approaches. Thus, accurate solutions have been achieved applicable for various coupled processes at the pore scale, including phase change (Chen et al., 2020). Such advancements enabled researchers to better capture the interplay between capillary and viscous forces. The component transport and its contribution to the gas and condensate flow at the micro-scale has also been modeled efficiently with its macroscopic manifestation in the gas-condensate reservoir flow patterns.

2.5.2. The main similarities of the reviewed PNM studies

For pore-space representation, generally, Weibull and log-normal pore size distributions have been utilized. The former has been used for modeling sandstone samples, and the latter has been employed for evaluating the effect of pore geometry, commonly in parametric studies. The applied boundary conditions often included condensate and gas flow for the inlet, and constant pressure for the outlet boundary, to reflect the conditions held in the gas-condensate reservoir region adjacent to wellbores and to provide flow properties under steady-state conditions. In addition, most studies only assign hydraulic conductance to pore throats (capillaries) by assuming infinite conductivity for pore bodies.

Although in compositional formulation, the molar accumulation term has been included in the conservation equation, in most cases, the relative permeability has been reported under the resulting steady-state flow condition. Nonetheless, the first steps for the generalization of gas-condensate flow PNM to the transient condition has been taken by Chen et al. (2020). For most dynamic pore-network models summarized in this study, the condensate bridge primarily forms within the throats. Then, its displacement occurs where the gas pressure gradient along the condensate bridge is higher than a critical pressure drop (please see Table 6) (Reis and Carvalho, 2020, 2021, 2022) or exceeds the pore entry pressure (Jamiolahmady et al., 2003; Momeni et al., 2017) as was shown in Table 6. Besides, Labe et al. (2018) considered a criterion in which gas pressure gradient should overcome the difference of capillary pressures acting on two sides of the bridge to initiate its displacement from one pore throat to another. The differential capillary pressure threshold is determined based on IFT, contact angle, and throat radii. Furthermore, condensate may swell and disconnect the gas flow, if the snap-off criterion is met.

2.5.3. Differences among pore-network models

In the early stages, very often pore-network models were used to

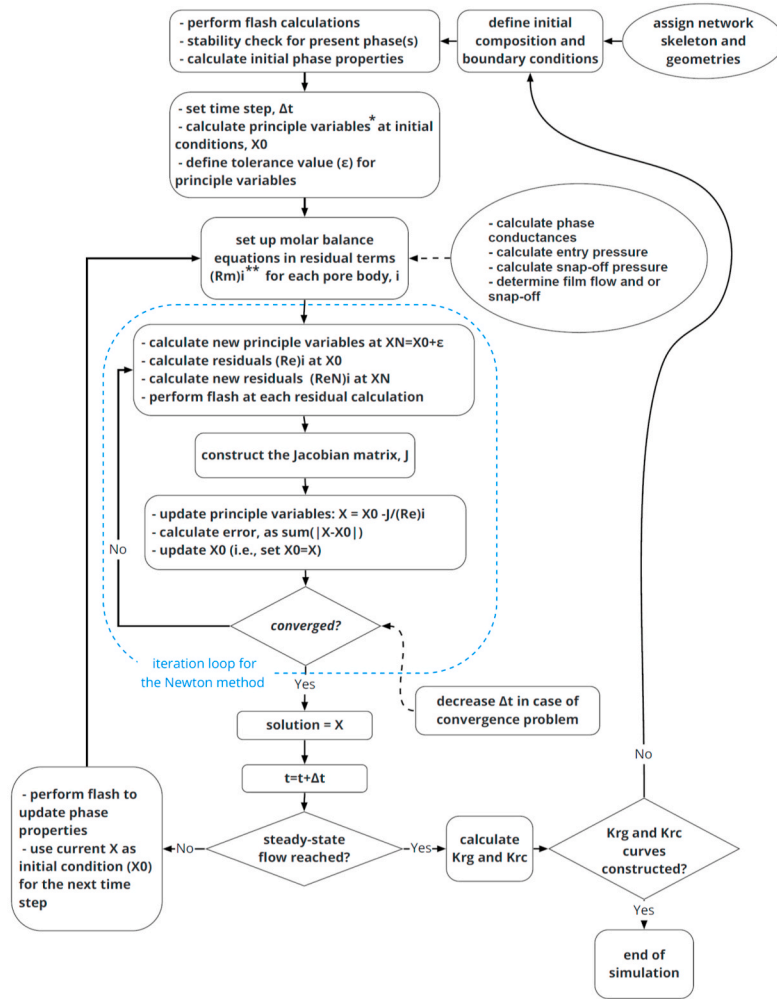


Fig. 3. The flowchart of the computational steps applied in a compositional pore-network modeling approach following the methodology of Chen et al. (2020) to simulate the gas condensation process in porous media.

* Primary variables are considered to be the overall molar composition and gas phase pressure, and the eliminated variables are updated by flash calculations after the primary variables are computed.

** $(R_m)_i$ = [Summation of molar rates at each pore body element, i] + [+inlet/-outlet molar rates at the boundary] - [molar change for each pore body element versus time].

* Primary variables are considered to be the overall molar composition and gas phase pressure, and the eliminated variables are updated by flash calculations after the primary variables are computed.

** $(R_m)_i$ = [Summation of molar rates at each pore body element, i] + [+inlet/-outlet molar rates at the boundary] - [molar change for each pore body element versus time]

Table 11
Relative permeability calculation.

Author	Model	Relative permeability equation
Relative permeability (Bustos and Toledo, 2003a,b)	Quasi-Static Model	$K_{rj} = \frac{G_j}{\bar{G}}$... (11.1)
		$G_j = \frac{Q_j}{(P_{in} - P_{out})}$, ... (11.2)
		$\bar{G} = \frac{Q}{(P_{in} - P_{out})}$, ... (11.3) where G_j is the network phase j conductance and \bar{G} is the single-phase network conductance
Relative permeability (Jamiolahmady et al., 2003)	Dynamic Model	$K_{rj} = \frac{\mu_j Q_j}{AK} \left(\frac{-L}{\Delta P_j} \right)$, $j = l, g, \dots$ (11.4)
		$K_{rj} = \frac{K_j}{K}$... (11.5)
		$K_{rj} = \frac{Q_j}{Q}$... (11.6)

investigate the critical condensate saturation under the quasi-static assumption and viscous forces were not included (Table 2). In quasi-static models, the condensate distribution was updated based on only local capillary pressure. For cases where viscous forces are dominated,

dynamic approach modeling has been employed, in which the gas pressure gradient is considered to mobilize the condensate bridges. Moreover, the geometrical idealization of void space is also different among different studies. On the one hand, there are site-bond models, which have been used to investigate the condensate evolution in the network of pores and throats and inspect the morphology and structural effects on macroscopic parameters such as critical condensate saturation (Wang and Mohanty, 1999, and 2000; Santos and Carvalho, 2020). On the other hand, a number of models take the advantage of the simplicity of bond models to quantify the effects of velocity and interfacial tension on gas-condensate effective permeability (Jamiolahmady et al., 2003; Momeni et al., 2017). Recently, Chen et al. (2020) developed a site model to investigate the phase saturation distribution and the viscosity ratio effect on gas-condensate flow patterns. Sites have to be taken into account to capture the reality of condensate flow, particularly at high condensate saturations, where pores and pore-filling mechanisms with phase change play an indispensable role in pore scale displacements of condensate. In recent PNM studies, pore-scale displacement mechanisms such as snap-off processes have also been incorporated. However, the snap-off criterion is quantified differently at the pore-scale among different pore scale models as presented in Table 6. Finally, a major contrast is whether or not the model accounts for the mixture

composition, which has only recently been included in the modeling formulations (for compositional gas condensate PNM, see Table 2). Compositional pore-network modeling has also been introduced in other applications of PNM to study two-phase flow including the phase change process in the porous media, fuel cells, and printing processes. Contrary to quasi-static and dynamic pore-network models, dynamic compositional pore-network models can better capture complexities of gas-condensate flow, such as compressibility, component transport, and phase change, directly and explicitly. For instance, a study conducted by Chen et al. (2020) quantified the very complex and coupled processes of phase change, capillary, and viscous forces in a gas-condensate flow system and modeled induced viscous fingering. Similarly, Reis and Carvalho (2022) studied the coupled processes of phase and compositional change through gas injection in the pore-network model.

2.5.4. Challenges and the way forward

Despite the modeling opportunities that pore-network modeling offers, its simplification of the real geometry and challenges pertinent to accurately describing pore-filling mechanisms have led researchers to search for innovative and new solutions. Advancements to address such shortcomings include considering conductance and fluxes within pore bodies by introducing extra computational nodes in each corner of drained pore bodies (Raouf et al., 2013) or using coupled techniques such as lattice Boltzmann informed pore-network modeling (Puig Montellà, 2019; Montellà et al., 2020) to refine calculations. Besides, progress in imaging techniques has evolved our understanding of pore-scale physics and has shed light on local rules and pore-scale physics, which have to be implemented in the pore-network models (Schmatz et al., 2015; Dehshibi et al., 2019; Blunt et al., 2019). The pore-scale images not only serve as benchmark data sets to validate pore-scale models by providing a complete characterization of interfacial areas, curvature, and wettability (Joekar-Niasar et al., 2010a; Bultreys et al., 2018) but also let the disclosure of phenomena such as the formation of saddle-shaped menisci spanning the pore space, spatial distribution of contact angles, and evolution of Haines jumps, which are not otherwise possible (Lourenço et al., 2012; Berg et al., 2013; Lin et al., 2019; Spurin et al., 2020; Milatz et al., 2022).

Regarding accurate conceptualization of pore geometry (i.e., the difficulties pertinent to the extraction of the realistic throat and pore shapes) and careful characterization of wettability required for PNM studies, advanced 3D and 2D imaging techniques (such as dynamic x-ray tomography, neutron tomography, focused ion beam scanning electron microscopy, helium ion beam scanning electron microscopy and confocal microscopy), and data assimilation with synchrotron X-ray fluorescence microscopy (SXRF) results offer great opportunities for delineation of pore and throat geometry as well as wettability. Such advancement makes it possible to account for the heterogeneity in the mineralogy of the grains at their surfaces and, consequently, in the pore walls. More accurate pore-network models can be constructed with further insights from imaging pore-scale filling mechanisms, snap-off, corner, and film flow.

The imaging of tailored experiments such as high-pressure high-temperature microfluidics is recommended as a way forward to get insight into the formation of condensate bridges and their coalescence as well as transport. Besides, advanced microfluidics equipped with particle imaging velocimetry and fiber optics can enhance our understanding of pore scale pressure and velocity fields, helping us to refine local rules in dynamic pore-network models (Zarikos et al., 2018a, 2018b). Moreover, in the absence of imaging data from porous media, there are also theoretical models, which can infer pore space information from solid skeleton based on fractal theory (Khoshghalb et al., 2015; Penghui et al., 2019).

Notwithstanding all the recent advances in pore-scale imaging studies, the pore-filling mechanisms and the pore-scale processes during drainage and imbibition displacements are the subjects of ongoing research. Since the effect of pore and throat morphology as well as

wettability on the competition of involved pore-scale mechanisms such as snap-off and cooperative pore body filling are not yet well formulated for complex pore and throat morphologies and pores of high coordination number.

Pore-scale imbibition mechanisms include piston-like movement, snap-off and cooperative pore-body filling, the latter of which is not yet well characterized since its micromodel observations by Lenormand et al. (1983). First steps have been taken by Ruspini et al. (2017) to generalize the stochastic expressions put forward by Blunt and Scher (1995), Blunt (1997), and Øren et al. (1998) to explicitly account for the spatial locations of the connecting throats and the local fluid topology. Nevertheless, their model is limited to the cases where the centerline of the throats meets in the center of the associated pore. Furthermore, the advancement of pore-scale imaging has led to the discovery of new pore-filling mechanisms which need to be formulated and incorporated into pore-network models (Singh et al., 2022). Singh et al. (2022) have also employed fast pore-scale imaging to inspect quantitatively the correlation of different pore-filling events with aspect ratio, pore and throat radius, throat shape factor, as well as coordination number. Dynamic pore-scale imaging has also been employed to look at the snap-off evolution, as well as to validate its direct numerical simulation (Singh et al., 2017; Shams et al., 2021). As a result, pore-scale displacement rules obtained from such studies can provide valuable input for developing more advanced pore-network models.

Although pore-network modeling favors its lower computational demand as compared to direct numerical simulation, dynamic pore-network modeling of a large domain can still be computationally challenging, mainly when pore-scale models of complex porous media such as shales with a broad spectrum of pore scales are aimed at (Song et al., 2020). Artificial intelligence-informed pore-network modeling and GPUs can be considered as possible remedy to expedite dynamic pore-network modeling by reducing its computational demands or via parallelization (An et al., 2020). Assimilation of imaging data of various scales for multi-scale pore-network models is another avenue of research, paving the way to model complex rock structures (Ruspini et al., 2021; Wang et al., 2022).

Apart from challenges pertinent to pore-network modeling of two-phase flow, pore-network models developed for gas-condensate flow have been in their evolution stage. As revealed in the course of this review, few studies capture the full depiction of porous media and assign the volume to both pores and throats. There are therefore rare PNM studies of gas-condensate studies incorporating cooperative filling mechanisms. Further to that, the use of coupled PNM and phase field-based LBM can be considered to better characterize the coalescence of condensate bridges using phase field-based LBM (Younes et al., 2022) and model their displacement through the pore network.

The recent development of the compositional PNM is another advancement offering the possibility to investigate simultaneously the effect of micro-scale phenomena controlling condensate formation and flow along with the phase behavior and composition. Compositional PNM can improve our understanding of fluid and process-dependent mechanisms by implementing thermodynamic behaviors, phase change, compressible fluid flow, and compositional transport of components in gas condensation systems. In a way forward, the compositional-dependent processes involved in EOR methods such as gas recycling, solvent injection, and wettability alteration applied to gas-condensate reservoirs can be studied in the near future using PNM even in complex reservoir rocks like carbonates and shales. Experimental data on condensate formation and swelling, thin film flow in liquid-wet medium, and flow regimes present in altered/mixed wettability reservoirs can provide valuable information and crucial knowledge for not only developing but also verification of dynamic pore-network models of gas-condensate flow. The scarcity of the experimental data required for elucidating pore-scale mechanisms and local rules needed for pore-network modeling has therefore to be addressed along with numerical advancements.

3. Concluding remarks

Early gas-condensate pore-network models have considered limited pore-scale processes and mechanisms to simulate gas condensate behavior. Gravity and capillary forces were first included in circular-shaped horizontal and vertical capillaries. Over time, the angular pores were considered to allow for the corner flow of the wetting phase. The improvement in models was achieved by the introduction of equivalent pore-networks extracted from images of core samples. Viscous, inertial, and Knudsen flow effects in gas-condensate and shale gas-condensate systems have been studied in several models. Governing flow equations in the pore networks were improved from quasi-static condensation processes to volume/mass conservation equations considering viscous forces, and recently to the compositional molar balance formulations to more accurately simulate phase and compositional changes in the pore network. The available core-flood experimental data and micromodel observations have been employed to determine critical condensate saturation, investigate the dependence of gas-condensate relative permeability on the flow velocity, and directly determine wettability and IFT effects on the gas and condensate flow in the recently developed pore-network models. The fundamental study on gas-condensate via PNMs aims to address pore-scale mechanisms altering the gas-condensate well deliverability under near-wellbore conditions as well as multicomponent transport effects on flow patterns.

In summary, there is no single PNM study in the literature which includes all relevant processes. For instance, while the early models suffered from overlooking mixture composition, recently introduced compositional models do not often account for gravitational effects, water saturation, and inertial effects. The formation and distribution of condensate in porous media, swelling of condensate, pore invasion processes such as pore-filling mechanisms, and slug flow in mixed wettability media all require insights from micromodel and experimental data yet to be conducted to accurately set up pore-network formulations. On the other hand, the current models have mostly

considered throats or capillaries and have given less value to pores, although condensate can also form therein. Recent advancements in flow transport mathematical models with robust computational methodologies (e.g., fully implicit approach) have improved implementation of pore scale flow physics. Better characterization of geometry and refining the implemented physics can result in more comprehensive pore-scale models which can be used to study multi-phase and multi-component processes in gas-condensate as well as being utilized in exploring similar issues faced in other various natural and industrial porous material applications.

Declaration of competing interest

The authors declare that they have no known competing financial interests or personal relationships that could have appeared to influence the work reported in this paper.

Data availability

No data was used for the research described in the article.

Acknowledgement

The authors would like thank the constructive comments of two anonymous reviewers as well as Prof. Masa Prodanovic of The University of Texas at Austin for her notes on the comparison of direct numerical methods and pore-network models as well as Dr. Pooyan Broumand of Shiraz University for his comments on the advantages and disadvantages of phase field method. The authors have special thanks to Prof. Holger Steeb from University of Stuttgart for his comments on different approaches in smoothed particle hydrodynamics (SPH). Finally, Dr. Arman Khoshghalb of University of New South Wales is acknowledged for his pointer to fractal models of porous media.

Nomenclature

A	area
CGR	condensate gas ratio
dt	time step
e	condensate film thickness in the capillary
g	fluid conductance
G	shape factor
\bar{G}	average network conductance
h	condensate bridge height
h_{max}	maximum length of a ganglion
H	step function showing the status of opening or closing of a capillary for flow
H^{int}	function indicating whether the ΔP_{int} is included in equation 10.29
IFT	Interfacial Tension
K	permeability
K_{rl}	liquid relative permeability
K_{rg}	gas relative permeability
K_n	Knudsen number
L	capillary length
m	mass
n_{pore}	number of pore bodies
n_{cap}	number of capillaries
n_c	number of corners
\dot{n}	molar flow rate
N	number of moles
N_B	Bond number
N_c	capillary number
P	pressure
P_c	capillary pressure

P_e	entry pressure
\bar{P}	reference pore body pressure for volume calculation
PV	pore volume
ΔP	pressure gradient
ΔP^{int}	pressure difference along the condensate bridge due to capillary effect
ΔP_{crit}	critical pressure needed to mobilize a condensate bridge in a capillary
q	flow rate
R_p	a threshold value defined for the menisci of gas-condensate in pore corners
R_t	inscribed radius of the throat
R	capillary radius
R	average value of the radius
R_1	the minimum radius of curvature for the condensate bridge at a specified saturation
R_2	the maximum radius of curvature for the condensate bridge at a specified saturation
R_{eq}	an equivalent radius defined for each pore geometry
R_{max}	capillary maximum radius in the defined pore geometry with converging-diverging profile
R_{min}	capillary minimum radius in the defined pore geometry with converging-diverging profile
s	the term for sink or source
S	fluid saturation
SD	standard deviation
S_{cc}	critical condensate liquid saturation
t	time
t_{crit}	the condensate thickness at which the condensate film gets snapped-off in a capillary
V	volume
\bar{V}_i	reference volume for volume calculation at pore body, i
v	pore body compressibility factor
x	index for the liquid molar fractions
y	index for the gas molar fractions
z	index for the mixture molar fractions
Z	coordination number
α	corner half angle
β	corner half angle
θ	contact angle
θ_A	advancing contact angle
θ_R	receding contact angle
λ	the average minimum free path
φ	porosity
μ	fluid viscosity
ρ	fluid density
σ	gas-condensate interfacial tension
ξ	density in terms of molar quantity of a substance within the volume
ξ_{rel}	relative gas-condensate correction factor

subscripts

A	advancing
b	bulk
c	critical
c	condensate
cc	referring to critical condensate saturation
$crit$	critical
eff	effective
$entry$	referring to entry pressure
eq	equivalent
f	film
g	index for the gas phase
i	property in pore body i
in	inlet
ij	index for the capillaries
ig	index of gas phase in capillary j
il	index of liquid phase in capillary j
l	index for the condensate liquid phase
nw	index for the non-wetting phase
out	outlet
p	phase
pc	phase corner

<i>r</i>	relative
<i>r_j</i>	relative to property of <i>j</i>
<i>R</i>	receding
<i>S</i>	snap-off
<i>S_{th}</i>	snap-off threshold
<i>t</i>	time
<i>T_b</i>	total bulk
<i>T_f</i>	total film
<i>thr</i>	threshold
<i>w</i>	referring to wetting phase

superscripts

<i>c</i>	capillary
<i>in</i>	inlet
<i>int</i>	referring to interface capillary pressure difference term
<i>k</i>	indicating the <i>k_{th}</i> component in the composition
<i>n</i>	time counter
<i>nw</i>	non-wetting
<i>out</i>	outlet
<i>sf</i>	slug flow
<i>w</i>	wetting
<i>α</i>	phase

References

- Ahmadi, M.A., Chen, Z., 2019. Comparison of machine learning methods for estimating permeability and porosity of oil reservoirs via petro-physical logs. *Petroleum* 5 (3), 271–284.
- Aker, E., Maloy, K.J., Hansen, A., Batrouni, G.G., 1998. A two-dimensional network simulator for two-phase flow in porous media. *Transport Porous Media* 32, 163–186.
- Al-Futaisi, A., Patzek, T.W., 2003. Impact of wettability alteration on two-phase flow characteristics of sandstones: a quasi-static description. *Water Resour. Res.* 39 (2).
- Al-Gharbi, M.S., Blunt, M.J., 2005. Dynamic network modelling of two-phase drainage in porous media. *Phys. Rev. E* 71, 016308.
- Allawe, E.M., Stockdale, A.P., Aminiaa, K., Ameri, S., 2015. Impact of nanoscale pore confinement on estimation of gas resources and gas/condensate behavior in shale reservoirs. In: *SPE Eastern Regional Meeting*. OnePetro.
- Alpak, F., Samardžić, A., Frank, F., 2018. A distributed parallel direct simulator for pore-scale two-phase flow on digital rock images using a finite difference implementation of the phase-field method. *J. Petrol. Sci. Eng.* 166, 806–824.
- An, S., Erfani, H., Godínez-Brizuela, O.E., Niasar, V., 2020. Transition from viscous fingering to capillary fingering: application of GPU-based fully implicit dynamic pore network modeling. *Water Resour. Res.* 56 (12), e2020WR028149.
- An, S., Yu, H.W., Wang, Z., Kapadia, B., Yao, J., 2017. Unified mesoscopic modeling and GPU-accelerated computational method for image-based pore-scale porous media flows. *Int. J. Heat Mass Tran.* 115, 1192–1202.
- Beresnev, I.A., Li, W., Vigil, R.D., 2009. Condition for break-up of non-wetting fluids in sinusoidally constricted capillary channels. *Transport Porous Media* 80 (3), 581.
- Berg, S., Ott, H., Klapp, S.A., Schwing, A., Neiteler, R., Brussee, N., et al., 2013. Real-time 3D imaging of Haines jumps in porous media flow. *Proc. Natl. Acad. Sci. USA* 110 (10), 3755–3759.
- Berkowitz, B., Ewing, R.P., 1998. Percolation theory and network modeling applications in soil physics. *Surv. Geophys.* 19 (1), 23–72.
- Biswas, S., Fantinel, P., Borgman, O., Holtzman, R., Goehring, L., 2018. Drying and percolation in correlated porous media. *Physical Review Fluids* 3 (12), 124307.
- Blunt, M.J., King, P., 1991. Relative permeabilities from two- and three-dimensional pore-scale network modelling. *Transport Porous Media* 6, 407–433.
- Blunt, M.J., Scher, H., 1995. Pore-level modeling of wetting. *Phys. Rev.* 52 (6), 6387.
- Blunt, M.J., 1997. Pore level modeling of the effects of wettability. *SPE* 38435. *SPE J.* 2.
- Blunt, M.J., Lin, Q., Akai, T., Bijeljic, B., 2019. A thermodynamically consistent characterization of wettability in porous media using high-resolution imaging. *J. Colloid Interface Sci.* 552, 59–65.
- Blunt, M., Jackson, M.D., Piri, M., Valvatne, P.H., 2002. Detailed physics, predictive capabilities and macroscopic consequences for pore-network models of multiphase flow. *Adv. Water Resour.* 25, 1069–1089.
- Bultreys, T., Lin, Q., Gao, Y., Raeini, A.Q., AlRatrou, A., Bijeljic, B., Blunt, M.J., 2018. Validation of model predictions of pore-scale fluid distributions during two-phase flow. *Phys. Rev.* 97 (5), 053104.
- Bustos, C.I., Toledo, P.G., 2003a. Contact angle hysteresis effects on the relative permeability of gas and condensate in three-dimensional pore networks. *Lat. Am. Appl. Res.* 33 (1), 45–50.
- Bustos, C.I., Toledo, P.G., 2004. Pore shape effects on the relative permeability of gas and condensate in three-dimensional pore networks. *Transport Porous Media* 55 (2), 247–251.
- Bustos, C.I., Toledo, P.G., 2003b. Pore-level modeling of gas and condensate flow in two- and three-dimensional pore networks: pore size distribution effects on the relative permeability of gas and condensate. *Transport Porous Media* 53 (3), 281–315.
- Cai, J.C., Chen, Y., Qiao, J.C., Yang, L., Zeng, J.H., Sun, C.H., 2022. Determination of dynamic capillary effect on two-phase flow in porous media: a perspective from various methods. *Petrol. Sci.* 19 (4), 1641–1652.
- Chalabaud, C., Robin, M., Bekri, S., Egermann, P., 2007. Wettability impact on CO₂ storage in aquifers. Visualisation and quantification using micromodel tests, pore network model and reservoir simulations. In: *Proceedings of the International Symposium of the Society of Core Analysts*, pp. 10–12.
- Chen, S., Jiang, J., Guo, B., 2021. Effect of pore geometry and heterogeneous surface wettability on the nanoconfined phase behavior in nanopore networks of shale rocks. In: *SPE/AAPG/SEG Unconventional Resources Technology Conference (OnePetro)*.
- Chen, S., Qin, C., Guo, B., 2020. Fully implicit dynamic pore-network modeling of two-phase flow and phase change in porous media. *Water Resour. Res.* 56, e2020WR028510.
- Chen, Y., Cheng, P., 2005. Condensation of steam in silicon microchannels. *Int. Commun. Heat Mass Tran.* 32, 175–183.
- Civan, F., Devegowda, D., Sigal, R., 2012. Theoretical fundamentals, critical issues, and adequate formulation of effective shale gas and condensate reservoir simulation. Porous media and its applications in science, engineering, and industry. *AIP Conf. Proc.* 1453, 155–160.
- Collins, D., Nghiem, L., Li, Y., Grabonstotter, J., et al., 1992. An efficient approach to adaptive-implicit compositional simulation with an equation of state. *SPE Reservoir Eng.* 7 (2), 259–264.
- Coskuner, G., 1997. Microvisual study of multiphase gas condensate flow in porous media. *Transport Porous Media* 28, 1–18.
- Cubaud, T., Ulmanella, U., Ho, C.M., 2006. Two-phase flow in microchannels with surface modifications. *Fluid Dynam. Res.* 38, 772.
- Cui, R., Hassanizadeh, S.M., Sun, S., 2022. Pore-network modeling of flow in shale nanopores: network structure, flow principles, and computational algorithms. *Earth Sci. Rev.*, 104203.
- Da Wang, Y., Chung, T., Armstrong, R.T., Mostaghimi, P., 2020. ML-LBM: Machine Learning Aided Flow Simulation in Porous Media arXiv preprint arXiv:2004.11675.
- Danesh, A., Henderson, G.D., Peden, J.M., 1991. Experimental investigation of critical condensate saturation and its dependence on interstitial water saturation in water-wet rocks. *SPE Reservoir Eng.* 336–342.
- Danesh, A., Henderson, G.D., Krinis, D., Peden, J.M., 1988. Experimental Investigation of Retrograde Condensation in Porous Media at.
- Danesh, A., Khazam, M., Henderson, G., Tehrani, D., Peden, J., 1994. Gas condensate recovery studies. In: *DTI Improved Oil Recovery and Research Dissemination Seminar (London)*.
- Danesh, A., Krinis, A., Henderson, G.D., Peden, J.M., 1989. Visual investigation of retrograde phenomena and gas condensate flow in porous media. In: *European Symp. Enhanced Oil Recovery*.
- Danesh, A., Krinis, D., Henderson, G.D., Peden, J.M., 1987. Visual investigation of retrograde phenomena and gas condensate flow in porous media. In: *the 4th European Symposium on Enhanced Oil Recovery*.
- Daneshian, B., Habibagahi, G., Nikooee, E., 2021. Determination of unsaturated hydraulic conductivity of sandy soils: a new pore network approach. *Acta Geotechnica* 16 (2), 449–466.
- Dawe, R.A., Grattoni, C.A., 2007. Fluid flow behaviour of gas-condensate and near-miscible fluids at the pore scale. *J. Petrol. Sci. Eng.* 55 (3–4), 228–236.

- Dehshibi, R.R., Sadatshojaie, A., Mohebbi, A., Riazi, M., 2019. A new insight into pore body filling mechanism during waterflooding in a glass micro-model. *Chem. Eng. Res. Des.* 151, 100–107.
- Dong, H., Blunt, M.J., 2009. Pore-network extraction from micro-computerized-tomography images. *Phys. Rev.* 80, 036307. E.
- Dong, M., Dullien, F.A., Dai, L., Li, D., 2005. Immiscible displacement in the interacting capillary bundle model part I. Development of interacting capillary bundle model. *Transport Porous Media* 59 (1), 1–18.
- Fang, C., Steinbrenner, J.E., Wang, F.M., Goodson, K.E., 2010. Impact of wall hydrophobicity on condensation flow and heat transfer in silicon microchannels. *J. Micromech. Microeng.* 20, 045018.
- Fang, F., Firoozabadi, A., Abbaszadeh, M., Radke, C., et al., 1996. A phenomenological modeling of critical condensate saturation. In: *SPE Annual Technical Conference and Exhibition*. Society of Petroleum Engineers.
- Fathi, H., Raouf, A., Mansouri, S.H., 2017. Insights into the role of wettability in cathode catalyst layer of proton exchange membrane fuel cell; pore scale immiscible flow and transport processes. *J. Power Sources* 349, 57–67.
- Fatt, I., 1956a. The network model of porous media I. Capillary pressure characteristics. *Trans AIME* 207, 144–159.
- Fatt, I., 1956b. The network model of porous media II. Dynamic properties of a single size tube network. *Trans AIME* 207, 160–163.
- Fatt, I., 1956c. The network model of porous media III. Dynamic properties of networks with tube radius distribution. *Trans AIME* 207, 164–181.
- Foroughi, S., Bijeljic, B., Lin, Q., Raeini, A.Q., Blunt, M.J., 2020. Pore-by-pore modeling, analysis, and prediction of two-phase flow in mixed-wet rocks. *Phys. Rev.* 102 (2), 023302.
- Frank, F., Liu, C., Alpak, F.O., Berg, S., Riviere, B., 2018. Direct numerical simulation of flow on pore-scale images using the phase-field method. *SPE J.* 23 (5), 1833–1850.
- Ganiea, K., Idrisb, A.K., Mohshima, D.F., Wan Sulaimanb, W.R., Mohd Saaida, I., Abdul Maika, A., 2019. A review on the wettability alteration mechanism in condensate banking removal. *J. Petrol. Sci. Eng.* 183, 106431.
- Gholampour, F., Mahdiyari, H., 2019. A new correlation for relative permeability in gas-condensate reservoirs. *J. Petrol. Sci. Eng.* 172, 831–838.
- Golparvar, A., Zhou, Y., Wu, K., Ma, J., Yu, Z., 2018. A comprehensive review of pore-scale modeling methodologies for multiphase flow in porous media. *Advances in Geo-Energy Research* 2 (4), 418–440.
- Gostick, J.T., 2017. Versatile and efficient pore network extraction method using marker-based watershed segmentation. *Phys. Rev.* 96, 023307. E.
- Guo, B., Mehmani, Y., Tchelepi, H.A., 2019. Multiscale formulation of pore-scale compressible Darcy-Stokes flow. *J. Comput. Phys.* 397, 108849.
- Heiba, A.A., Davis, H.T., Scriven, L.E., 1983. Effect of wettability on two-phase relative permeabilities and capillary pressures. In: *SPE Annual Technical Conference and Exhibition*. OnePetro.
- Henderson, G.D., Danesh, A., Tehrani, D.H., Peden, J.M., 1997. The effect of velocity and interfacial tension on the relative permeability of gas condensate fluids in the wellbore region. *J. Petrol. Sci. Eng.* 17, 265–273.
- Henderson, G.D., Danesh, A., Tehrani, D.H., Al-Kharusi, B., 2000. The relative significance of positive coupling and inertial effects on gas condensate relative permeabilities at high velocity. In: *SPE Annual Technical Conference and Exhibition*. OnePetro.
- Henderson, G.D., Danesh, A., Tehrani, D.H., Peden, J.M., 1995. The effect of velocity and interfacial tension on the relative permeability of gas condensate fluids in the wellbore region. In: *IOR 8th European Symposium on Improved Oil Recovery*.
- Hilpert, M., Miller, C.T., 2001. Pore-morphology-based simulation of drainage in totally wetting porous media. *Adv. Water Resour.* 24 (3–4), 243–255.
- Hosseinkhani, E., Habibagahi, G., Nikooee, E., 2023. Cyclic modeling of unsaturated sands using a pore-scale hydromechanical approach. *Int. J. Numer. Anal. Methods Geomech.* 47 (3), 457–481.
- Huang, X., Bandilla, K.W., Celia, M.A., 2016. Multi-physics pore-network modeling of two-phase shale matrix flows. *Transport Porous Media* 111 (1), 123–141.
- Hughes, R.G., Blunt, M.J., 2000. Pore scale modeling of rate effects in imbibition. *Transport Porous Media* 40 (3), 295–322.
- Hui, M.H., Blunt, M.J., 2000. Effects of wettability on three-phase flow in porous media. *J. Phys. Chem. B* 104 (16), 3833–3845.
- Hunt, A., Ewing, R., Ghanbarian, B., 2014. *Percolation Theory for Flow in Porous Media*, vol. 880. Springer.
- Hunt, A.G., Ewing, R.P., Horton, R., 2013. What's wrong with soil physics? *Soil Sci. Soc. Am. J.* 77 (6), 1877–1887.
- Idowu, N.A., 2009. Pore-scale Modelling: Stochastic Network Generation and Modelling of Rate Effects in Waterflooding. PhD Thesis. Imperial College London.
- Jamiolahmady, M., Danesh, A., Tehrani, D.H., Duncan, D.B., 2000. A mechanistic model of gas-condensate flow in pores. *Transport Porous Media* 41 (1), 17–46.
- Jamiolahmady, M., Danesh, A., Tehrani, D.H., Duncan, D.B., 2003. Positive effect of flow velocity on gas-condensate relative permeability: network modelling and comparison with experimental results. *Transport Porous Media* 52, 159–183.
- Jamiolahmady, M., Sohrabi, M., Ireland, S., 2009. Gas condensate relative permeability of low permeability rocks: coupling versus inertia. In: *SPE Middle East Oil and Gas Show and Conference*. OnePetro.
- Jettestuen, E., Friis, H.A., Helland, J.O., 2021. A locally conservative multiphase level set method for capillary-controlled displacements in porous media. *J. Comput. Phys.* 428, 109965.
- Joekar-Niasar, V., Hassanizadeh, S.M., 2011. Effect of fluids properties on non-equilibrium capillarity effects: dynamic pore-network modeling. *Int. J. Multiphas. Flow* 37 (2), 198–214.
- Joekar-Niasar, V., Hassanizadeh, S.M., 2012. Analysis of fundamentals of two-phase flow in porous media using dynamic pore-network models: a review. *Crit. Rev. Environ. Sci. Technol.* 42 (18), 1895–1976.
- Joekar-Niasar, V., Hassanizadeh, S.M., Dahle, H.K., 2010a. Non-equilibrium effects in capillarity and interfacial area in two-phase flow: dynamic pore-network modelling. *J. Fluid Mech.* 655, 38–71.
- Joekar-Niasar, V., Prodanović, M., Wildenschild, D., Hassanizadeh, S.M., 2010b. Network model investigation of interfacial area, capillary pressure and saturation relationships in granular porous media. *Water Resour. Res.* 46 (6).
- Khaksar, H., Habibagahi, G., Nikooee, E., 2013. SWRC modeling in unsaturated soils: a pore network approach. In: *Poromechanics V: Proceedings of the Fifth Biot Conference on Poromechanics*, pp. 1570–1579.
- Khoshghalb, A., Pasha, A.Y., Khalili, N., 2015. A fractal model for volume change dependency of the water retention curve. *Geotechnique* 65 (2), 141–146.
- King, P.R., 1987. The fractal nature of viscous fingering in porous media. *J. Phys. A: Math. Gen.* 20 (8), L529.
- Koplik, J., Lasseter, T.J., 1985. Two-phase flow in random network models of porous media. *Soc. Petrol. Eng. J.* 25 (1), 89–100.
- Kunz, P., Zarihos, I.M., Karadimitriou, N.K., Huber, M., Nieken, U., Hassanizadeh, S.M., 2016. Study of multi-phase flow in porous media: comparison of SPH simulations with micro-model experiments. *Transport Porous Media* 114 (2), 581–600.
- Labeled, I., Oyeneyin, B., Oluayemi, G., 2018. Gas-condensate flow modelling for shale reservoirs. *J. Nat. Gas Sci. Eng.* 59, 156–167.
- Lenormand, R., Zarcone, C., Sarr, A., 1983. Mechanisms of the displacement of one fluid by another in a network of capillary ducts. *J. Fluid Mech.* 135, 337–353.
- Li, J., McDougall, S.R., Sorbie, K.S., 2017. Dynamic pore-scale network model (PNM) of water imbibition in porous media. *Adv. Water Resour.* 107, 191–211.
- Li, K., Firoozabadi, A., et al., 2000. Phenomenological modeling of critical condensate saturation and relative permeabilities in gas/condensate systems. *SPE J.* 5 (2), 138–147.
- Likos, W.J., Jaafar, R., 2013. Pore-scale model for water retention and fluid partitioning of partially saturated granular soil. *J. Geotech. Geoenviron. Eng.* 139 (5), 724–737.
- Lin, Q., Bijeljic, B., Berg, S., Pini, R., Blunt, M.J., Krevor, S., 2019. Minimal surfaces in porous media: pore-scale imaging of multiphase flow in an altered-wettability Bentheimer sandstone. *Phys. Rev.* 99 (6), 063105.
- Liu, H., Valocchi, A.J., Kang, Q., 2012. Three-dimensional lattice Boltzmann model for immiscible two-phase flow simulations. *Phys. Rev.* 85 (4), 046309.
- Liu, J., Regenauer-Lieb, K., 2021. Application of percolation theory to microtomography of rocks. *Earth Sci. Rev.* 214, 103519.
- Liu, M., Meakin, P., Huang, H., 2007. Dissipative particle dynamics simulation of pore-scale multiphase fluid flow. *Water Resour. Res.* 43 (4).
- Liu, M.B., Liu, G.R., Zhou, L.W., Chang, J., 2015. Dissipative particle dynamics (DPD): an overview and recent developments. *Arch. Comput. Methods Eng.* 22 (4), 529–556.
- Lourenço, S.D.N., Gallipoli, D., Augarde, C.E., Toll, D.G., Fisher, P.C., Congreve, A., 2012. Formation and evolution of water menisci in unsaturated granular media. *Geotechnique* 62 (3), 193–199.
- Mahmoodlu, M.G., Raouf, A., Bultreys, T., Van Stappen, J., Cnudde, V., 2020. Large-scale pore network and continuum simulations of solute longitudinal dispersivity of a saturated sand column. *Adv. Water Resour.* 144, 103713.
- Mani, V., Mohanty, K.K., 1998. Pore-level network modeling of three-phase capillary pressure and relative permeability curves. *SPE J.* 3 (3), 238–248.
- Mason, G., Mellor, D.W., 1995. Simulation of drainage and imbibition in a random packing of equal spheres. *J. Colloid Interface Sci.* 176 (1), 214–225.
- McDougall, J., Li, S.R., Sorbie, K.S., 2017. Dynamic pore-scale network model (PNM) of water imbibition in porous media. *Adv. Water Resour.* 107, 191–211.
- Meakin, P., Tartakovsky, A.M., 2009. Modeling and simulation of pore-scale multiphase fluid flow and reactive transport in fractured and porous media. *Rev. Geophys.* 47 (3).
- Mehmani, A., Verma, R., Prodanović, M., 2020. Pore-scale modeling of carbonates. *Mar. Petrol. Geol.* 114, 104141.
- Mehmani, Y., Tchelepi, H.A., 2018. Multiscale computation of pore-scale fluid dynamics: single-phase flow. *J. Comput. Phys.* 375, 1469–1487.
- Mehmani, Y., Tchelepi, H.A., 2019. Multiscale formulation of two-phase flow at the pore scale. *J. Comput. Phys.* 389, 164–188.
- Milatz, M., Andò, E., Viggiani, G.C., Mora, S., 2022. In situ X-ray CT imaging of transient water retention experiments with cyclic drainage and imbibition. *Open Geomechanics* 3, 1–33.
- Moebius, F., Or, D., 2014. Inertial forces affect fluid front displacement dynamics in a pore-throat network model. *Phys. Rev.* 90, 023019. E.
- Mogensen, K., Stenby, E.H., 1996. Simulation of two-phase immiscible displacement using a dynamic network model that accounts for crevice flow and ganglion dynamics. In: *The 17th Annual Workshop and Symposium of the International Energy Agency Collaborative Project on Enhanced Oil Recovery*.
- Mogensen, K., Stenby, E.H., 1997. A dynamic pore-scale model of imbibition. In: *He 18th Annual Workshop and Symposium of the International Energy Agency Collaborative Project on Enhanced Oil Recovery*.
- Mogensen, K., Stenby, E.H., 1998. A dynamic two-phase pore-scale model of imbibition. *Transport Porous Media* 32 (3), 299–327.
- Mogensen, K., Stenby, E., Banerjee, S., Barker, V.A., 1999. Comparison of iterative methods for computing the pressure field in a dynamic network model. *Transport Porous Media* 37, 277–301.
- Mohammadi, S., Sorbie, K., Danesh, A., Peden, J., et al., 1990. Pore-level modelling of gas-condensate flow through horizontal porous media. In: *SPE Annual Technical Conference and Exhibition*. Society of Petroleum Engineers.

- Momeni, A., Dadvar, M., Hekmatzadeh, M., Dabir, B., 2017. 3d pore network modeling and simulation for dynamic displacement of gas and condensate in wellbore region. *Int. J. Multiphase Flow* 97, 147–156.
- Montellà, E.P., Yuan, C., Chareyre, B., Gens, A., 2020. Hybrid multi-scale model for partially saturated media based on a pore network approach and lattice Boltzmann method. *Adv. Water Resour.* 144, 103709.
- Mott, R., Cable, A., Spearing, M., 2000. Measurements and Simulation of Inertial and High Capillary Number Flow Phenomena in Gas-Condensate Relative Permeability. AEA Technology. SPE 62932.
- Nekoeian, S., Goharrizi, A.S., Jamialahmadi, M., Jafari, S., Sotoudeh, F., 2018. A novel Shan and Chen type Lattice Boltzmann two phase method to study the capillary pressure curves of an oil water pair in a porous media. *Petroleum* 4 (3), 347–357.
- Nguyen, N.H., Nguyen, V.P., Wu, J.Y., Le, T.H.H., Ding, Y., 2019. Mesh-based and meshfree reduced order phase-field models for brittle fracture: one dimensional problems. *Materials* 12 (11), 1858.
- Nguyen, V.H., Sheppard, A.P., Knackstedt, M.A., Pinczewski, W.V., 2006. The effect of displacement rate on imbibition relative permeability and residual saturation. *J. Petrol. Sci. Eng.* 52, 54–70.
- Nikooee, E., Habibagahi, G., Daneshian, B., Sweijen, T., Hassanizadeh, S.M., 2017. A grain scale model to predict retention properties of unsaturated soils. In: *Proceedings of the 19th International Conference on Soil Mechanics and Geotechnical Engineering*.
- Nikooee, E., Habibagahi, G., Khaksar, H., Hassanizadeh, S., Raouf, A., 2014. Pore network modeling of unsaturated soils: fundamentals, recent advancements and future perspectives. *Numerical Methods in Geotechnical Engineering-NUMGE 2014*, 1007–1012.
- Nikooee, E., Sweijen, T., Hassanizadeh, S.M., 2016. Determination of the relationship among capillary pressure, saturation and interfacial area: a pore unit assembly approach. In: *E3S Web of Conferences*, vol. 9. EDP Sciences, 02002.
- Øren, P.E., Bakke, S., Arntzen, O.J., 1998. Extending predictive capabilities to network models. *SPE J.* 3 (4), 324–336.
- Øren, P.E., Bakke, S., 2002. Process based reconstruction of sandstones and prediction of transport properties. *Transport Porous Media* 46 (2), 311–343.
- Osorno, M., Schirwon, M., Kijanski, N., Sivanapillai, R., Steeb, H., Göttsche, D., 2021. A cross-platform, high-performance SPH toolkit for image-based flow simulations on the pore scale of porous media. *Comput. Phys. Commun.* 267, 108059.
- Ovaysi, S., Piri, M., 2010. Direct pore-level modeling of incompressible fluid flow in porous media. *J. Comput. Phys.* 229 (19), 7456–7476.
- Pan, C., Prins, J.F., Miller, C.T., 2004. A high-performance lattice Boltzmann implementation to model flow in porous media. *Comput. Phys. Commun.* 158 (2), 89–105.
- Pan, S., Ma, J., Zuo, J.Y., Hamed, N., 2019. A pore-scale mechanistic investigation of shale gas condensate at near saturation pressure on fluid flow in shale. In: *SPE/AAPG/SEG Unconventional Resources Technology Conference (OnePetro)*.
- Panja, P., Velasco, R., Deo, M., 2020. Understanding and modeling of gas-condensate flow in porous media. *Advances in Geo-Energy Research* 4 (2), 173–186.
- Penghui, S., Zhaohui, X., Ping, W., Liangchao, Q., Wenguang, Z., 2019. Investigation of pore structure and fractal characteristics in an organic-rich shale gas-condensate reservoir from the duvernay formation. In: *SPE Europe Featured at 81st EAGE Conference and Exhibition. OnePetro*.
- Piri, M., 2003. Pore-Scale Modelling of Three-phase Flow. Ph.D. thesis. Imperial College, London.
- Piri, M., Blunt, M.J., 2005. Three-dimensional mixed-wet random pore-scale network modeling of two- and three-phase flow in porous media. I. Model description. *Phys. Rev. E* 71, 026301.
- Prat, M., 2011. Pore network models of drying, contact angle, and film flows. *Chem. Eng. Technol.* 34 (7), 1029–1038.
- Primkulov, B.K., Talman, S., Khaleghi, K., Shokri, A.R., Chalaturnyk, R., Zhao, B., MacMinn, C.W., Juanes, R., 2018. Quasistatic fluid-fluid displacement in porous media: invasion-percolation through a wetting transition. *Physical Review Fluids* 3 (10), 104001.
- Puig Montellà, E., 2019. Modeling capillarity and two-phase flow in granular media: from porescale to network scale, PhD thesis. UPC-Grenoble intritute of tech.
- Qin, C., 2015. Water transport in the gas diffusion layer of a polymer electrolyte fuel cell: dynamic pore-network modeling. *J. Electrochem. Soc.* 162 (9), F1036.
- Qin, C.Z., van Brummelen, H., 2019. A dynamic pore-network model for spontaneous imbibition in porous media. *Adv. Water Resour.* 133, 103420.
- Qin, C.Z., Wang, X., Zhang, H., Hefny, M., Jiang, H., Tian, J., Deng, W., 2022. Numerical studies of spontaneous imbibition in porous media: Model development and pore-scale perspectives. *J. Petrol. Sci. Eng.* 218, 110961.
- Rabbani, A., Jamshidi, S., Salehi, S., 2014. An automated simple algorithm for realistic pore network extraction from micro-tomography Images. *J. Petrol. Sci. Eng.* 123, 164–171.
- Raeini, A.Q., Bijeljic, B., Blunt, M.J., 2015. Modelling capillary trapping using finite-volume simulation of two-phase flow directly on micro-CT images. *Adv. Water Resour.* 83, 102–110.
- Raeini, A.Q., Giudici, L.M., Blunt, M.J., Bijeljic, B., 2022. Generalized network modelling of two-phase flow in a water-wet and mixed-wet reservoir sandstone: uncertainty and validation with experimental data. *Adv. Water Resour.* 164, 104194.
- Raouf, A., Hassanizadeh, S.M., 2010. A new method for generating pore-network models of porous media. *Transport Porous Media* 81 (3), 391–407.
- Raouf, A., Hassanizadeh, S.M., 2012. A new formulation for pore-network modeling of two-phase flow. *Water Resour. Res.* 48 (1).
- Raouf, A., Nick, H.M., Hassanizadeh, S.M., Spiers, C.J., 2013. PoreFlow: a complex pore-network model for simulation of reactive transport in variably saturated porous media. *Comput. Geosci.* 61, 160–174.
- Reis, P.K., Carvalho, M.S., 2020. Pore-scale analysis of condensate blockage mitigation by wettability alteration. *Energies* 13 (18), 4673.
- Reis, P.K., Carvalho, M.S., 2021. Pore-scale compositional modeling of gas-condensate flow: effects of interfacial tension and flow velocity on relative permeability. *J. Petrol. Sci. Eng.* 202, 108454.
- Reis, P.K., Carvalho, M.S., 2022. Pore-scale analysis of gas injection in gas-condensate reservoirs. *J. Petrol. Sci. Eng.* 212, 110189.
- Rostami, A., Habibagahi, G., Ajdari, M., Nikooee, E., 2015. Pore network investigation on hysteresis phenomena and influence of stress state on the SWRC. *Int. J. GeoMech.* 15 (5), 04014072.
- Ruspini, L.C., Farokhpoor, R., Øren, P.E., 2017. Pore-scale modeling of capillary trapping in water-wet porous media: a new cooperative pore-body filling model. *Adv. Water Resour.* 108, 1–14.
- Ruspini, L.C., Øren, P.E., Berg, S., Masalmeh, S., Bultreys, T., Taberner, C., et al., 2021. Multiscale digital rock analysis for complex rocks. *Transport Porous Media* 139 (2), 301–325.
- Sahimi, M., Tahmasebi, P., 2022. The Potential of Quantum Computing for Geoscience. *Transport in Porous Media*, pp. 1–21.
- Sakhaei, Z., Nikooee, E., Riazi, M., 2020. A new formulation for non-equilibrium capillarity effect using multi-gene genetic programming (MGGP): accounting for fluid and porous media properties. *Eng. Comput.* 1–13.
- Santos, J.E., Xu, D., Jo, H., Landry, C.J., Prodanović, M., Pycrc, M.J., 2020. PoreFlow-Net: a 3D convolutional neural network to predict fluid flow through porous media. *Adv. Water Resour.* 138, 103539.
- Santos, M., Carvalho, M., 2020. Pore network model for retrograde gas flow in porous media. *J. Petrol. Sci. Eng.* 185, 106635.
- Scardovelli, R., Zaleski, S., 1999. Direct numerical simulation of free-surface and interfacial flow. *Annu. Rev. Fluid Mech.* 31 (1), 567–603.
- Schmatz, J., Urai, J.L., Berg, S., Ott, H., 2015. Nanoscale imaging of pore-scale fluid-fluid-solid contacts in sandstone. *Geophys. Res. Lett.* 42 (7), 2189–2195.
- Sethian, J.A., 1999. Level Set Methods and Fast Marching Methods: Evolving Interfaces in Computational Geometry. In: *Fluid Mechanics, Computer Vision, and Materials Science*, vol. 3. Cambridge university press.
- Shams, M., Singh, K., Bijeljic, B., Blunt, M.J., 2021. Direct numerical simulation of pore-scale trapping events during capillary-dominated two-phase flow in porous media. *Transport Porous Media* 138 (2), 443–458.
- Singh, D., Friis, H.A., Jettestuen, E., Helland, J.O., 2022. A level set approach to Ostwald ripening of trapped gas bubbles in porous media. *Transport Porous Media* 145 (2), 441–474.
- Singh, K., Bultreys, T., Raeini, A.Q., Shams, M., Blunt, M.J., 2022. New type of pore-snap-off and displacement correlations in imbibition. *J. Colloid Interface Sci.* 609, 384–392.
- Singh, K., Menke, H., Andrew, M., Lin, Q., Rau, C., Blunt, M.J., Bijeljic, B., 2017. Dynamics of snap-off and pore-filling events during two-phase fluid flow in permeable media. *Sci. Rep.* 7 (1), 1–13.
- Singh, M., Mohanty, K.K., 2003. Review: dynamic modelling of drainage through three-dimensional porous materials. *Chem. Eng. Sci.* 58, 1–18.
- Sivanapillai, R., Steeb, H., 2018. Fluid Interfaces during Viscous-Dominated Primary Drainage in 2D Micromodels Using Pore-Scale SPH Simulations. *Geofluids*, 2018.
- Song, W., Liu, L., Wang, D., Li, Y., Prodanović, M., Yao, J., 2020. Nanoscale confined multicomponent hydrocarbon thermodynamic phase behavior and multiphase transport ability in nanoporous material. *Chem. Eng. J.* 382, 122974.
- Sorbie, K.S., Skaue, A., 2012. Can network modeling predict two-phase flow physics? *Petrophysics* 53 (6), PAGE 401–409.
- Spurin, C., Bultreys, T., Rücker, M., Garfi, G., Schlepütz, C.M., Novak, V., Krevor, S., 2020. Real-time imaging reveals distinct pore-scale dynamics during transient and equilibrium subsurface multiphase flow. *Water Resour. Res.* 56 (12), e2020WR028287.
- Stinchcombe, R.B., 1974. Conductivity and spin-wave stiffness in disordered systems-an exactly soluble model. *J. Phys. C Solid State Phys.* 7 (1), 179.
- Stinchcombe, R.B., Watson, B.P., 1976. Renormalization group approach for percolation conductivity. *J. Phys. C Solid State Phys.* 9 (17), 3221.
- Sweijen, T., Aslannejad, H., Hassanizadeh, S.M., 2017. Capillary pressure-saturation relationships for porous granular materials: pore morphology method vs. pore unit assembly method. *Adv. Water Resour.* 107, 22–31.
- Sweijen, T., Nikooee, E., Hassanizadeh, S.M., Chareyre, B., 2016. The effects of swelling and porosity change on capillarity: DEM coupled with a pore-unit assembly method. *Transport Porous Media* 113 (1), 207–226.
- Tang, K., Da Wang, Y., McClure, J., Chen, C., Mostaghimi, P., Armstrong, R.T., 2022. Generalizable framework of unpaired domain transfer and deep learning for the processing of real-time synchrotron-based X-ray microcomputed tomography images of complex structures. *Physical Review Applied* 17 (3), 034048.
- Tartakovsky, A.M., Meakin, P., 2006. Pore scale modeling of immiscible and miscible fluid flows using smoothed particle hydrodynamics. *Adv. Water Resour.* 29 (10), 1464–1478.
- Tartakovsky, A.M., Meakin, P., Scheibe, T.D., Wood, B.D., 2007. A smoothed particle hydrodynamics model for reactive transport and mineral precipitation in porous and fractured porous media. *Water Resour. Res.* 43 (5).
- Tembely, M., AlSumaiti, A.M., Alameri, W., 2020. A deep learning perspective on predicting permeability in porous media from network modeling to direct simulation. *Comput. Geosci.* 24 (4), 1541–1556.
- Thompson, K.E., 2002. Pore-scale modeling of fluid transport in disordered fibrous materials. *AIChE J.* 48 (7), 1369–1389.
- Tranter, T.G., Boillat, P., Mularczyk, A., Manzi-Orezoli, V., Shearing, P.R., Brett, D.J.L., Eller, J., Gostick, J.T., Forner-Cuenca, A., 2020. Pore network modelling of capillary

- transport and relative diffusivity in gas diffusion layers with patterned wettability. *J. Electrochem. Soc.* 167 (11), 114512.
- Valvatne, P.H., Blunt, M.J., 2004. Predictive pore-scale modeling of two-phase flow in mixed wet media. *Water Resour. Res.* 40 (7).
- Van Genuchten, M.T., 1980. A closed-form equation for predicting the hydraulic conductivity of unsaturated soils. *Soil Sci. Soc. Am. J.* 44 (5), 892–898.
- Vogel, H.J., Tölke, J., Schulz, V.P., Krafczyk, M., Roth, K., 2005. Comparison of a lattice-Boltzmann model, a full-morphology model, and a pore network model for determining capillary pressure–saturation relationships. *Vadose Zone J.* 4 (2), 380–388.
- Wang, S., Ruspini, L.C., Øren, P.E., Van Offenwert, S., Bultreys, T., 2022. Anchoring multi-scale models to micron-scale imaging of multiphase flow in rocks. *Water Resour. Res.* 58 (1), e2021WR030870.
- Wang, X., Mohanty, K., 1999. Critical condensate saturation in porous media. *J. Colloid Interface Sci.* 214 (2), 416–426.
- Wang, X., Mohanty, K.K., et al., 2000. Pore-network model of flow in gas/condensate reservoirs. *SPE J.* 5 (4), 426–434.
- Wang, Y., Blunt, M.J., Armstrong, R.T., Mostaghimi, P., 2021. Deep learning in pore scale imaging and modeling. *Earth Sci. Rev.* 215, 103555.
- Weishaupt, K., Helmig, R., 2021. A dynamic and fully implicit non-isothermal, two-phase, two-component pore-network model coupled to single-phase free flow for the pore-scale description of evaporation processes. *Water Resour. Res.* 57 (4) e2020WR028772.
- Wopara, O.F., Iyuke, S.E., 2018. Review of studies on pore-network modeling of wettability effects on water flood oil recovery. *J. Petrol. Gas Eng.* 2141–2677.
- Wu, T., Djilali, N., 2012. Experimental investigation of water droplet emergence in a model polymer electrolyte membrane fuel cell microchannel. *J. Power Sources* 208, 248–256.
- Xiong, Q., Baychev, T.G., Jivkov, A.P., 2016. Review of pore network modelling of porous media: experimental characterisations, network constructions and applications to reactive transport. *J. Contam. Hydrol.* 192, 101–117.
- Yi, Z., Lin, M., Jiang, W., Zhang, Z., Li, H., Gao, J., 2017. Pore network extraction from pore space images of various porous media systems. *Water Resour. Res.* 53, 3424–3445.
- Yin, X., Aslannejad, H., de Vries, E.T., Raouf, A., Hassanizadeh, S.M., 2018. Droplet imbibition into paper coating layer: pore-network modeling simulation. *Transport Porous Media* 125 (2), 239–258.
- Younes, N., Benseghier, Z., Millet, O., Wautier, A., Nicot, F., Wan, R., 2022. Phase-field Lattice Boltzmann model for liquid bridges and coalescence in wet granular media. *Powder Technol.* 411, 117942.
- Zarikos, I.M., Hassanizadeh, S.M., Van Oosterhout, L.M., van Oordt, W., 2018a. Manufacturing a micro-model with integrated fibre optic pressure sensors. *Transport Porous Media* 122 (1), 221–234.
- Zarikos, I., Terzis, A., Hassanizadeh, S.M., Weigand, B., 2018b. Velocity distributions in trapped and mobilized non-wetting phase ganglia in porous media. *Sci. Rep.* 8 (1), 1–11.
- Zhao, B., MacMinn, C.W., Primkulov, B.K., Chen, Y., Valocchi, A.J., Zhao, J., Kang, Q., Bruning, K., McClure, J.E., Miller, C.T., Fakhari, A., 2019. Comprehensive comparison of pore-scale models for multiphase flow in porous media. *Proc. Natl. Acad. Sci. USA* 116 (28), 13799–13806.
- Zhao, J., Qin, F., Derome, D., Carmeliet, J., 2020. Simulation of quasi-static drainage displacement in porous media on pore-scale: coupling lattice Boltzmann method and pore network model. *J. Hydrol.* 588, 125080.
- Zhou, X.H., McClure, J.E., Chen, C., Xiao, H., 2022. Neural network-based pore flow field prediction in porous media using super resolution. *Physical Review Fluids* 7 (7), 074302.
- Zhu, G., Chen, H., Yao, J., Sun, S., 2019. Efficient energy-stable schemes for the hydrodynamics coupled phase-field model. *Appl. Math. Model.* 70, 82–108.